Numerical Modeling and Experimental Studies on the Hydrodynamics and Heat

Transfer of Silica Glass Particles

by

Manogna Adepu

A Dissertation Presented in Partial Fulfillment
of the Requirements for the Degree
Doctor of Philosophy

Approved March 2020 by the
Graduate Supervisory Committee:

Heather Emady, Chair
Christopher Muhich
MaryLaura Thomas
Matthew Green
Yang Jiao

ARIZONA STATE UNIVERSITY

May 2020

ABSTRACT

Granular material can be found in many industries and undergo process steps like drying, transportation, coating, chemical and physical conversions. Understanding and optimizing such processes can save energy as well as material costs, leading to improved products. Silica beads are one such granular material encountered in many industries as a catalyst support material. The present research aims to obtain a fundamental understanding of the hydrodynamics and heat transfer mechanisms in silica beads. Studies are carried out using a hopper discharge bin and a rotary drum, which are some of the most common process equipment found in various industries. Two types of micro-glass beads with distinct size distributions are used to fill the hopper in two possible packing arrangements with varying mass ratios. For the well-mixed configuration, the fine particles clustered at the hopper bottom towards the end of the discharge. For the layered configuration, the coarse particles packed at the hopper bottom discharge first, opening a channel for the fine particles on the top. Also, parameters such as wall roughness (WR) and particle roughness (PR) are studied by etching the particles. The discharge rate is found to increase with WR, and found to be proportional to (Root mean square of PR)^(-0.58). Furthermore, the drum is used to study the conduction and convection heat transfer behavior of the particle bed with varying process conditions. A new non-invasive temperature measurement technique is developed using infrared thermography, which replaced the traditional thermocouples, to record the temperatures of the particles and the drum wall. This setup is used to understand the flow regimes of the particle bed inside the drum and the heat transfer mechanisms with varying process

conditions. The conduction heat transfer rate is found to increase with decreasing particle size, decreasing fill level, and increasing rotation speed. The convection heat transfer rate increased with increasing fill level and decreasing particle size, and rotation speed had no significant effect. Due to the complexities in these systems, it is not always possible to conduct experiments, therefore, heat transfer models in Discrete Element Method codes (MFIX-DEM: open-source code, and EDEM: commercial code) are adopted, validated, and the effects of model parameters are studied using these codes.

DEDICATION

Papa, Mummy, and Sunny, thank you so much for your love and support through all

these years.

Thank you for understanding,

when I couldn't come home for a long time,

for all the family time I missed,

for all the festivals I missed,

for all the holidays I didn't come home,

for all the unanswered phone calls, and

for everything until date and forever.

I dedicate my work to you three as a token of appreciation for all that you have done for

me. Love you three!

Bharath, I know you keep saying that you have done nothing for this achievement

of mine. But this is the only achievement that I am sincerely and truly proud about from

my past. This is my past and you are my future. I am dedicating this past of mine to you

my future.

ACKNOWLEDGEMENTS

TABLE OF CONTENTS

LIST OF TABLES

LIST OF FIGURES

1   INTRODUCTION

1.1   Background

Past surveys have shown that the processing of powdered material had an annual value of more than $10 billion (McGlinchey, 2009). Studies also demonstrated that an estimated 25–30 % of the total output from the chemical industries was in the physical form of either powdered or agglomerated material (McGlinchey, 2009). The characterization of the particulate material produced, together with the handling and behavior of the powdered material in bulk quantities, is therefore of paramount importance in the optimization of many multiphase and multi-particulate processes. Powders are made into granules in most instances for dust-free and optimized handling and transportation.

1.1.1   Hoppers

This work focuses on the process of hopper discharge using experiments. Across particle technology, hoppers are widely used in many process engineering applications for the storage of granular materials (McGlinchey, 2009). The range of hopper applications is from small-scale pharmaceutical and food processing operations to large-scale minerals industry storage. More important than being used as storage facilities, hoppers are also often used as links between various unit operations in plant processes to provide buffering to control flow variation and operational instability. This becomes more important in a particulate solids processing plant. In this process, the bulk solids

behavior is generally more unpredictable than for gases and liquids, and unsteady flows often occur in the course of handling and processing, and this inconsistency can lead to dramatic loss of revenue and/or delay in process start-up (BJ et al., 1994). One of the major industrial problems in using hoppers is obtaining reproducible and consistent particle discharge flow rates. Furthermore, during the particles flowing through the hopper, jamming is a common phenomenon. This issue has been investigated by many researchers over the past few years (Landry and Grest, 2005; To et al., 2001).

The hopper discharge behavior is associated with the complex flow patterns of granular materials inside the hopper and the hopper properties. This behavior gets even more complicated when the granular materials segregate. Granular materials have long been known to segregate due to differences in particle characteristics such as size, shape, or density. Segregation may render the final products that do not meet the necessary standards of product quality, such as content uniformity in pharmaceuticals and mechanical properties in the case of powder metallurgical parts (Ketterhagen et al., 2007). This heterogeneity not only leads to the rejection of product, but also adversely affects efficiencies through wasted material, labor, and production time. Therefore, it is crucial to understand the flow behavior and the segregation pattern of the granular materials through the hoppers.

1.1.2 Rotary Drums

Granular materials undergo diverse processing steps that include transportation, drying, heating and chemical or physical conversion. In several instances, rotary drums

2

(kilns) are the most commonly used process equipment for this purpose. Rotary drums

are widely employed in the chemical, metallurgical, minerals, ceramics, cement,

polymers, food, fertilizer, waste treatment, pharmaceutical, and catalyst industries (Xu et

al., 1984) to handle bulk materials, especially in the processing of coarse or free-flowing

solids. They are used in operations such as mixing, heating, cooling, reacting and drying

of solids, or a combination of these operations. The wide use of drums can be attributed

to major factors such as the ability to handle an extensive range of feed physical

properties and the flexible adjustment of residence time in a continuous operation mode

involving heterogeneous reactions. They are used to operate under high temperature, for

example, burning of cement clinker (2000 °C) (Peray and Waddell, 1986), calcination of

aluminum oxide and coke (1300°C) (Bui et al., 1995; Kawecki et al., 1974), lime burning

(1200 °C) (Georgallis et al., 2002), calcination of petroleum coke (1100 °C) (Martins et

al., 2001), thermal treatment of waste material (900–1200°C) (Rovaglio et al., 1998) and

the gasification of waste tires or wood to obtain activated carbon (1300 °C) (Ortiz et al.,

2005). As these processes are related to high energy demand, optimizing them can save

energy as well as material costs, leading to improved products. Since most of these

processes are energy-intensive, the handling of granular materials is tightly connected to

a high-energy demand. Considering the wide range of high-temperature applications of

rotary drums, it is essential to understand the bed hydrodynamics along with the

mechanisms of heat transfer. Over the last five decades, there has been a continued

interest in understanding the hydrodynamics of the solid bed inside the rotary drums

(Grajales et al., 2012; Jiang et al., 2011; Makse, 1999). Unlike with the hydrodynamics of

3

the solid bed, less work has been done to understand the heat transfer mechanisms in rotary drums.

The heat transfer in a rotary drum is influenced by a wide range of process parameters like specific heat capacity of the particle bed, particle size, particle size distribution, particle shape, particle density, particle thermal conductivity, rotational speeds, fill levels, drum cross-sectional shape, granular cohesion, friction, baffles, size of baffles, and number of baffles. As it is not always possible to conduct experiments using different materials and all process conditions to study the thermal mechanisms due to the complexity of these processes, computational modeling and simulations have been extensively used to understand the heat transfer mechanisms in rotary drums. In the past, the above mentioned parameters have been investigated using both experiments and computational modeling using continuum and DEM models (Boateng et al., 1996; Dhanjal et al., 2004; Gui et al., 2013; Kwapinska et al., 2006; Liu and Specht, 2010; Piton et al., 2015; Schmid, 2011; Shi et al., 2008; Thammavong et al., 2011; Wes et al., 1976). There are numerous models describing rotary drum heat transfer in the literature (Beckman et al., 1998; Bui et al., 1995; Lehmberg et al., 1977; Schliinder, n.d.; Schlünder and Mollekopf, 1984; Tscheng and Watkinson, 1979; Wes et al., 1976), but the quantitative predictions of these models are significantly different. Also, these models have not been sufficiently confirmed by experimental data. Therefore, more reliable and validated simulation models are required for a good understanding of the complex heat transfer mechanisms in the rotary drum, to make potential energy efficiency

improvements, reduce manufacturing and operation costs, as well as widen its applications at different scales.

1.2   Literature Review

1.2.1   Hopper Discharge

The segregation of granular materials discharging from a hopper has been the focus of several studies in recent years. The most common method of classification of particle segregation is by the fundamental mechanism which gives rise to segregation. As many as thirteen mechanisms by which particles segregate have been identified and reviewed by researchers. The thirteen mechanisms are summarized below (de Silva et al. 2000):

- Trajectory: caused by a greater speed reduction for smaller particles due to air drag.
- Air current: fine particles are deposited at silo walls by air currents created by falling particles.
- Rolling: large or rounded particles roll down the surface of a particle heap in formation.
- Sieving: smaller particles flow downward through a sliding or rolling layer of larger particles.
- Impact: a segregation mechanism where more bouncy particles are found further away from the center of a heap in formation.

- Embedding: larger or denser particles penetrate the surface layer of a heap and become locked in position there.

- Angle of repose: components with lower angle of repose flow more easily toward the edges of a heap.

- Push-away: lighter particles are pushed towards the edge of a heap by equally sized heavier particles falling on the apex of the heap.

- Displacement: larger particles rise above smaller particles as a result of vibrations.

- Percolation: smaller particles fall through void spaces between larger particles, sometimes as a result of localized shear.

- Fluidization: fine or lighter particles are kept fluidized at the surface of the particle mixture.

- Agglomeration: very fine particles form larger aggregates with greater mobility.

- Concentration driven displacement: occurs in rotating devices where fine particles concentrate in zones due to higher mobility.

In addition to the mechanisms listed above, electrostatic interactions of particles may also influence segregation. Of the thirteen mechanisms, percolation and sieving are hypothesized to be the primary means by which segregation occurs. According to Samadani et al. (2000), segregation primarily occurs near the 'V'-shaped granular free surface where shearing of particles occurs. The other eleven mechanisms should be negligible since the particles used in the present work are relatively large, free-flowing,

and spherical with uniform characteristics. Also, there is no projectile motion of particles during discharge from the hopper or inside the hopper.
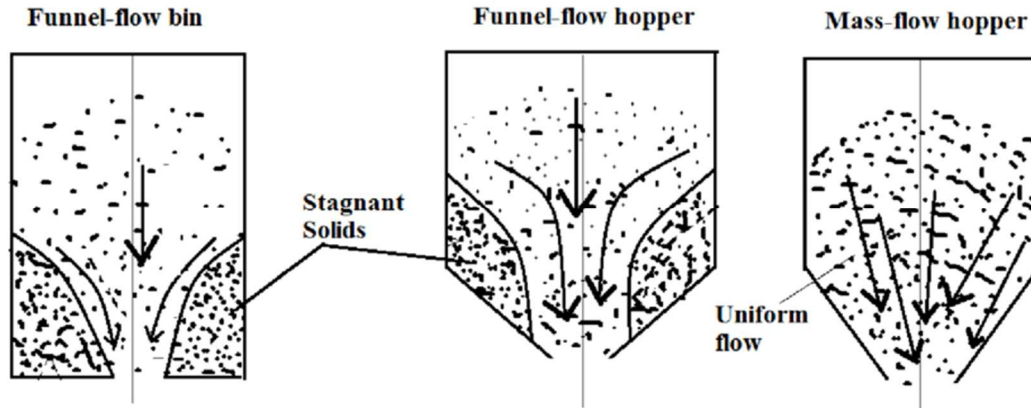
Figure 1. Hopper discharge cross-section showing funnel and mass flow (Van Belle et al., 2018).

Properties of particles contributing to segregation include particle size, shape, density, elasticity, cohesivity, surface roughness, friction, and size ratio. However, some particle properties dominate segregation depending on the process conditions. The concentration of fine particles is another factor that affects segregation. Arteaga and Tüzün examined the effect of fines concentration on the segregation of binary (Arteaga and Tüzün, 1990) and ternary (Tüzün and Arteaga, 1992) materials discharging from mass-flow and funnel-flow hoppers (see Fig. 1). Results showed that most segregation occurred either during an initial transient or a final transient. Typically, more segregation occurs when the fines fraction is lower. This is because there are more void spaces that the number of fine particles that can move through.

Size segregation was shown to be related to the granular microstructure, which is dependent on diameter ratio and fines mass fraction. A model was also developed as shown in Eq. (2.1) to specify a limiting fines mass fraction above which percolation is not feasible due to a transition in the granular microstructure from coarse-continuous to fines-continuous:

$$x_{f,L} = \frac{4}{4 + \Phi_D} \tag{2.1}$$

where $x_{f,L}$ is the limiting fines mass fraction for a given particle diameter ratio, Φ_D. This proposed model is applicable for relatively large, free-flowing, nearly spherical particles, and is independent of hopper geometry. Sleppy and Puri (1996) performed similar experiments using a 50 % mixture of bidisperse sugar granules for varying diameter ratios. Experiments conducted in a mass-flow hopper generally exhibited no segregation. However, discharge from a funnel-flow hopper resulted in a segregation pattern where the first half of discharge was fines-rich, and the second half was fines-depleted. These trends are in qualitative agreement with those of Arteaga and Tüzün (1990). Samadani et al. (1999) examined segregation upon discharge from a quasi-2D, flat-bottomed silo. It was concluded that segregation primarily occurs on the free surface, and therefore the system was analyzed as a flow on an inclined plane following the model of Savage and Lun (1988).

Work by Alexander et al. (2000) examined the asymptotic segregation profile attained through repeated hopper discharges using an apparatus similar to that in the present work. In the Alexander et al. study, a hopper filled with a mixture of glass beads

8

or pharmaceutical excipients was discharged into an identical hopper placed below the first. The second hopper was then swapped with the first, and the process repeated. An asymptotic segregation profile was reached after several iterations, and it was found that this profile is often quite different from the segregation profile of the first discharge and is not dependent on the initial filling method. In another study by Tanaka et al. (1988), the filling and discharge of a hopper with approximately 900 particles was modeled using the discrete element method (DEM). Results showed that a solid, stationary insert in the hopper deterred segregation from occurring during filling, and hence, the discharge tended to be more uniform than if the insert was not present. Ketterhagen et al. (2007) used DEM to model hopper flows with a focus on determining the extent of segregation that occurs during hopper discharge as a function of several particle and hopper parameters. A bi-disperse system consisting of frictional spheres was modeled in a wedge-shaped hopper utilizing two parallel, periodic boundaries (i.e., a quasi-3D hopper) to effectively model a thin slice of a large, rectangular cross-section hopper. The effects of various particle properties such as the diameter and density ratios, mass fraction of each component, and mean particle size, as well as hopper properties such as the fill height, hopper width and wall angle, and outlet width were examined.

The particle diameter ratio, hopper wall angle, particle–wall sliding friction, and the initial fill method were shown to strongly affect the extent of segregation upon discharge. Other parameters which affected segregation, but to a lesser extent, included the mass fraction of each component, hopper dimensions, and particle–particle sliding friction. While this work showed qualitative agreement with previous experimental data

9

(e.g., Arteaga and Tüzün, 1990), the use of periodic boundary conditions rendered it impossible to make direct quantitative comparisons with experimental data in actual hoppers.

1.2.2   Solid Transport in Rotary Drums

There are two components in the transport of the granular solid through the kiln, the transport that occurs in a transverse section, perpendicular to the kiln axis, and the transport taking place along the kiln axis. While the first is important to the homogeneity of the solid bed, the second is critical in determining the bed profile and the mean residence time of the solids in the kiln.
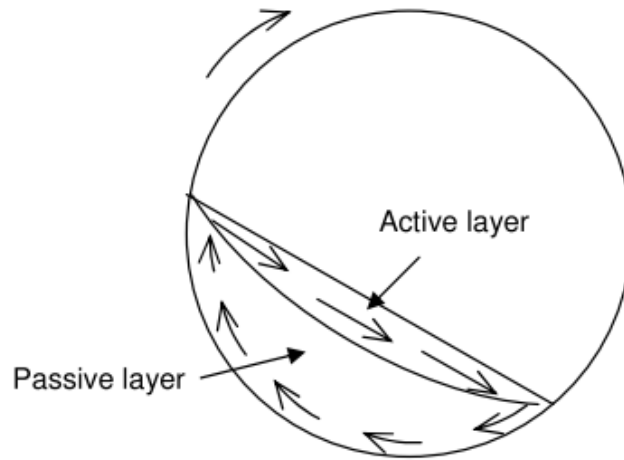
Figure 2. Schematic of the bed cross-section under rolling bed motion in rotary kilns without lifters (J. Mellmann 2001).

The prevailing form of solid transversal motion in rotating kilns without lifters is rolling motion (see Fig. 2). This type of motion is characterized by a uniform, static flow

of a particle layer on the surface (active layer), while the larger part of the bed (passive layer) is transported upwards by solid body rotation with the rotational speed of the wall (Chatterjee et al., 1983; Vàhl and Kingma, 1952).

Four different approaches are commonly used for the quantification of axial solid transport variables, (e.g., axial bed depth profile, total hold-up, mean residence time and axial velocity) with or without considering the effects of freeboard gas and end restriction:

1. Dimensionless empirical correlations, typically in the case of kilns without lifters (Austin et al., 1978; Das Gupta et al., 1991; Kramers and Croockewit, 1952; Lebas et al., 1995; Lehmberg et al., 1977; Vàhl and Kingma, 1952);

2. Mechanistic models using geometrical deduction and calculations, firstly proposed by Saeman (1951) and then used in other studies in kilns without lifters (Austin et al., 1978; Venkataraman and Fuerstenau, 1986; Xie et al., 2017) and with lifters (Iwan Harsono, 2009);

3. Semi-dimensionless empirical models in kilns with lifters using the definitions of the underloaded, design loaded and overloaded kilns and related to the airborne and dense phases, which was firstly proposed by Matchett and Baker (1987, 1988) and subsequently used in other studies (Matchett and Sheikh, 1990; Sherritt et al., 1993, 1994, 1996; Pan et al., 2006) in kilns without freeboard gas, with lifters (Abouzeid and Fuerstenau, 1980; Karra and Fuerstenau, 1978) or without lifters (Perron and Bui, 1990); and

11

4. Discrete Element Method (DEM) simulations, considering flow patterns and velocity distributions in the axial direction devices (Pandey et al., 2006; Gyenis et al., 1999; Laurent, 2006). DEM simulation data provide insight and reasonable explanations on the particle level for the practical observations quantitatively and qualitatively.

The second approach is often favored because it is possible to extrapolate outside the operating conditions with reasonable confidence using measurable physical and operational properties, such as initial angle of lifter discharge, lifter hold-up and dynamic angle of repose (Matchett and Baker, 1987).

1.2.3   Solid Mixing in Rotary Drums

A particle traveling in a rotating kiln moves in both transverse and axial directions. Mixing in the transverse plane is much more rapid and is a combination of convective (macro) and diffusive (micro) mixing. Mixing in the axial direction is generally much slower, characterized as purely diffusive, caused by the random collisions of particles in the active region (Clement et al., 1995; Khakhar et al., 1997; Metcalfe et al., 1995; Santomaso et al., 2005; Sherritt et al., 2003; Van Puyvelde, 1999). Generally, lifters can be installed to enhance axial mixing. The key mechanism is an overall convection causing the bulk movement of the material from the inlet of the kiln to the outlet at an average velocity equal to the plug flow velocity (Marias et al., 2005; Mujumdar et al., 2006, Patisson et al., 2000).

A detailed review of the flow regimes within rotating drums, including the experimental and numerical efforts employed in measuring key rheological ingredients (velocity, volume concentration, and flowing layer depth) of these flow regimes is provided by Govender (2016). Granular flows in rotating drums are often described by a flowing free surface layer over a densely packed rising mass that is considered static relative to the rotating drum.
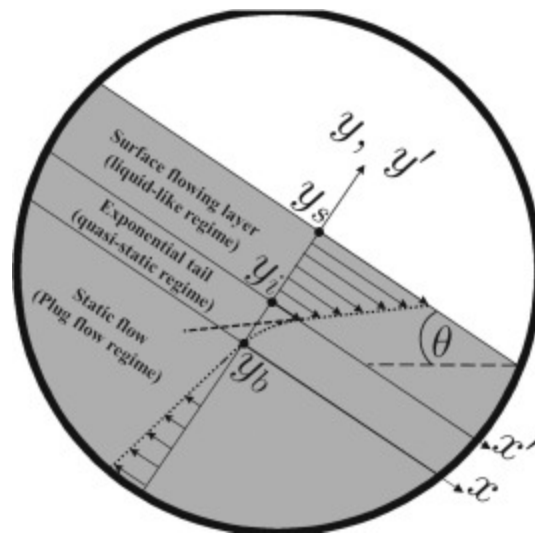
Figure 3. Granular flow in a clockwise rotating drum (Govender 2016).

Fig. 3 is a simple illustration (not to scale) of the typical flow regimes studied primarily in the physics literature, and is based on the schematic given in Midi (2004). Starting at the top of the surface flowing layer (often referred to as the free surface layer) and moving into the bed along the negative y-direction (see Fig. 3), the velocity in the surface flowing layer decreases essentially linearly with depth until very close to the bottom of the flow, where the decrease starts to slow down exponentially with further

increases in depth. The exponential tail is a solid-like regime that is characterized by dense quasi-static flows in which the deformations are very slow, and the particles interact by frictional contact (Roux and Combe, 2002). The linear region is a liquid-like regime that is also densely packed but still able to flow like a liquid with particles interacting by both friction and collision (Pouliquen and Chevoir, 2002; Midi, 2004; Forterre and Pouliquen, 2008). Henein et al. (1983) and Mellmann (2001) classified granular flows in rotating drums by the Froude number (Eq. 2.2):

$$Fr = \frac{\omega^2 R}{g} \tag{2.2}$$

where ω is the angular speed in radians per second, R denotes the internal radius of the drum and g is the usual acceleration due to gravity in meters per second squared.

(a) Slipping or slumping   (b) Surging   (c) Rolling

(d) Cascading   (e) Cataracting   (f) Centrifuging
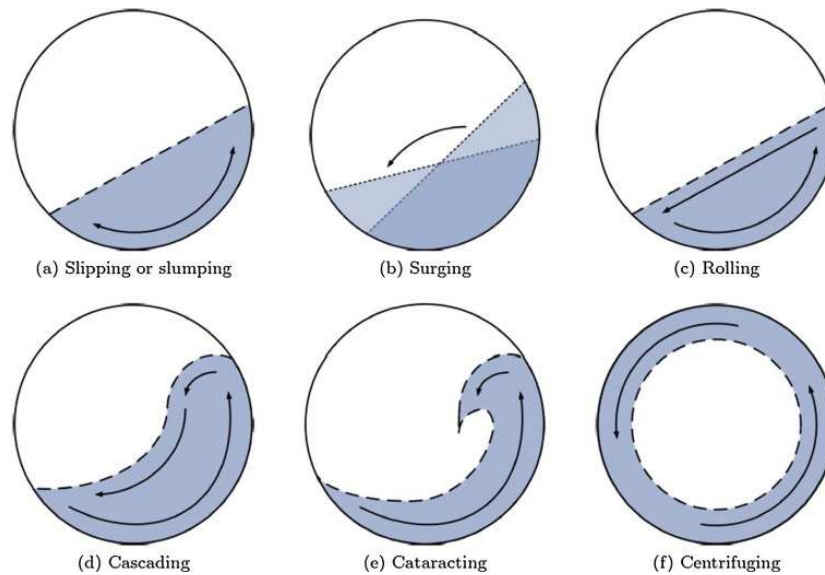
Figure 4. Six categories of rotating drum flows in alphabetical order of increasing drum rotational speed or wall friction (Govender 2016).

There are six categories of rotating drum flows in alphabetical order of increasing drum rotational speed or wall friction summarized by Govender (2016). Below the quasi-static regime shown in Fig. 4, the flow is assumed static relative to the rotating drum, i.e., the grains are assumed to be moving with the same angular velocity as the drum and is often compared to a solid plug moving with the rotating drum, which is called the plug flow. Slipping or slumping (see Fig. 4a) occurs under unfavorable frictional conditions between the solid bed and the cylinder wall. When the cylinder wall is very smooth, sliding may be observed, which is characterized by a bed constantly sliding from the wall (see Fig. 4b). With increasing wall friction, sliding turns into surging. This type of motion is characterized by periodic alternation between adhesive and kinetic friction of the bed on the wall. The solid bed adheres on the rotating wall up to a certain angle of deflection and subsequently slides back en-masse on the wall surface (see Fig. 4c). A continuous circulation of the bed, rolling motion, can be observed when there is sufficient wall friction. This type of motion is characterized by a uniform, static flow of a particle layer on the surface, while the larger part of the bed plug flow region is transported upwards by solid body rotation with the rotational speed of the wall. The bed surface is nearly level and the dynamic angle of repose, which appears only slightly, depends on rotational speed and filling degree (see Fig. 4d). As the rotational speed further increases, the bed surface begins to arch and cascading sets in. The transition to cascading is also dependent on particle size. The height of the arch of the kidney-shaped bed increases with increasing rotational speed (see Fig. 4e). As rotational speed increases, the cascading motion is so strongly pronounced that individual particles detach from the bed and are thrown off into the free space of the cylinder. The release of particles is a characteristic

feature of cataracting motion. Cataracting is characterized by particles from the bed being flung into the gas space. With increasing rotational speed, the number of particles thrown off and the length of the trajectories increase until a uniform trickling veil forms along the diameter (see Fig. 4f).

In the case of further increases of the rotational speed, particles on the outer paths ($r \sim R$, where r is the radius of particles and R is radius of the drum) begin to adhere to the wall and the extreme case of cataracting motion, centrifuging, occurs. Theoretically, centrifuging reaches its final stage when the entire solid material is in contact with the cylinder wall as a uniform film. This state is, however, only achieved at extremely high rotational speeds.

1.2.4   Heat Transfer in Rotary Drums

The heat transfer in a rotary drum is unique compared to other furnaces because it involves not only the gas and the moving bed of solids, but also the rotating drum wall. These rotary drums can be heated in two ways, directly or indirectly, depending upon the process. In the directly heated rotary drum, fuel (coal, gas or oil) goes through a combustor or burner where it is mixed with oxygen to generate high temperature gas (Nafsun et al., 2016). The hot gas is then introduced into the kiln in a direction either co-current or counter-current to the solids flow. However, in an indirectly heated drum, the heat tube is housed in casing and the combustion occurs within the case but external to the drum, while the solids are processed inside the kiln, or the drum walls are heated using hot air blowers or electrical heaters. Therefore, indirect heating of drums provides

16

clean heating and is flexible in controlling the heat transfer for solids. An indirectly heated rotary drum is used when the material must avoid direct contact with the hot gas. The heat transfer, in this multiphase system, between the gas, drum wall, and solid bed includes conduction (particle-particle, particle-fluid-particle, particle-fluid-wall, and particle-wall), convection (particle-gas, wall-gas), and radiation (particle-particle, particle-environment).
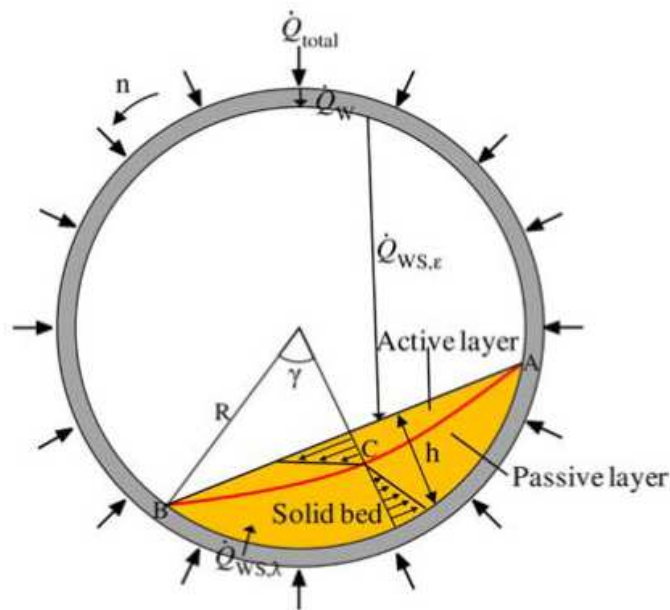
Figure 5. Schematic of heat transfer in the cross-section of indirectly heated rotary drums (Nafsun & Herz 2016).

As the drum rotates, the heat stored in the drum wall is transferred to the solid bed. In indirectly heated rotary drums, heat is given to the outer shell of the drum wall. The heat transfer path in an indirectly heated rotary drum is shown in Fig. 5. Heat is transferred to the solid bed in two ways, across the active layer of the solid bed found

near the bed material surface where the particles avalanche and cascade downward, and the passive layer of the bed found near the drum wall, where particles move as a solid body (Chaudhuri et al., 2010; Dhanjal et al., 2004; Ding et al., 2001; Gui; et al., 2013; Komossa et al., 2015; Le Guen et al., 2013; Liu and Specht, 2010; Lybaert, 1987; Nafsun et al., 2017, 2016; Nguyen et al., 2015; Shi et al., 2008; Thammavong et al., 2011; Wes et al., 1976). In indirect heating, the drum wall is heated externally with $\dot{Q}_{total}$. The heat from the source, $\dot{Q}_W$, is transported to the wall and then conducted through the wall. A part of the heat radiates to the free solid bed surface, $\dot{Q}_{WS,\varepsilon}$, and the other part is conducted from the covered wall surface to the solid bed in the contact region, $\dot{Q}_{WS,\lambda}$.

There are some unique challenges associated with heat transfer in rotary kilns. Typically, the kiln is inclined at a slight angle to the horizontal direction and the solid bed is at an angle to the kiln due to rotation. Two distinct regions are present in the cross-section of the kiln, i.e., the freeboard and the solid bed. The gases flow in the freeboard, while the solid material occupies the bed. The bed moves, but not in as well-defined a manner as a liquid or a gas. The bed is constantly tumbled and mixed by the kiln rotation and is continuously being exposed to the heat sources, i.e., under the bed, on top of the bed, and also with the rotating kiln wall. Depending on applications, gases may evolve from the bed, which can be an additional source of energy. Materials processing may also be exothermic or endothermic depending on the involved chemical reactions (Martins et al., 2001; Ortiz et al., 2005; Patisson et al., 2000; Ramakrishna et al., 1999). Some processes may involve three phases if the solid feed material melts and becomes a liquid

in the kilns, in addition to the combustion gases and possible gases evolving from the process.

The heat transfer in an indirectly heated drum is influenced by a wide range of process parameters, such as specific heat capacity, particle size, particle size distribution (PSD), particle shape, particle density, thermal conductivity, rotational speed, fill level, and equipment design parameters (diameter, length, and inclination angle). In the past, experiments have been performed to understand the heat transfer mechanisms and the effects of process parameters in rotary drums (Komossa et al., 2015). Another researcher, Nafsun et al. (2016), conducted experiments to investigate the contact heat transfer between the wall and solid bed, using monodisperse solid beds of steel spheres, animal powder, cement clinker, quartz sand, glass beads, and expanded clay, with variation in rotational speed (from 1 to 6 rpm) and a constant filling degree. They found that the contact conduction heat transfer coefficient increases with higher rotational speeds. They also found that the effective physical properties (bulk density, heat capacity, and conductivity) have a significant influence on the contact heat transfer coefficient. At higher effective physical properties, the heat transfer coefficient increases due to the lower penetration resistance inside the solid bed. Furthermore, as the particle diameter increases, the contact heat transfer coefficient decreases. This is due to the higher contact resistance between the covered wall and the first particle layer of the solid bed. Chaudhuri et al. (2010) also investigated the contact conduction mechanism in an indirectly heated drum. They studied the effects of thermal conductivity, rotation speed, and baffles using alumina (2 mm diameter) and cylindrical silica particles (2 mm

diameter and 3 mm long). The drum was filled up to 50 % of its volume, and the walls were kept constant at 100 °C. They found that materials with higher thermal conductivity heated faster and rotation speed had minimal impact on heat transfer. They also found that the baffles promote heat transfer and thermal uniformity within the bed. Most recently, Njeng et al. (2018) studied the heat transfer coefficient between the wall and solids in an indirectly heated flighted rotary drum using nodular sand with an average particle size of 0.55 mm. A model based on dimensional analysis was proposed to calculate the wall to solid heat transfer coefficient for low to medium heating temperatures (100–500 °C). They found that when radiation is neglected, the wall-to-solid heat transfer coefficient varied by up to 24 %, and convection had little or no effect on this coefficient.

Miller et al. (1942) conducted the first extensive study of heat transfer in rotary dryers and concluded that the total rate of heat transfer is affected by the number of flights. Recently, Chaudhuri et al. (2006) used DEM simulations to conduct a detailed study on the effects of baffles, baffle size, the number of baffles, and adiabatic baffles, on heat transfer using copper particles of radius 2 mm in a 15.0 cm diameter and 1.6 cm long calciner. They found that baffles enhance heat transfer and thermal uniformity, the L-shaped baffles are more efficient than the square-shaped baffles, and the heated baffles enhance heat transfer within the calciner. They also found that an increase in the number of baffles caused enhancement in heat transfer within the calciner, as well as concluded that the thermal uniformity of the bed is directly proportional to the number of baffles.

A few researchers have investigated the effect of rotation speed on heat transfer in rotary drums with heated walls (Chaudhuri et al. 2006; Nafsun et al. 2016; Figueroa et al. 2010; Sunkara et al. 2013; Komossa et al. 2015). Komossa et al. (2015) conducted experiments to study the effect of rotation speed (between 1 to 9 rpm) on the heat transfer using 2 mm diameter monodisperse glass spheres, maintaining the bed bulk movement within the rolling motion mode (with 15% fill level and constant wall temperature of 474 K). They discovered that at the free bed surface, the frequency distribution of the effective heat transfer coefficient is based on the particle velocities. Analogously to the particle velocity distribution, the mean value of the frequency distribution of the effective heat transfer coefficient increases with increasing rotational speed, and the distribution broadens. Emady et al. (2016) studied the effect of rotation speed and thermal conductivity of 4 mm diameter alumina particles using DEM simulations. The rotary drum modeled had a constant slope, constant fill, constant diameter, fixed particle size with a normal size distribution, and no baffles. They found that the rotation speed has a minimal effect on the heat transfer between the drum walls and the process material, with low conductivity, and the sensitivity of the heat transfer to rotation rate increases with increasing conductivity. One interesting finding reported by Chaudhuri et al. (2010) showed increasing rotation speed decreases heat transfer and temperature uniformity on a per-revolution basis, but the effect disappears on a per-time basis.

Fill level is another important parameter which plays a significant role in the heat transfer in rotating drums. Chaudhuri et al. (2006) found that faster mixing is possible for the lower fill fraction case, which causes rapid heat transfer from the drum wall to the

21

granular bed with a more uniform temperature distribution. Studies show that the mixing rate increases with rotation rate and with decreasing the fill level of the drum (Hogg et al. 1969; Hogg & Fuerstenau 1972; Orpe & Khakhar 2001; McCarthy et al. 1996; Lehmberg et al. 1977). In another work, Figueroa et al. (2010) compared mixing versus heating rates in various rotating systems. They discovered that increasing mixing rates can be either unfavorable or enhance the heating of the granular bed, depending on the Peclet number (ratio of the thermal energy convected to the thermal energy conducted). Also, the rotary drum system exhibits a faster heating rate when the ratio of thermal conductivity to heat capacity increases (Xie & Feng 2013). Nguyen et al. (2015b) performed 2D DEM simulations to investigate the effects of thermal conductivity, heat capacity, fill level, rotation rate, and particle size on heat transfer. They found that small particle size, high rotation rate, low fill level, low heat capacity, and high thermal conductivity each resulted in faster heating.

Little previous work has been done on understanding the effect of particle size on heat transfer in rotary drums. Most recently, Mohseni and Peters (2016), using XDEM, found that with smaller particles in the system, the heat transfer rate is higher. As the particle size increases, the heat transfer coefficient decreases due to the higher contact resistance between the covered wall and the first particle layer of the solid bed (Nafsun et al. 2016). The heat transfer study gets more complicated when the granular bed has particles of different sizes. An experimental study by Dhanjal et al. (2004) looked at the effects of polydispersed particles on heat transfer in a rotary kiln. It was observed that there was little influence of particle segregation on overall heat transfer and there was

inadequate particle mixing which caused radial temperature gradients. The polydispersed

particles considered in this study (de Silva et al., 2000) were made up of two distinct

sizes of monodispersed particles, i.e., two solid phases with the same thermo-physical

properties (like density, conductivity, shape, and heat capacity) and distinct particle size

(monodispersed). However, ideally, granular material is not monodispersed but

polydispersed, where each particle possesses a unique diameter.

1.3   Thesis Objectives

1. To investigate the segregation of bi-disperse granular materials during discharge
   from a 3D-printed hopper.

2. To investigate the effects of particleand wall roughness on the discharge of silica
   beads through a hopper. A glass blown hopper and a 3D-printed hopper are used
   toachieve wall roughness.

3. To verify and validate the contact conductive heat transfer model implemented in
   MFIX-DEM, an open-source DEM code, using an indirectly heated rotary drum.
   The conduction model is validated with monodispersed alumina particles using the
   DEM simulation and experiment presented by Chaudhuri et al. (2010).

4. To investigate the effects of operational parameters on the overall heat transfer
   inside a rotary drum.

   a. Perform experiments to investigate the effect of fill level on the average bed
      temperature.

   b. Perform DEM simulations to investigate the effects of rotation speed,
      particle size distribution, and rolling friction.

5. To construct a lab-scale rotary drum and develop a new non-invasive temperature measurement technique using infrared (IR) thermography.

    a. To present a detailed IR calibration methodology and data acquisition process.

    b. To investigate the effects of rotation speed and fill level on the conduction heat transfer in the rotary drum constructed.

2   GRANULAR SEGREGATION IN DISCHARGING CYLINDRICAL HOPPERS USING EXPERIMENTS

2.1   Abstract

The segregation of granular materials due to differences in particle properties occurs during a variety of handling and transport processes, such as flow from a hopper. In the present work, experiments are used to investigate segregation of spherical, bidisperse granular materials during discharge from a hopper. Specifically, two types of micro-glass beads with distinct size distributions are used to fill the hopper in two possible packing arrangements, i.e., well-mixed and layered configurations, with varying mass (particle number) ratios. The experimentally obtained discharge dynamics was calculated as the normalized discharge mass fraction for one of the phases versus the overall discharge mass fraction (γ_f^N). For the well-mixed configuration, due to segregation effects, the fine particles clustered at the hopper bottom towards the end of the discharge, leading to an increase of γ_f^N towards the end of discharge. For the layered configuration, the coarse particles packed at the hopper bottom discharge first, opening a channel for the fine particles on the top. Therefore, the resulting γ_f^N remained zero for a while (before a channel was opened up) and monotonically increased as the discharge proceeded after the channel was open.

2.2   Introduction

Particulate systems play a significant role in many industries, like pharmaceuticals, polymers, mineral processing, munitions, energy, food processing, environment, and agriculture. The discharging of granular materials from a hopper is a critical topic of industrial importance, and the discharge flow rate from hoppers is of continuous research interest. Granular materials typically consist of particles with a distribution of sizes, shapes, and densities, which may induce segregation of the material upon handling. Since the product quality is often contingent on maintaining blend homogeneity, segregation of granular materials is undesirable for many solids handling processes. Therefore, it is important to examine the causes and extent of segregation in various systems. This work uses experiments to investigate the segregation of polydispersed silica particles during hopper discharge.

2.3   Experimental Setup

Experiments were carried out using two types of polydisperse particles with varying initial packing configurations. The hopper used in the experiments (shown in Fig. 6) is 3D printed using a Strata- sys Dimension 1200es SST (Stratasys Ltd., MN, USA), with ABSplus thermoplastic. It contains a cylinder of 12.5 cm height and 12.5 cm diameter, connected to a cone with a height of 3.5 cm and 55◦ cone angle. The bottom of the hopper cone is further connected to a short cylinder of height 1.3 cm and diameter 2.5 cm. The hopper is leveled and clamped to a support stand. A glass slide gate is used to close and open the hopper outlet, to fill and discharge, respectively. The granular

materials used in the experiments are silica beads (soda-lime silica glass). The silica

beads are purchased from Potters Industries, PA, USA; with particle density 2.5 g/cm^3 in

different sizes. The particles are further sieved to narrow the particle size distribution

(PSD). The sieved particles are analyzed using a Malvern Morphologi G3SE (Malvern

Instruments Ltd., UK), and two distinct sized polydisperse silica beads with a bi-modal

size distribution (shown in Fig. 7 and 8) are used for the experiments. Specifically, the

system can be considered to contain two phases of solid particles, each possessing a

distinct normal size distribution, with the same physical properties.

Figure 6. Experimental set-up showing the 3D printed hopper clamped to a stand
and placed above a balance with beaker.

The fine particles possess a normal distribution with a mean of 1.5 mm and

standard deviation of 0.3 mm, and the coarse particles possess a normal distribution with

a mean of 2.9 mm and standard deviation of 0.1 mm (see Fig. 7 and 8). While the particles discharge through the hopper, they become tribocharged and tend to stick to the walls of the hopper. To remove any charging of the particles during discharge, the particles are treated with an anti-static solution. The anti-static solution is pre- pared by dissolving 1 ml of ASA anti-static agent (Electrolube, UK) into 100 ml of ethanol. No change in the discharge dynamics and segregation is observed before and after the particles are coated with the anti-static solution.
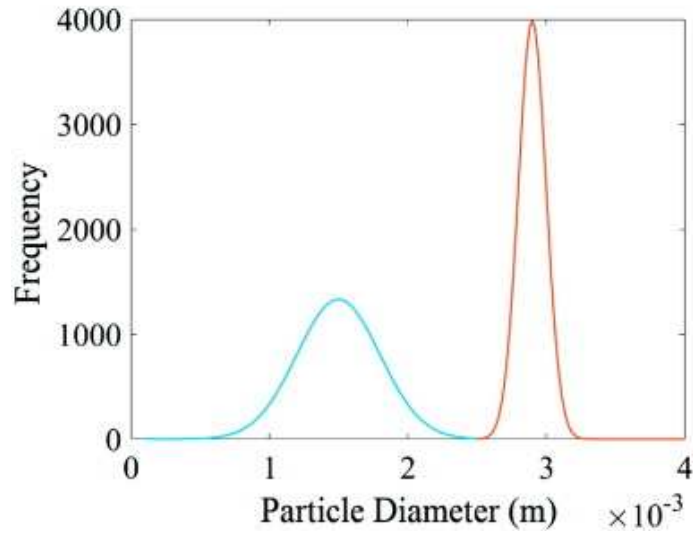
Figure 7. A bi-modal particle size distribution (i.e., number frequency vs. particle size) was employed, which includes two normal distributions for fine and coarse silica bead particles.

Figure 8. Silica beads: Normal distribution of the fine particles with mean of 1.5 mm and standard deviation of 0.3 mm, colored in red; and the coarse particles with a mean of 2.9 mm and standard deviation of 0.1 mm, colored in green.

2.4   Methodology

The masses of the fine and coarse particles used in the experiments are 580 g and 420 g, respectively. Two initial packing configurations are prepared using the fine and coarse particles. In the first configuration, the fine and coarse particles are well mixed. For this, both the fine and coarse particles are divided into 10 equal portions. One portion of fine particles is mixed with one portion of coarse particles using a Turbula T2F Shaker-Mixer (Glen Mills Inc., NJ, USA). The same procedure is repeated with the remaining 9 portions to produce 10 equal portions of well-mixed fine and coarse particles. The hopper outlet is closed, and each portion is loaded slowly into the hopper, to minimize segregation due to free fall. The particle bed is leveled after each portion is

loaded. In the second configuration, the coarse particles are first packed at the bottom of the hopper (with the outlet closed). Then the fine particles are loaded on top of the coarse particles to form a layered packing. Each layer is leveled after loading into the hopper. We note that these configurations were also used by Ketterhagen et al. (2007). The discharge experiment is carried out using a discontinuous sampling method (Chu 2008). The outlet of the hopper is opened, and samples of equal mass are collected using the discontinuous sampling method. The initial and final arrangement of particles, for both mixed and layered configurations, are shown in Fig. 9. The collected samples are sieved and weighed to determine the mass of fine and coarse particles.

The discharged mass fractions of both the fine and the coarse particles are determined, and the segregation data is plotted as the normalized mass fraction of fine (γ_f^N) and the overall discharged fractional mass (γ), using Eq. (3.1) and (3.2).

$$\gamma_f^N = \gamma_f^{discharge}/\gamma_f^0 \tag{3.1}$$

$$\gamma = m^{discharge}/m^0 \tag{3.2}$$

where, γ_f^N is the normalized fine mass fraction of the discharged particles, γ discharge is the fine mass fraction of the discharged particles, is the fine mass fraction in the initial packing configuration, $m^{discharge}$ is the overall discharged mass fraction, m^0 discharge is the total discharged mass and m^0 is the mass of the initial particle packing. During the experiments with the well-mixed configuration, segregation occurs while loading. Therefore, each experiment is replicated five times to minimize the effects of

any non-homogeneous regions on discharge segregation results, for both well-mixed and layered configurations.
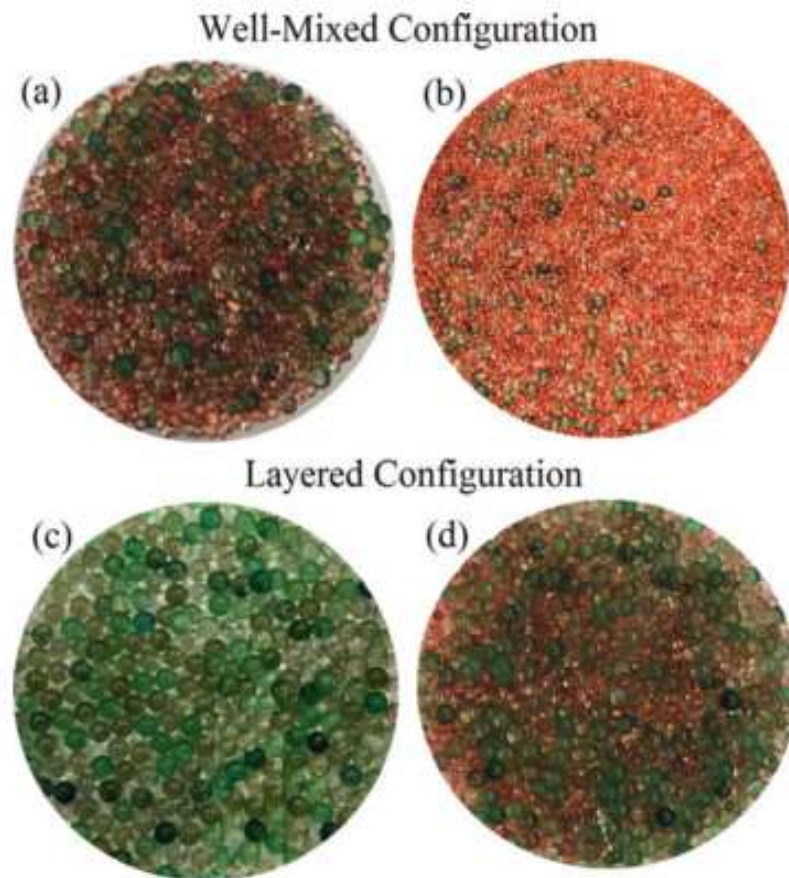
Figure 9. Images of the discharged smaples from the hopper. (a) First discharged sample from the well-mixed configuration. An approximately equal number of fine and coarse particles are discharged. (b) Last discharged sample from the well-mixed configuration. A majority of fine particles are discharged. (c) First discharged sample from the layered configuration. Only coarse particles are discharged. (d) Last discharged sample from the layered configuration. A mixture of both fine and coarse particles are discharged.

2.5 Results and Discussion

2.5.1 Well-mixed configuration
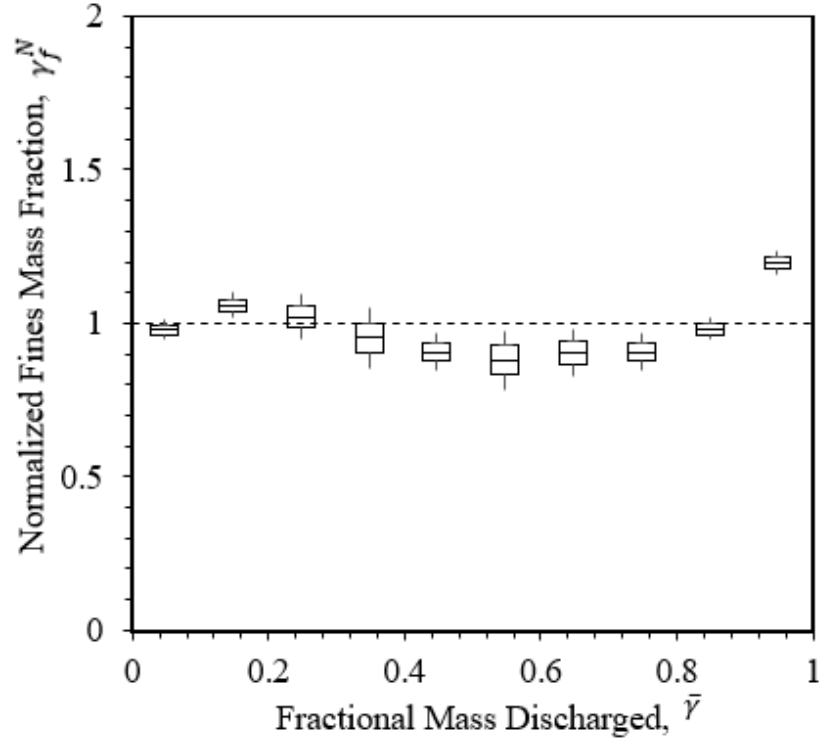
Figure 10. Discharge dynamics are quantified using the normalized fine mass fraction of the discharged particles vs. the overall discharged mass fraction for the well-mixed configuration.

In the ideal case that during the entire discharge process, the packing configuration stays well mixed, the resulting $\gamma_f^N - \gamma$ curve would be a simple constant function with value 1. However, due to segregation effects, the fine particles cluster at the hopper bottom towards the end of the discharge, leading to an increase γ_f^N towards the end of discharge (see Fig. 10). It can be seen that the data tends to deviate more from the

ideally mixed case (i.e., the constant function), indicating a stronger segregation effect during the discharge. It is note that in an "ideally mixed case", there will be no aggregation of particles of similar sizes during the entire discharge process. This situation is not possible in practice, as the particles during a discharge process always gain kinetic energy and thus, inevitably form aggregations of different sizes. Therefore, the segregation in the system is mainly due to discharge and becomes significant towards the end of the discharge process.
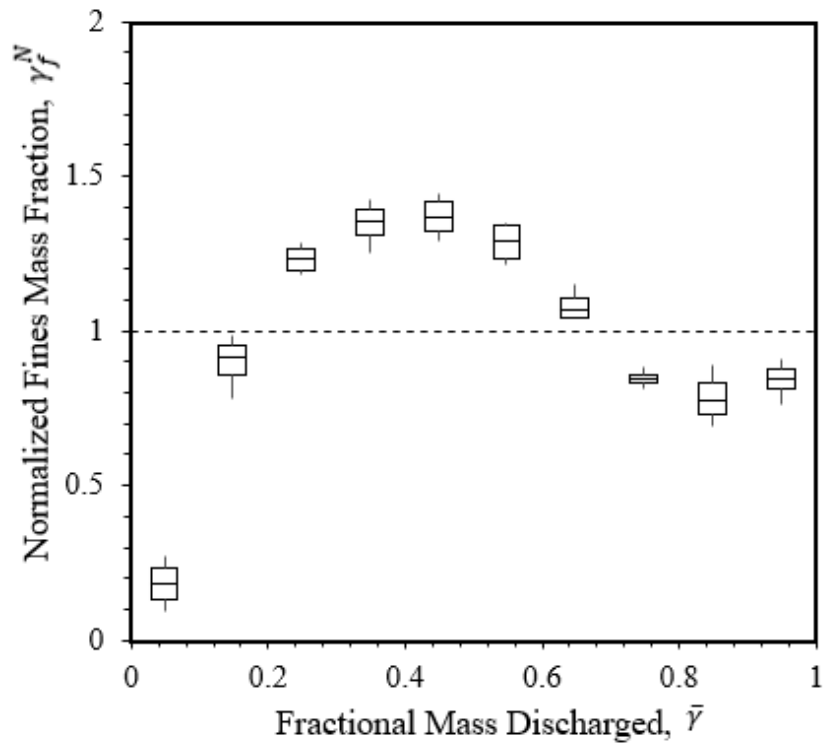
Figure 11. Discharge dynamics are quantified using the normalized fine mass fraction of the discharged particles vs. the overall discharged mass fraction for the layered configuration.

33

2.5.2 Layered configuration

In this case, the coarse particles packed at the hopper bottom discharge first, which opens up a channel for the fine particles on the top. Therefore, the resulting γ_f^N remains zero for a while (before a channel is opened up) and is monotonically increasing as the discharge proceeds after the channel is open. Towards the end of discharge, since most of the fine particles in the hopper are gone, γ_f^N begins to decrease and finally starts to fluctuate due to a very small number of fine particles remaining in the hopper (see Fig. 11). It can be seen that the data tends to deviate more from the ideally mixed case (i.e., unity) compared to the simulation results. Although, in this layered configuration, the coarse and fine particles are separately packed in their own layers, within each layer the locally segregated regions still exist (due to the polydispersity of particles within the same solid phase) in the experimentally prepared initial configurations. This leads to the observed stronger segregation effects during the discharge process.

It is predicted that the channel for fine particles is opened during the discharge. Due to the geometry of the hopper, the particles in the central region corresponding to a virtual extension of the cylinder-shaped outlet at the hopper bottom always discharge first, regardless of the initial packing configurations in the hopper. The fast flow of discharging particles in this central region generates a pressure on the remaining particles and pushes them against the container wall. In the layered configuration, the coarse particles are packed at the bottom of the hopper and fine particles are then stacked on top.

Thus, once the discharge process starts, the coarse particles in the central region discharge first, which efficiently opens a channel for the fine particles that were originally packed on top of the coarse ones.

2.6   Conclusions

This work uses experiments to investigate the segregation of polydispersed silica particles during hopper discharge. A 3D-printed lab-scale hopper with two size ranges (diameters of 1.5 mm and 2.9 mm) of silica particles is used for the study. The hopper is filled in two ways, with the two layers of particles, in a well-mixed and layered configuration. The particles are discharged and collected transiently in equal volumes. Preliminary results show that a central flow channel is formed, and the top layer begins to deflect and forms a V-shaped surface. The incline formed promotes segregation via percolation whereby the fine layers shift downward into the inert or slow-moving material below, while coarse particles tend to roll down the incline toward the hopper centerline. As a result, the coarse layers start to discharge. Since the velocities are greatest near the centerline, the fines-depleted material that accumulates near the hopper centerline discharges quickly. As discharge continues, fines-rich material near the hopper walls is discharged, resulting in a peak at the end of the segregation profile. We propose to study the same batch of particles, where the particles will be subjected to etching, thereby increasing the surface roughness. Those particles will be used to investigate the friction effects on segregation.

3   EFFECT OF PARTICLE AND WALL ROUGHNESS ON DISCHARGE OF SILICA BEADS THROUGH HOPPERS

3.1   Abstract

The effect of surface roughness on the discharge rate of a hopper is studied. The roughness of both the wall surface and the particle surface are varied to investigate their individual effects on discharge. Spherical silica beads with a mean diameter ranging between 0.16 to 4 mm are etched using an NaOH base etching technique. The wall roughness is varied by constructing two hoppers with different materials. A 3D-printed hopper with ABSplus thermoplastic and a glass-blown borosilicate glass hopper are used for the wall roughness studies. Results show that the discharge rate increases with increasing wall roughness. The discharge rate is estimated to be inversely proportional to (the root mean square roughness of the particle)$^{0.59}$.

3.2   Introduction

The flow of granular materials through storage vessels such as hoppers and bins is a common and important industrial unit operation. Many industries, including chemicals production, polymer production, pharmaceutical tableting, powder manufacturing, mineral mining, agricultural and food processing, and plastics manufacturing encounter handling and storing of granular materials in some stage of their processes. Besides providing storage solutions, hoppers are often used as links between various unit operations in many industrial processes to provide buffering to control flow variation and operational instability. This becomes crucial in particulate processes,

36

as their bulk behavior is generally unpredictable and unsteady. Granular material often does not flow reliably or uniformly in the course of handling and processing, resulting in production loss, extra labor, plant downtime, poor quality control, and inconsistent materials.

The hopper discharge behavior is associated with the complex flow patterns of granular materials inside the hopper, as well as the hopper properties. In order to predict the discharge rate of hoppers, an extensive array of studies were historically performed, such as Enstad (1975), Williams (1977), and Jenike (1967). Parameters that have been studied include single particle parameters (e.g., density, hardness, hygroscopicity, light scattering/adsorption, shape, size, and surface); bulk particle parameters (e.g., adhesion, bulk density cohesion, conductivity, electrostatic charge, moisture content, pore size distribution, porosity, shear strength, size distribution, surface area, and compressive strength), and hopper design parameters (e.g., fill height, friction, hopper width, hopper angle, and hopper outlet width) (Saleh et al., 2018). In general, there are two types of friction, namely, particle-particle (P-P) friction and particle-wall (P-W) friction. Research showed that differences in P-W and P-P frictional forces affect discharge rate and induce segregation. Ketterhagen et al. (2007) studied segregation profiles for discharge from a wedge-shaped hopper, using a mixture of fine and coarse particles, in which the P-W friction coefficient and the P-P friction coefficient were varied. It was found that decreasing the P-W friction created a more mass flow-like behavior in the hopper, minimizing the tendency for fines to be retained in the hopper until the end of the discharge. Also, increases in the P-P friction produced the same effects as decreasing the

P-W friction. Increasing the P-P friction inhibited the percolation of fines through the mixture to the bottom of the hopper, resulting in a coarse-rich discharge at the end.

The effect of wall friction in pharmaceutical materials was first studied in 1982, and it was found that, in general, the wall friction increased with increasing surface roughness and decreasing particle size (Jolliffe and Newton, 1983a, 1983b, 1982). In their later work, in 1990, Jolliffe and Newton found that there was a weak trend of greater wall friction with an increasing surface roughness of the wall and decreasing particle size of the powders (Jolliffe and Newton, 1983a). In general, it has been assumed that the wall surface roughness is an order of magnitude less important in influencing segregation than particle size or density (Pohlman et al., 2006). Pohlman et al. (2006) studied segregation patterns of a binary mixture of smooth and rough surfaced chrome steel beads in 2D and 3D rotating tumblers. Their experimental and simulation results showed that surface roughness affected the angle of repose. However, the influence of particle and wall surface roughness on particle discharge and segregation has received little attention in granular hopper flow studies.

The above-mentioned previous studies show that particle roughness has a significant impact on granular processes. Therefore, the current work focuses on studying the hopper discharge rate by varying the roughness of the hopper wall and the particles. Eleven batches of silica beads with different sizes ranging between 0.125 to 4 mm are used for this study. The beads are roughened through a base etching technique, by varying the etching time to produce different particle roughness levels. Two hoppers, constructed by glass blowing and 3D printing, are used to obtain different wall friction

levels. The surface properties of the wall and the particles are characterized using a non-contact optical profilometer.

3.3   Materials and Experimental Procedure

Silica beads purchased from Potters Industries, PA, USA, are used as the granular material for this study, with particle density of 2.5 g/cm^3 in different sizes. To ensure the particles are close to monodisperse, they are sieved to narrow the size range using standard sieves. A total of eleven batches are prepared with varying size ranges and mean diameters. Table 1 provides the particle properties specific to each size range. The sieved particles are analyzed using a Malvern Morphologi G3SE (Malvern Instruments Ltd., UK), a microscopic technique for particle size characterization. The mean diameter d_{32} of the sample and the sphericity are determined.

In order to induce roughness on the surfaces of the particles, a 2M sodium hydroxide (NaOH) etching solution is prepared. The NaOH solution is prepared by measuring 72 g of sodium hydroxide pellets, which are dissolved in 900 ml of distilled water. Potassium hydrogen phthalate (KHP) solution is used for standardizing the NaOH solution using the titration method. To prepare the KHP solution, 6 g of KHP are dissolved in 100 ml of distilled water. Two to three drops of phenolphthalein are used as an indicator, and are added to the KHP solution. The amount of NaOH used for titration is recorded once the clear KHP solution turns pink, and the concentration of NaOH is determined. The silica spheres are treated with the etching solution in a beaker and then set on an automatic swirler at 200 rpm, in order to prevent resistance in the mass transfer

from the surfaces of the spheres to the etching solution. The etching time is varied

between 1 to 20 min. Samples are immediately rinsed upon etching with DI water to

prevent further exposure to the etchant, and are then dried. To remove any electrostatic,

the samples are treated with an anti-static solution. The anti-static solution is prepared by

dissolving 1 ml of ASA anti-static agent (Electrolube, UK) into 100 ml of ethanol. The

dried samples are soaked in the ethanol and anti-static solution overnight. As ethanol is

volatile, the solution evaporates, leaving behind samples coated in antistatic. Micrographs

of a 2 mm particle before and after etching are presented in Fig. 12.

Table 1. Properties of the Silica Particles Used in Experiments.

Sample ID	Diameter Range (mm)	Mean Diameter, d_{avg} (mm)	Sphericity, ϕ
1	0.125 - 0.180	0.16	0.95
2	0.180 - 0.250	0.21	0.95
3	0.250 - 0.350	0.27	0.95
4	0.350 - 0.500	0.46	0.95
5	0.500 - 0.600	0.57	0.95
6	0.600 - 0.710	0.63	0.96
7	0.710 - 0.850	0.78	0.95
8	0.850 - 1.000	0.97	0.96
9	1.000 - 1.200	1.06	0.96
10	2.000 - 2.250	2.10	0.98
11	3.984 - 4.016	4.00	0.98
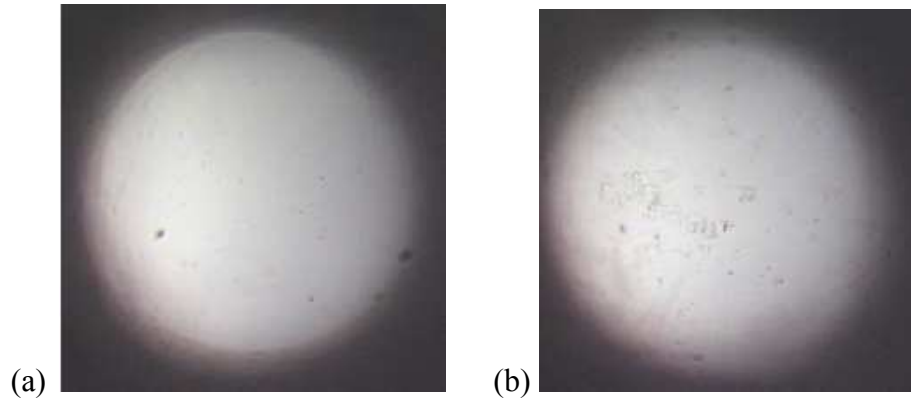
Figure 12. Image analysis micrographs from the Malvern Morphologi G3SE: (a) a 2 mm silica particle and (b) a 2 mm etched silica particle (20 min).

To study the effect of wall roughness, two types of cylindrical hoppers are constructed with different materials. The cylindrical hopper contains a cylinder of 12.5 cm height and 12.5 cm diameter, connected to a cone with a height of 3.5 cm and 55° cone angle. The bottom of the hopper cone is further connected to a short cylinder of height 1.3 cm and diameter 2.5 cm (see Fig. 13a). One hopper is 3D-printed using a Stratasys Dimension 1200es SST (Stratasys Ltd., MN, USA), with ABSplus thermoplastic (see Fig. 13b). Another hopper is constructed with the same dimensions via glass blowing with borosilicate at the Arizona StateUniversity Glassblowing Facility (see Fig. 13c). The hoppers are leveled and clamped to a support stand, as shown in Fig. 14 (Chen et al., 2017). The entire setup is placed above an analytical balance, which is used to record the mass of sample discharged. A glass slide gate is used to close and open the hopper outlet, to fill and discharge, respectively. To determine the discharge rate, the hopper outlet is closed using a slide gate, and the desired sample is loaded slowly into the hopper, to minimize segregation due to free-fall. The particle bed is leveled after loading

41

using a spatula. The discharge experiment is carried out using a continuous sampling method (Standish and Kilic, 1985). The outlet of the hopper is opened, and the particles are allowed to discharge under gravity. The discharged particles are collected in a beaker placed under the hopper outlet. The balance is connected to the computer and the WinWedge software (TAL Technologies, Inc.) is used to record the mass over time.
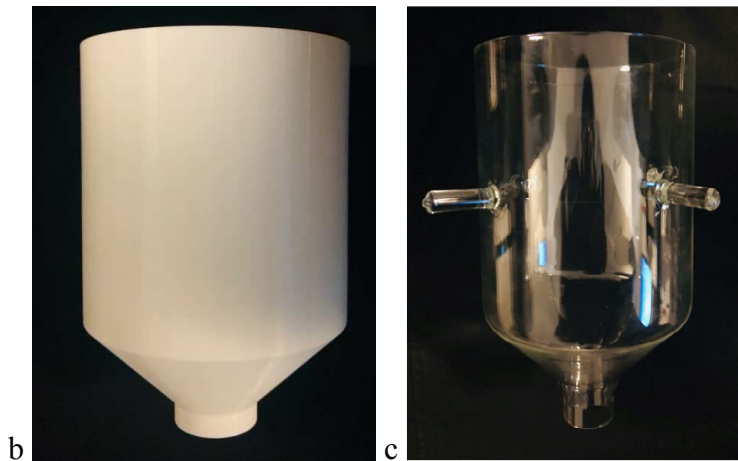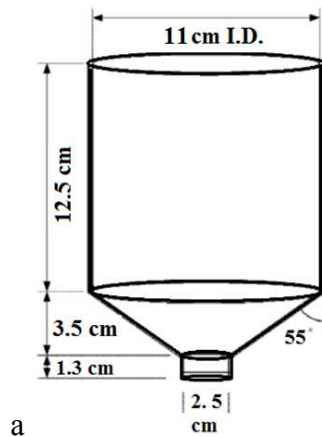
Figure 13. Hoppers constructed for the experiments: (a) a schematic showing the dimensions of both the hopper, (b) a 3D-printed hopper, and (c) a glass-blown hopper.

Figure 14. Experimental setup of the hopper. Clamped 3D-printed hopper with a beaker, for collecting discharged particles, placed on an analytical balance to measure the mass of discharged particles for sampling (Chen et al., 2017).

3.4   Particle roughness

Previously, researchers have used atomic force microscopy (AFM) to measure particle surface roughness (Lamarche et al., 2017; Meyer et al., 2014; Vaziri Hassas et al., 2016). In AFM, an oscillating tip or a cantilever is used to measure the particle roughness. The oscillating height of the tip or cantilever is determined from a baseline, which is in turn determined based on the shape of the sample. A baseline is calculated by considering all measured points on the cantilever path line. Furthermore, the surface roughness is calculated based on the difference between the probing path line and the baseline. As the sample in this case is a spherical particle, there may be an error

in the baseline calculation due to the variation in the height of the tip from the shape of the sample. Also, AFM requires force feedback and physically touching the surface, so while it is extremely sensitive and provides high Z resolution (vertical direction), it is sensitive to soft surfaces and the tip can become contaminated by the surface. This technique can also be destructive to some surfaces. In addition, as it involves physical movements in the X, Y and Z directions while maintaining contact with the surface, it is slower than non-contact techniques. The tip size and shape can influence the measurements and limit the lateral resolution. Therefore, the current work utilizes a non-contact optical technique using an optical profilometer.

Optical profilometer instruments enable precise, quantitative, non-contact surface measurement and characterization of microscale and nanoscale surface features, capturing up to two million data points in just seconds. The key component to this technique is directing the light in a way that it can detect the surface in 3D with a height resolution better than 1Å, and reconstruct the surface. A1 shows the methodology of the optical profilometer. Roughnesses of the particles are determined using the Zygo ZeScope Instruction V.2.0 profilometer. In general, the surface morphology of a sample is reported as the root mean square roughness, R_q, which is calculated from the mean line within the assessment length, L:

$$R_q = \sqrt{\frac{1}{L}\int_0^L y^2(x)dx} \qquad (4.1)$$

where x is the number of measured points and y is the height of each measured point.

3.5   Results and discussions

The roughness value, R_q, is obtained from the profilometer analysis using 10 particles from each sample. The roughness of 2.1 mm mean diameter particles as a function of etching time are presented in Fig. 15. Here, the R_q values increase with increasing etching time, which is consistent with the results obtained by acid etching presented in Vaziri Hassas et al. (2016). Visual topographic images after different etching times of the 2.1 mm mean diameter particles are presented in Fig. 16.
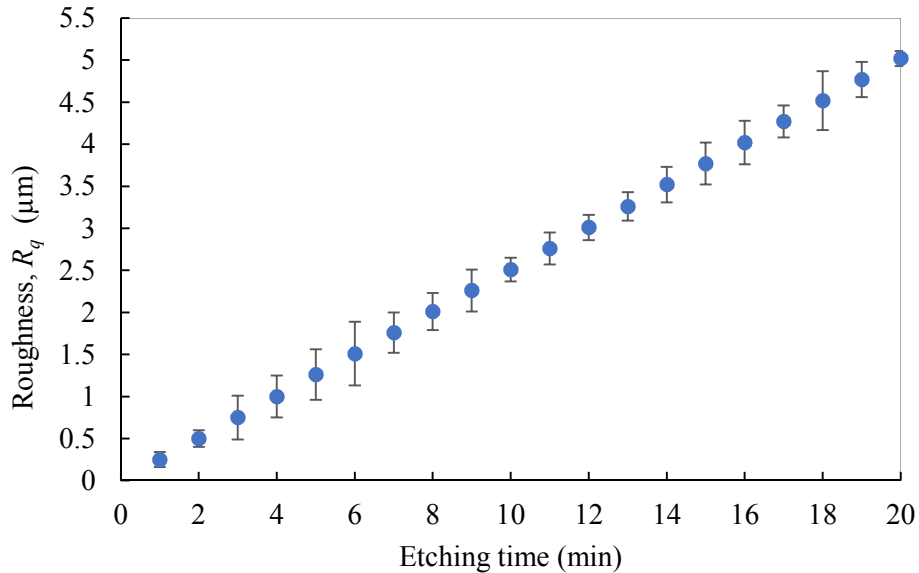
Figure 15. Root mean square roughness, Rq, values of etched 2.1 mm silica beads evaluated by an optical profilometer versus etching time. Error bars represent the standard deviation for 10 particles.

45
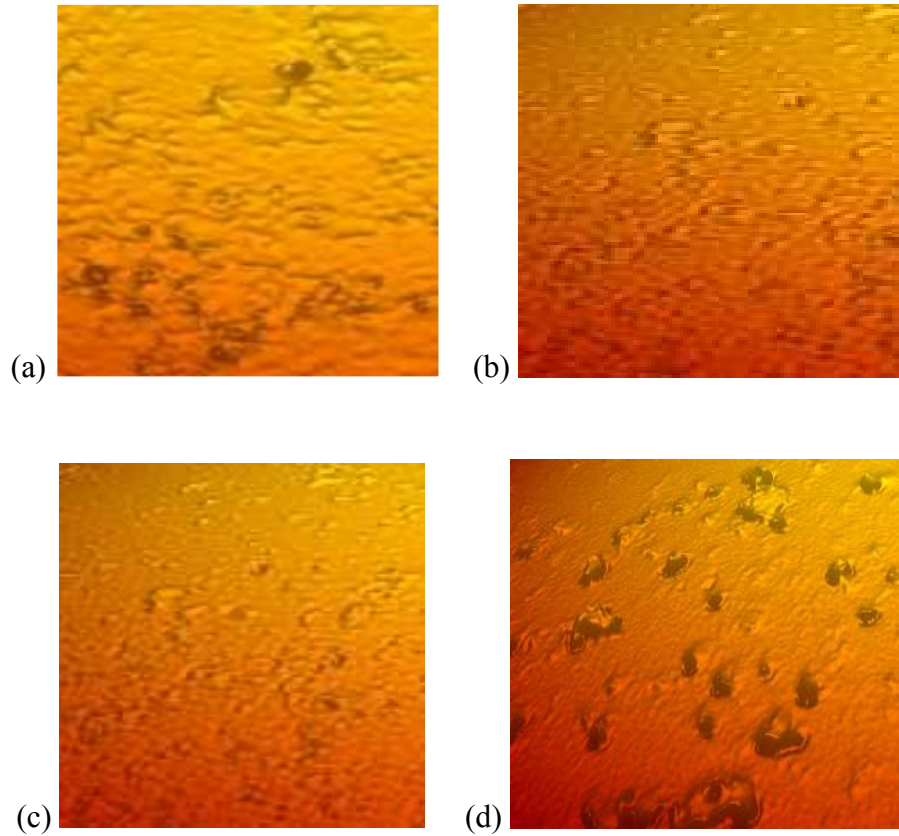
Figure 16. Selected surface topography images of 2.1 mm etched spherical particle at etching times of: (a) 5 min, (b) 10 min, (c) 15 min, and (d) 20 min.

The same profilometer is used to estimate the roughness of the hopper walls. Table 2 shows the highest peak, the lowest peak, and the root mean square of the roughness for each hopper type. The visual topographic images of the hopper wall surfaces are presented in Fig. 17. Both Table 2 and Fig. 17 demonstrate that the surface of the 3D-printed hopper is significantly rougher than the glass hopper.

46

Table 2. Hopper Wall Roughness Values Obtained From the Optical Profilometer.

	3D	Glass
Highest Peak, R_p (µm)	19.12	0.16
Lowest Peak, R_v (µm)	1.34	0.006
Root Mean Square, R_q (µm)	1.73	0.005

(a)

(b)
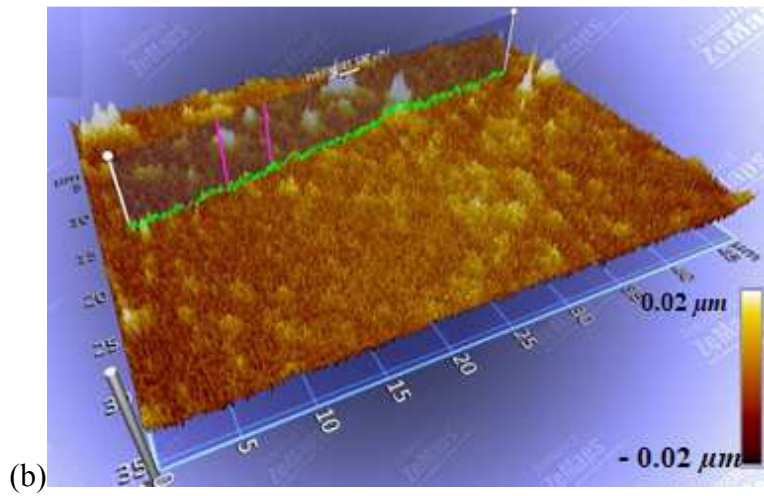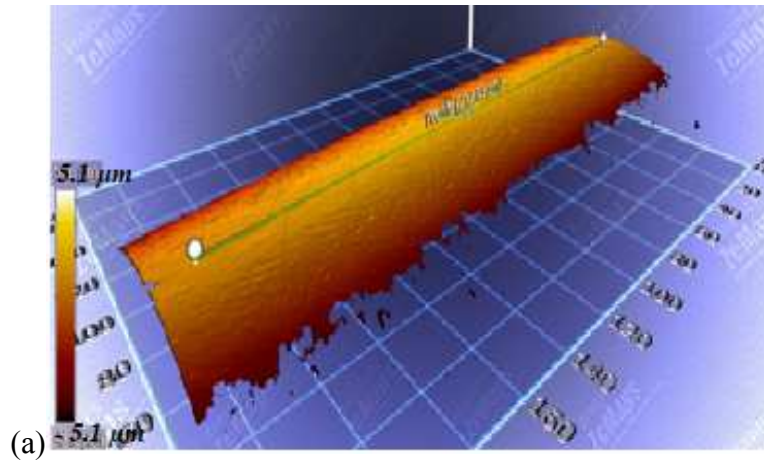
Figure 17. Visual surface topography images of the hopper wall for the: (a) 3D-printed hopper and (b) glass hopper.

To study the effect of particle roughness, 2 to 2.25 mm diameter (2.1 mean diameter) silica particles of different roughness levels (see Fig. 15) are used. The 3D-printed hopper is filled with 500 g of sample, and the discharge rate through the hopper is recorded. The discharge rate of the hopper is calculated as the ratio of the mass of particles discharged through the hopper to the time taken for the discharge. Fig. 18 shows the effect of particle roughness on the hopper discharge rate. It can be seen that the discharge rate decreases with increasing particle roughness. An increase in roughness from 0.25 to 5.02 μm decreased the discharge rate from 11.4 to 2 g/s.

At lower roughness values, the particle-particle (P-P) friction is low, resulting in low normal stress. In the case of low P-P friction, the particles flow easily and quickly. Similar results were found by Suiker & Fleck (2004) and Anand et al. (2008) in their studies of particle friction and fill height. They found that in the case of low friction solids, the discharge rate was a function of fill height, and a hypothetical frictionless solid behaved like a fluid, showing a fill height dependency of $H^{0.5}$. As roughness increased, an increase in particle friction was observed, and thereby the discharge rate was found to decrease. A possible reason for this behavior is that increased friction increases the normal stress on each particle, and introduces choking of the flow due to the accumulation of the particles. Similar results were observed by Ahn et al. (2008) in their experimental work, where they found the presence of an unstable and transitional regime, characterized by a decrease in mass discharge rate with increasing normal stress.

For the 2.1 mm particles studied in this work, it is observed that the discharge rate is proportional to $(R_q)^{-0.59}$. However, the relation between discharge and particle roughness for other sized particles is not considered in the current work.
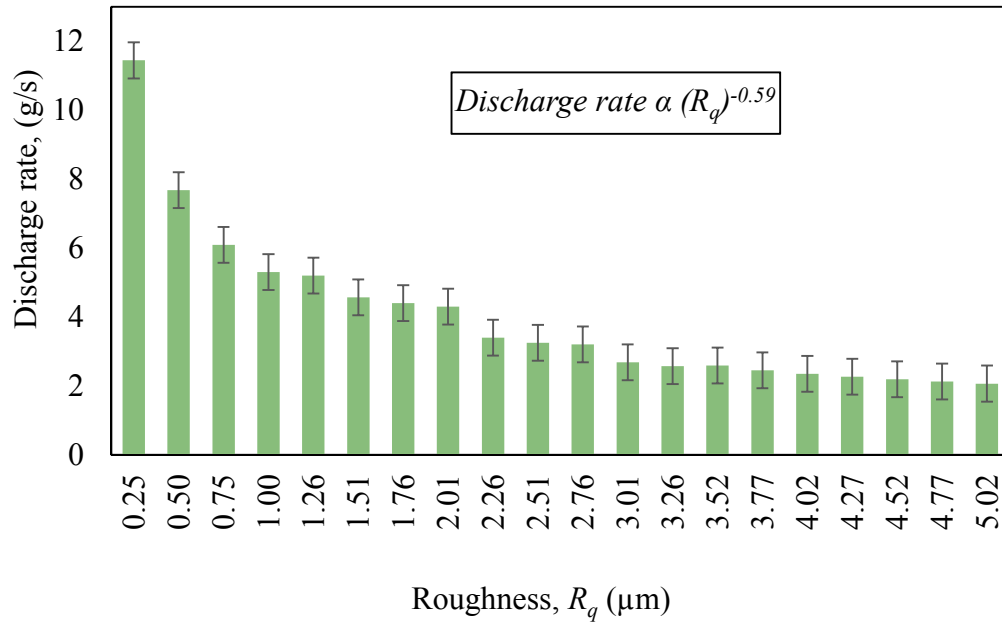
Figure 18. Discharge rate through 3D printed hopper of 2.1 mm particles for different roughness levels.

To study the effect of wall roughness, the discharge rates of all eleven samples shown in Table 1 are collected. Fig. 19 shows the effect of wall roughness on the hopper discharge rate for both the 3D-printed and the glass hopper. It is observed that as the wall roughness increases (from the glass to the 3D-printed hopper), the discharge rate increases. However, quantitatively, the percentage change in discharge rate varies only 200 % and 100 %, with a 34,500 % increase in wall roughness for the glass hopper and

the 3D-printed hopper, respectively. Thus, wall roughness has a negligible influence on the discharge rate. These results suggest that particle roughness plays a much more significant role than wall roughness, and is expected to influence the flow regime and discharge rate. From Fig. 19, it can also be seen that the discharge rate increases with increasing particle size for particles above 1 mm size. For particle sizes below 1 mm there is no trend observed. However, the percentage change in discharge rate varies only 200 % and 100 % with a 2200 % increase in mean particle diameter
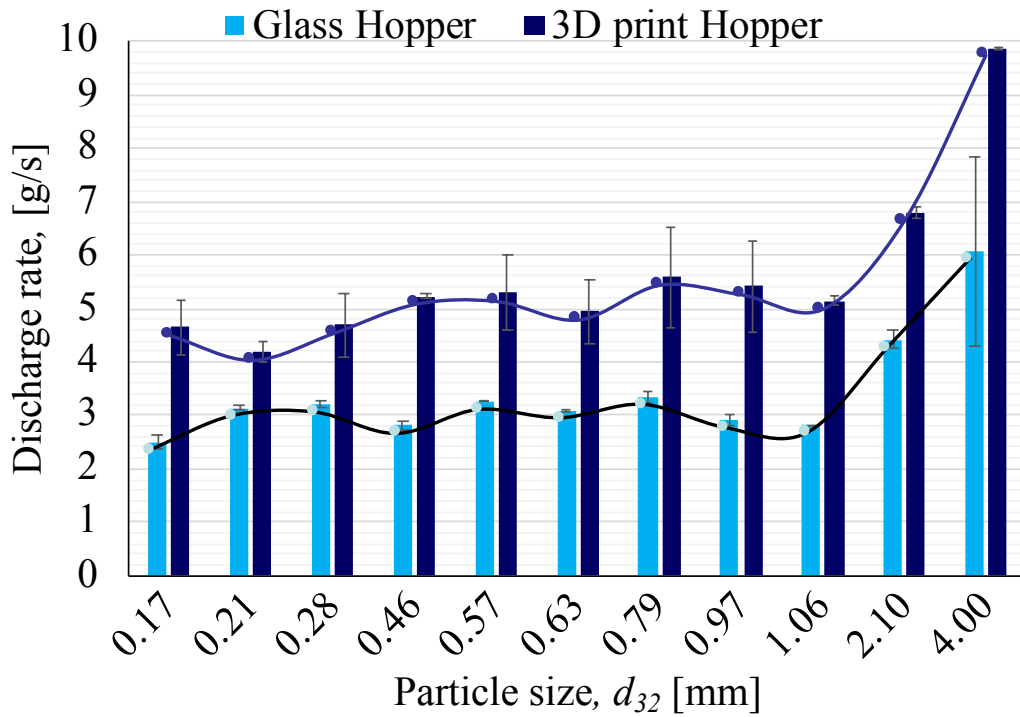
Figure 19. Discharge rate of particles through both glass and 3D-printed

hoppers.

3.6 Conclusions

This work uses experiments to study the effects of both wall and particle roughnesses on the discharge rate of silica beads through a cylindrical hopper. Varying levels of particle roughness are achieved by base etching using an NaOH solution for different amounts of time. It is found that particle roughness plays a significant role in determining the discharge rate of hoppers. An increase in roughness resulted in a decrease of discharge rate, which could be a result of clogging of the particles due to increased particle friction. Furthermore, two hoppers are built, using 3D printing and glass blowing, to vary wall roughness. It is found that wall roughness does not have a significant effect on the discharge rate. Also, it is observed that particle size has a very minimal influence on the discharge rate, which is consistent with previous findings. The results indicate that hopper discharge rate can be increased by decreasing particle roughness. An extended study must be done to verify if the correlation of *Discharge rate* α *$(R_q)^{-0.59}$* observed with 2.1 mm diameter particles is applicable to all size ranges.

3.7 Acknowledgements

4 WALL TO PARTICLE BED CONTACT CONDUCTION HEAT TRANSFER IN A ROTARY DRUM USING DEM

4.1 Abstract

Contact conduction heat transfer behavior in a rotary drum using the discrete element method (DEM) based simulation codes MFIX-DEM (open-source) and EDEM (commercial) is investigated. Simulations are performed to compare the performance of open-source and commercial code models with experimental data. This study also aims to investigate the effects of particle size distribution (PSD), rotation speed, and rolling friction on overall wall-bed heat transfer using the validated codes. It is found that the variability in the PSD with same mean, μ, and standard deviation, σ, resulted in different heat transfer coefficients. Monodispersed particle beds exhibit better heat transfer when compared to polydispersed beds because heat transfer is inhibited as the distribution broadens due to segregation. Rotation speed has minimal impact on conduction heat transfer. At lower values of rolling friction, particle circulation in the bed is enhanced and therefore better heat transfer is achieved.

4.2 Introduction

Granular materials undergo processing steps that include transportation, drying, and chemical or physical conversion. In several instances, these materials involve heat transfer during processing, and the particle heat transfer characteristics are complex due to a wide range of process parameters, the continuous moving bed, and the moving drum wall. Also, the measurement systems in rotary drums remain limited, so it is difficult to

extract the temperature of each particle continuously throughout experiments. However, recent developments have enabled scientific computing to significantly advance our understanding of the fundamental physics involved in such complex processes. Simulation can provide a means for solving the physics-based mathematical equations, to resolve the governing physics both spatially and temporally, and to optimize, design, and troubleshoot specific problems. In recent years, the discrete element method (DEM) has become an important means to study particle heat transfer (Zhu et al., 2008). It is a tool for simulating solids flow by solving Newton's equations of motion for individual particles as well as energy balances for each particle, thereby allowing the user to track the position and temperature of each particle.

Previous researchers have focused on developing DEM codes to solve complex problems and handle a diverse range of spatial/temporal scales involved in multiphase flow simulations. Work has been carried out to reduce the time-to-solution through performance improvements, and uncertainty quantification analysis is done to improve the credibility of the prediction capability. However, with multiple DEM codes available, computational experts find it challenging to adopt the most suitable DEM code to model their processes. Therefore, it is worth comparing different codes to check their adaptability. In this work, we aim to validate and compare the DEM heat transfer model developed in an open-source code (MFIX-DEM) and a commercial code (EDEM) using the experiment performed by Chaudhuri et al. (2010).

Many commercial and open-source DEM codes that can resolve the solid phase heat transfer are now available. Researchers have focused on developing and improving

these models, to enchance their physical modeling capabilities. Most recently, we have presented our developments for enhancing MFIX-DEM (Chen et al., 2017), a suite of open-source software for multiphase flow simulations including both the two-fluid model (TFM) and the coupled CFD-DEM model, developed and maintained by the National Energy Technology Laboratory (NETL) of the U.S. Department of Energy (Syamlal, 1998). MFIX-DEM has codes implemented for solving all three modes of heat transfer. However, until the 2016-1 release version, MFIX-DEM was incapable of simulating polydisperse systems (heterogeneity of sizes), which created problems when modeling industrial applications. Chen et al. (2017), presents our recent work on enhancing MFIX-DEM's physical modeling capability for handling particle-size polydispersity. We have modified the data structures and created new subroutines to separately handle geometrical and physical parameters of the solid particles. This approach has enabled MFIX-DEM to easily handle an arbitrary number of solid (particle) phases, where the particles in each phase are allowed to possess a distinct arbitrary particle-size distribution.

Researchers have extensively adopted DEM for simulation of bulk materials, and one significant aspect in simulations is the determination of material and contact parameters. Repeatedly, these parameters have to be calibrated because they are difficult to measure or do not have a physical analogue. One such parameter is particle rolling friction. Rolling friction is an important macroscopic DEM parameter to indicate the granular behavior, and is of particular interest as it simplifies particle shape modeling (Frankowski and Morgeneyer, 2013). Work has been done to study the effect of coupled sliding-rolling friction to develop more shape models, but the individual effect of rolling

friction has not been investigated in complex dynamic processes (Syed et al., 2017a; Wensrich and Katterfeld, 2012). Therefore, this work also investigates the effect of rolling friction on heat transfer in a rotary drum.

4.3 Rotary Drums

Rotary drums are the most commonly used process equipment in the chemical, metallurgical, pharmaceutical, and catalyst industries to handle bulk materials (Xu et al., 1984). They are used to operate under high temperature, for example, calcination of petroleum coke [1373 K] (Martins et al., 2001), lime burning [1473 K] (Georgallis et al., 2002), thermal treatment of waste material [1173–1473 K] (Rovaglio et al., 1998), gasification of waste tires or wood to obtain activated carbon [1573 K] (Ortiz et al., 2005), calcination of aluminum oxide and coke [1573 K] (Bui et al., 1995; Kawecki et al., 1974), and burning of cement clinker [2273 K] (Peray and Waddell, 1986). As these processes are related to high energy demand, optimizing them can save energy as well as material costs, leading to improved processes and products.

The heat transfer in an externally (indirectly) heated rotary drum is influenced by particle and process parameters such as specific heat capacity, particle size, particle size distribution (PSD), particle shape, particle density, thermal conductivity, rotational speed, fill level, and equipment design parameters (diameter, length, and inclination angle). Table 3 presents a few of the most recent studies that investigated heat transfer in rotary drums using DEM simulations. A majority of the findings suggest that faster heating of the particle bed is achieved at higher thermal conductivity, lower heat capacity, higher

rotation speed, lower fill level, and smaller particle size. It was also found that particle cohesion does not affect heat transfer, and baffles promote heat transfer. Although several variables have been investigated, little work has been done on understanding the effects of PSD on heat transfer. An understanding of the particle hydrodynamics is a pre-requisite to study heat transfer (H. Liu et al., 2016), and previous studies showed that PSD influences the positioning of particles inside the system due to the velocity differences between different sized particles (Ding et al., 2002); therefore, a clear understanding of PSD is crucial. Past researchers have studied heat transfer in rotary drums using experiments with monodispersed, bi-dispersed, and polydispersed beds (Nafsun et al., 2018). However, less work has been done on understanding the effects of polydisperse PSDs using DEM. With the DEM capabilities available now, it is possible to model complex distributions that are relevant to industry.

Table 3. Literature Studies Employing Dem to Investigate Heat Transfer in Rotary Drums. (Tc: Thermal Conductivity, Hc: Heat Capacity, C: Cohesion, Rs: Rotation Speed, Fl: Fill Level, B: Baffles, Ps: Particle Size, Psd: Particle Size Distribution, Pd: Particle

Literature	Variables Investigated	Major Findings
Chaudhuri et al., 2006	TC, HC, RS, FL	• Faster heating is achieved for materials with higher TC and lower HC, and for lower FL. • C does not affect heat transfer rates. • Increasing RS decreases the heat transfer rate.
Kwapinska et al., 2008	N/A	• Studied heat transfer controlled by a contact resistance at the wall. • Investigated heat transfer to agitated beds with significant bed-side resistance to the stagnant bed.

		• Achieved calibration between DEM and the penetration model.
Chaudhuri et al., 2010	RS, TC, B, shape of B	• RS has a minimal impact on the heat transfer. • Higher TC promotes faster heat transfer. • B or flights enhance heat transfer. • L-shaped B are more effective than square B.
Nguyen et al., 2015	TC, RS, HC, FL, PS	• Observed faster heating with higher TC, higher RS, lower HC, lower FL, and smaller PS.
Emady et al., 2016	RS, TC	• Sensitivity of heat transfer to RS increases with increasing particle TC. • Modeled three heating time scales from wall to bed.
Yohannes et al., 2016	FL, RS	• Introduced dimensionless equations for scaling of heat transfer. • Defined equations that can predict average temperature and distribution of particles' temperature under varying conditions.
Mesnier et al., 2018	PSD, PD	• Thermal segregation is enhanced by mechanical segregation and is stronger for bi-dispersed beds than for monodispersed beds. • Bi-density bed exhibits stronger thermal segregation than the bi-size bed.
Bongo Njeng et al., 2018	RS, FL, B	• At constant FL, heat transfer increases with increasing RS. • Convection has little or no effect on the wall-to-solid heat transfer coefficient. • B or lifters enhance heat transfer.
Zhang et al., 2019	RS, FL	• Higher RS and lower FL are beneficial for both mixing and heat transfer.
Tsotsas, 2019	TC	• Proposed an analytical equation to calculate the particle-particle heat transfer coefficient (α_{pp}) from the effective thermal conductivity. • α_{pp} is directly proportional to TC.
Yazdani and Hashemabadi, 2019	PS, RS, FL	• Large particles tend to move towards the outer layer of the bed. • An increase in the PS ratio slowed the bed heat-up. • A higher RS and lower FL resulted in faster heating.

4.4   Objectives

This study aims to compare the DEM heat transfer models developed in an open-source code (MFIX-DEM) and a commercial code (EDEM). We investigate the effect of PSD and its variability on heat transfer in an indirectly heated rotary drum using our MFIX-DEM polydispersity implementation, presented in Chen et al. (2017). We also investigate the effect of rolling friction on heat transfer using EDEM.

4.5   Heat Transfer Modeling

In an externally heated rotary kiln, the high-temperature inner wall serves as a heating source and heats the solid particle bed to a predetermined temperature. Wall-particle heat conduction and particle-particle heat conduction are the main heat transfer methods here. There are also some auxiliary heat transfer modes, such as heat convection through the interstitial gas and radiative heat transfer between an exposed wall and the top surface layer of particles; however, the convection and radiation mechanisms are neglected in this work based on the following assumptions:

1. According to Batchelor & O'Brien (1977), as long as $(k_s a)/(k_f r)) \gg 1$, the contact conduction through particle-particle and particle-wall dominates. Here, a is the contact radius, r is the particle radius of curvature, k_f denotes the fluid interstitial medium conductivity, and k_s is the thermal conductivity of the solid granular material. Most recently, Njeng et al. (2018) proved that at low or no axial flow of gas through a drum operating below 573 K, convection has no or trivial effect on the wall to solid heat transfer. In the current study, $k_s \gg k_f$; therefore, interstitial

gas is neglected, and no gas phase equations are solved. Also, this condition is identically true in a vacuum.

2. Heat transfer from the wall to the solid bed by radiation is neglected due to the low-temperature environment (<700 K) inside the drum (Thammavong et al., 2011).

3. Constant physical properties: Particle properties such as heat capacity, thermal conductivity, and Young's modulus are considered to be constant throughout the process.

4. Isothermal particles: The contribution of heat transfer inside a particle is significantly reduced when the Biot number is less than 0.1, according to the lumped capacity approach (Yang et al., 2015). The Biot number for the alumina particles considered in this study is 0.02.

5. Boundary wall temperatures remain constant.

Applying all of these assumptions, only particle-particle and particle-wall conduction are considered, and the resulting thermal energy on a single isothermal particle is reduced to:

$$m_{p,i} C_{p,i} \frac{d}{dt} \left(T_{p,i} \right) = q_{i,j}^{pp} + q_i^{Pw} \tag{1}$$

where $m_{p,i}$ is the mass of particle i; $C_{p,i}$ is the specific heat of particle i; $T_{p,i}$ is the temperature of particle i; $q_{i,j}^{pp}$ is the rate of heat transfer between particle i and particle j; and q_i^{pw} is the rate of heat transfer between particle i and the wall. The particle-wall and

particle-particle conduction can be given as (Batchelor and O'Brien, 1977; Vargas and

McCarthy, 2001):

$$q_i^{pw} = h_{pw,i}(T_w - T_{p,i}) = \frac{4k_{p,i}k_w}{k_{p,i}+k_w}R_{Cw}(T_w - T_{p,i}) \qquad (2)$$

$$q_{i,j}^{pp} = h_{pp,i,j}(T_{p,j} - T_{p,i}) = \frac{4k_{p,i}k_{p,j}}{k_{p,i}+k_{p,j}}R_{Cp}(T_{p,j} - T_{p,i}) \qquad (3)$$

where $h_{pw,i}$ is the particle-wall conduction heat transfer coefficient for particle i

and the wall; T_w is the wall temperature; $T_{p,i}$ is the temperature of particle i; $k_{p,i}$ and $k_{p,j}$

are the thermal conductivities of particles i and j, respectively; k_w is the thermal

conductivity of the wall; $h_{pp,i,j}$ is the particle-particle conduction heat transfer coefficient

between particles i and j; and R_{cp} and R_{cw} are the radii of contact resulting from the

geometric overlap of the particle-particle and particle-wall upon collision, respectively.

In a rotary drum system, the heat transfer from the wall to the granular bed at any

given moment can be calculated from the heat balance equation as (Chaudhuri et al.,

2010; Wes et al., 1976):

$$M_s C_{ps} \frac{d}{dt}(T_s) = \alpha e_s A_s L(T_w - T_s) \qquad (4)$$

where M_s is the total mass of the solid material; C_{ps} is the specific heat of the solid

material; T_s is the average temperature of the solid material; α is the overall heat transfer

coefficient; e_s is the fraction of the wall touched by the solid material; A_s is the drum

circumference; L is the length of the drum; and T_w is the drum wall temperature. The

exact solution to Eq. (4) is given by the following expression:

$$ln\left(\frac{T_w - T_s}{T_w - T_s{}^o}\right) = -\frac{\alpha e_s A_s L}{M_s C_{ps}} t = \frac{-t}{\tau} \tag{5}$$

where $T_s{}^o$ is the initial temperature of the solid material, t is the time, and τ is the

thermal time constant. The thermal time constant, τ, is related to the time taken by the

complete solid bed to reach the final wall temperature. τ can be derived by plotting the

values of the natural logarithm of the ratio of $(T_w - T_s)$ to $(T_w - T_s{}^o)$ versus elapsed time and

calculating the negative inverse of the slope of the best-fit straight line drawn.

4.5.1   MFIX-DEM

The time integration method for the discrete solids phase momentum equation in

MFIX-DEM is based on the Adams-Bashforth method (Dietiker, 2013). The same

method is used to advance the solution of the particle internal energy equation. Therefore,

the temperature of a particle is calculated as (Musser, 2011):

$$T_{p,i}(t + \Delta t_s) = T_{p,i}(t) + \frac{\Delta t_s}{m_{p,i}(t)C_{p,i}(t)}\left(q_i^{pp}(t) + q_i^{pw}(t)\right) \tag{6}$$

where Δt_s is the step size for the numerical integration. At every time step, the

DEM model calculates the particles' contact forces from the contact properties and the

particles' heat fluxes from the thermal properties. It then calulates the sum of all forces

acting on the particles and heat fluxes on the particles. In the next step, it updates the

particle position, velocity and temperature.

The evolution of the temperature field of the granular flowing system for each time step is calculated as the average temperature, T_s (used in Eq. (4)), of all of the particles in the system:

$$T_s = \frac{1}{N_p} \sum_j^{N_p} T_{p,i} \tag{7}$$

where N_p is the total number of particles in a simulation and $T_{p,i}$ is the temperature of the indexed particle.

4.5.2   EDEM

Previously, Emady et al. (2016) used an in-house EDEM API model which accounts for the heat transfer between the drum walls and the particles. The same model is used in the present work. The temperature evolution of an individual particle is as follows (Emady et al., 2016):

$$\frac{dT_i}{dt} = \frac{\sum Q_{ij}}{\rho_p V_p C_p} \tag{8}$$

$$Q_{ij} = H_{c,ij}(T_j - T_i) \tag{9}$$

$$H_{c,ij} = 2k_p \left[\frac{3 F_N r^*}{4 E^*}\right]^{1/3} \tag{10}$$

where T_i and T_j are the temperatures of the particles i and j, respectively; Q_{ij} is the heat transferred from particle j to particle i; $H_{c,ij}$ is the inter-particle conductance; ρ_p, C_p, V_p, k_p, and E^* are the density, specific heat capacity, volume, thermal conductivity of the

particle, and effective elastic modulus, respectively; F_N is the normal component of the

contact force; and $r*$ is the effective radius of the contact area.

4.5.3   Simulation conditions

Particles are generated inside the drum and allowed to fall under gravity. All of

the particles are initially assigned a temperature of 298 K. Once the particles inside the

drum reach mechanical equilibrium, the wall is instantaneously heated and maintained at

the desired wall temperature, and the drum is rotated. The heated wall of the drum has the

no-slip condition, and the front and back walls of the domain are free-slip adiabatic

boundaries. The geometry is held fixed in time, and the rotation of the drum is generated

by modifying the gravity vector. As the drum is rotated, the particles move due to friction

between the wall and particles. At the same time, heat is transferred from the higher

temperature wall to the lower temperature particles, and from the higher temperature

particles to the lower temperature particles.

4.6   Results and discussion

4.6.1   Thermal time constant

Both MFIX-DEM and EDEM are used to simulate the setup described in Section

3, and the parameters given in Table 4 are employed here. Fig. 20 shows the temperature

profile of the alumina bed at different time intervals. A similar heating profile is observed

in both the simualitons, where the near-wall particles heat up due to particle-wall contact,

and these particles are transported to the freeboard as the drum rotates. The heat

penetrates the solid bed to include more heated particles with subsequent rotations,

thereby increasing the thermal boundary. Moreover, heated particles from near the wall transmit heat to surrounding particles as they move toward the freeboard region. This is seen after 10 s of simulation (see Fig.20b and 20e), where a thick layer of particles is heated along the boundaries of the solid bed. As time progresses towards 20 s (see Fig. 20c and 20f), more particles are heated, forming a cool inner core and a warmer outer layer in the solid bed. However, a section of particles in the lower right side has a comparatively higher temperature than the surrounding particles, thereby creating a stagnant zone. According to Mellmann (2001), this behavior is characteristic of the cascading regime, which is expected at its Froude number of 3.4×10^{-2}. In their simulations, Chaudhuri et al., (2010) also observed the same heating profile in the cascading regime, with an increasingly thick warmer outer layer and cooler inner core.
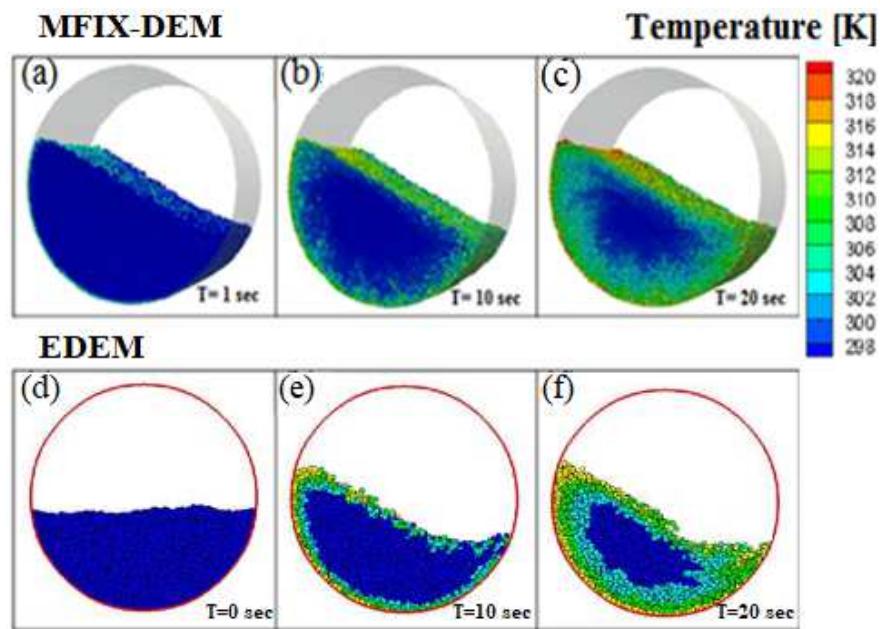
Figure 20. The temperature distribution of alumina obtained from MFIX-DEM and EDEM simulations.

64

Table 4. Simulation Parameters Used for Monodispersed Alumina Particles.

	Parameters	Value
Global	Coefficient of restitution	
	particle-particle	0.8
	particle-wall	0.5
	Friction coefficient	
	particle-particle	0.1
	particle-wall	0.1
	Normal stiffness coefficient	
	particle-particle	6000 N/m
	particle-wall	6000 N/m
	DEM time step	1.0×10^{-6} s
Particles	Material	Alumina
	Density, ρ	3900 kg/m^3
	Poisson's ratio	0.3
	Shear modulus	70.0×10^9 Pa
	Heat capacity, C_p	875 J/kgK
	Thermal conductivity, k	36 W/mK
	Initial temperature, T_s^o	298 K
	Total number of particles	20,000
	Particle diameter	0.2 cm
Drum	Temperature, T_w	373 K
	Diameter	15.24 cm
	Poisson's ratio	0.3
	Shear modulus	70.0×10^9 Pa
	Length	7.62 cm
	Fill level	50 %
	Rotation speed, ω	20 rpm

Fig. 21 shows the evolution of the scaled average bed temperature for MFIX-DEM, EDEM and experimental data (Chaudhuri et al., 2010). The simulations and experiment show the same trend in the log mean temperature. To better assess the accuracy of results, the thermal time constant, τ, is calculated using Eq. (5). The value of τ is 175.4 s for the experiment, 185.2 s for the MFIX-DEM simulation, and 158.7 s for EDEM simulation. Even though there is a discrepancy in τ, in general, there is a good agreement between the simulaion and experimental results. The results suggest that DEM simulations are a realiable means to model particulate processes.

There are a few possible reasons for the discrepancy observed between the simulation and experiments. A sudden elevation in the temperature is observed at 6 s in the experiments, which was not explained by Chaudhuri et al., (2010). Due to the lack of confidence interval data in the experimental results reported, it is difficult to determine the root cause for this discrepancy. For calculating the average temperature (T_s) in experiments, it is stated that the drum is stopped at 30 s intervals, then the thermocouples are inserted into the ten ports arranged radially along one of the side walls, and T_s is estimated as the mean of the readings of the ten thermocouples. When the drum is stopped for thermal measurements, it is likely that the temperature recorded by each thermocouple is an average measure of the interstitial fluid and particle temperatures. In such cases, the average temperature of the fluid-particle might read a higher value than the actual particle temperature and result in a subsequent rise in the recorded temperature. Also, when the drum is stopped for recording the temperatures, the contact time between

the solid bed and the wall increases, and simultaneously heat can be transferred to the particles, which might elevate the solid bed temperature.
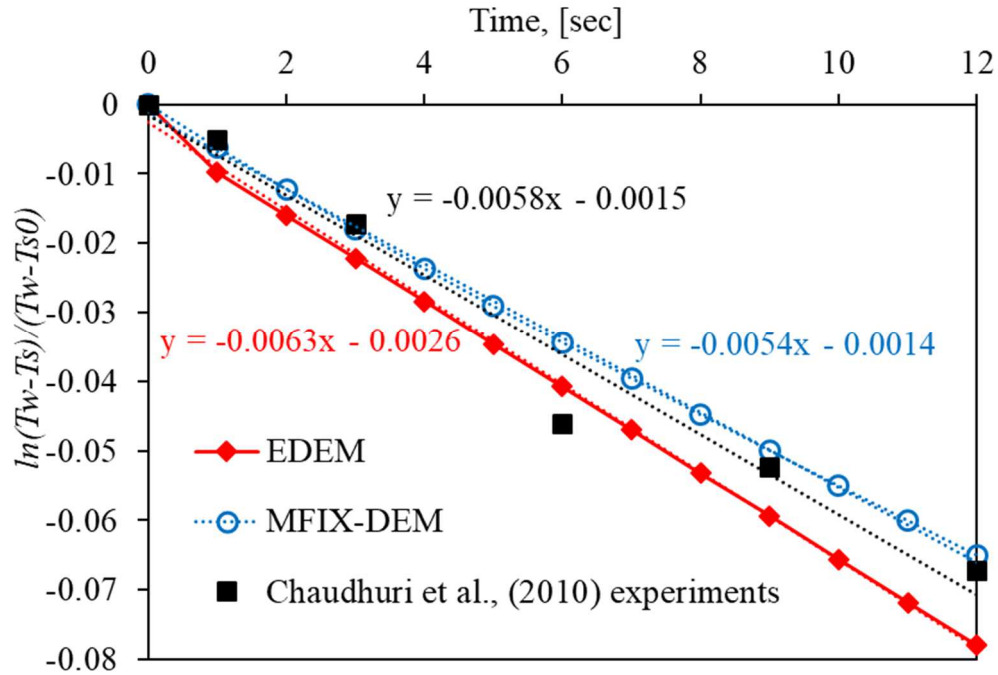
Figure 21. Logarithmic variation of scaled temperature difference with time for the DEM simulations and experiments (Chaudhuri et al., 2010).

Another reason for the discrepancy can be due to particle size variations. Chaudhuri et al., (2010) reported that the solid phase is monodispersed with 0.2 cm diameter alumina particles, and based on this, the current simulations are performed with single-phase monodispersed particles. But in reality, the experimental particles are most likely not perfectly monodispersed. Huang et al. (2013) showed that the rolling friction coefficient significantly affected the internal friction angle of dense granular processes. Therefore, it is important to investigate its effect on the hydrodynamic and thermal

behavior of the particles in a rotary drum. Further investigation of these two model parameters, particle size distribution (PSD) and rolling friction, are presented in Section 5.7.2.

4.6.2   Effect of model parameters

A parametric study is conducted by varying the particle size distribution (PSD) and rolling friction to better understand the effects of these model parameters. A steel drum of 15 cm diameter and 2 cm axial length filled with 0.11 kg of polydispersed alumina particles with 0.4 cm mean diameter and 0.33 relative standard deviation is used. All of the particles are initially given a temperature of 298 K, and the drum wall is maintained at a temperature of 578 K. A high thermal conductivity of 3000 W/mK is used to achieve a low thermal time constant in order to decrease the time-to-solution. All of the drum operating conditions and the simulation parameters are adopted from the DEM simulations performed by Emady et al. (2016) (see Table 5). The work published by Emady et al. (2016) used polydispersed alumina particles as the solid phase for studying the contact conduction heat transfer in a rotary drum. Since one of our parameters of interest is particle size distribution (PSD), we have chosen to adopt the model parameters from this work.

Table 5. Simulation Parameters Used for Polydispersed Alumina Particles.

	Variable	Value
Global	Coefficient of restitution	
	particle-particle	0.8
	particle-wall	0.8
	Friction coefficient	
	particle-particle	0.2
	particle-wall	0.2
	Normal stiffness coefficient	
	particle-particle	100 N/m
	particle-wall	100 N/m
	DEM time step	1.0×10^{-6} s
Particles	Material	Alumina
	Density, ρ	3890 kg/m^3
	Poisson's ratio	0.25
	Shear modulus	1.0×10^6 Pa
	Heat capacity, C_p	880 J/kgK
	Thermal conductivity, k	3000 W/mK
	Initial temperature, T_s^o	298 K
	Total particle mass	0.11 kg
	Particle radius, μ	0.2 cm
	Particle size distribution, σ/μ	Normal, 0.33
Drum	Material	Steel
	Poisson's ratio	0.25
	Shear modulus	7.93×10^7 Pa
	Wall temperature, T_w	578 K
	Diameter	15 cm
	Length	2 cm
	Average fill level	13 %
	Rotation speed, ω	5, 10, 20, 30 rpm

4.6.3 Effect of particle size distribution (PSD)

MFIX-DEM randomly generates particles using the user-defined mean size (μ), maximum size, minimum size, and standard deviation (σ). Three series of normal distributions (batch 1, batch 2, and batch 3) are generated using 0.4 cm as the mean, 0.46 cm as the maximum, 0.33 cm as the minimum, and 0.035 cm as the standard deviation of the diameter. The PSDs generated in the three series are shown in Fig. 22, with a total of 867 particles each. The particles are given the properties of alumina (see Table 5), and the simulations are conducted at rotation speeds of 5, 10, 20, and 30 rpm. Fig. 23 shows the effect of rotation speed, ω, on the overall heat transfer coefficient, α, for the three batches. It can be observed that rotation speed has no significant effect on the contact heat transfer, which is consistent with previous literature findings (Chaudhuri et al., 2010; Emady et al., 2016).
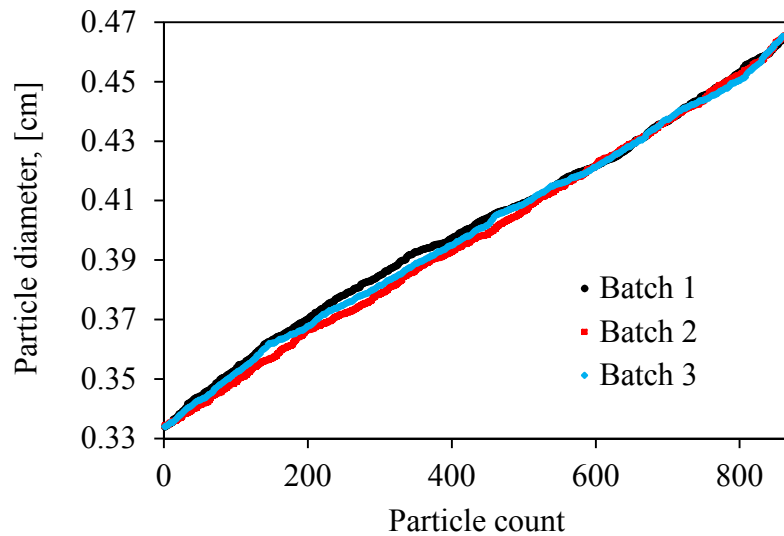
Figure 22. Particle size distributions with μ = 0.4 cm and σ = 0.035 cm.

70
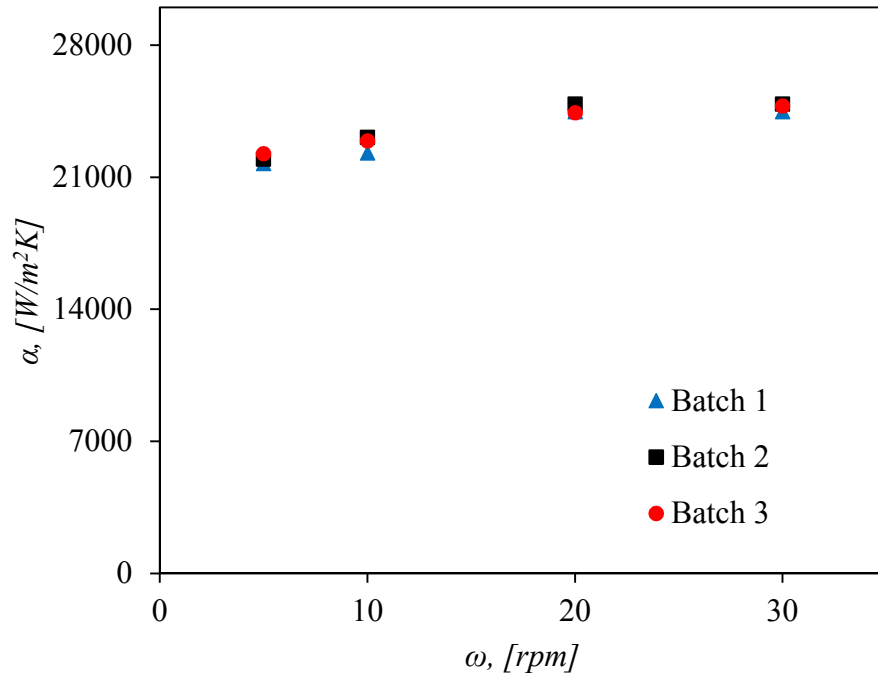
Figure 23. The sensitivity of the overall heat transfer coefficient to rotation speed for three PSDs with μ = 0.4 cm and σ = 0.035 cm.

For the different PSDs, the overall heat transfer coefficient, α, varied with a standard deviation of 267.1, 431.4, 247.9, and 213.9 W/m^2K at rotation speeds of 5, 10, 20, and 30 rpm, respectively, which contributes up to approximately 2 % of the observed values. Therefore, while performing validation studies using polydispersed particles, a certain percentage of discrepancy observed between the results might be caused by the failure to replicate the particle size distribution in the experiments. Hence, the discrepancy noted in Section 4.1 might have a certain percentage contributed by the

difference in PSD. Furthermore, additional simulations are performed to study the effect of distribution width.

Three simulations are performed using different types of distributions, namely, homogeneous, narrow, and broad. Table 6 and Fig. 24 show the particle size distributions obtained from MFIX-DEM for the three distributions. All three distributions have a mean diameter of 0.4 cm. The narrow and broad distributions have a size range from 0.34 to 0.47 cm and 0.21 to 0.6 cm, respectively (see Table 6). These values have been chosen to keep the difference in PSD minimal and observe its effect. An overall heat transfer coefficient of 52, 50, and 48 kW/m^{2}K is found for the homogeneous, narrow, and broad distributions, respectively (see Table 6). A percentage difference of 4 % is observed between the homogeneous and narrow, and 9 % between the homogeneous and broad distributions. The case with a broad distribution has a lower heat transfer coefficient, and the homogeneous distribution case has a higher heat transfer coefficient. Since polydispersed particles exhibit segregation, the orientation of the particles inside the drum changes and the heat profile is different from that of the homogenous PSD. For narrow and broad distributions, which exhibit segregation, it can be seen that less particles are in contact with the drum wall compared to the homogeneous distribution case (see Fig. 24). This decreases the area of contact between the particle bed and the drum wall, which in turn decreases the heat transfer and results in a lower heat transfer coefficient. Therefore, the conduction heat transfer decreases as the PSD broadens.

Table 6. Particle Size Distribution Information Used for the Narrow,

Homogeneous, and Broad Distributions.

Type of distribution	Diameter, cm				Number of particles	α [kW/m²K]
	Minimum	Maximum	STDEV	Mean		
Homogeneous	-	-	-	0.4	396	52
Narrow	0.34	0.47	0.03	0.4	400	50
Broad	0.21	0.6	0.07	0.4	398	48
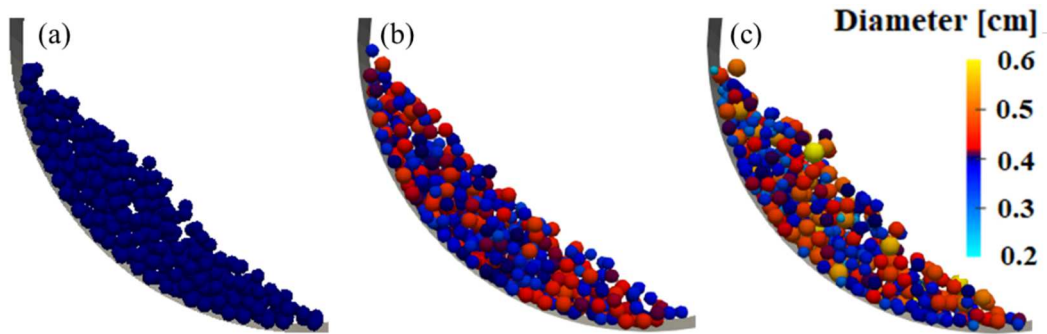
Figure 24. Particle size distributions obtained from MFIX-DEM simulations at t

= τ/2 for (a) homogeneous, (b) narrow, and (c) broad distributions.

4.6.4   Effect of rolling friction

Firstly, a no rolling friction case is simulated using MFIX-DEM for comparison

with the EDEM results. From Fig. 25, it can be seen that MFIX-DEM is able to predict a

similar trend to that obtained from EDEM, which is consistent with the results obtained

in Section 4.1. However, a slight discrepancy is observed, which may be a result of the

PSD, as discussed in Section 4.2.1. This suggests that MFIX-DEM can be used to solve

conduction heat transfer problems and is a viable alternative to the commercial codes. Also, since MFIX-DEM is an open-source code, it is transparent to the users and can be changed depending on the investigation purpose.

To understand the effect of rolling friction, simulations are performed using EDEM with rolling frictions of 0, 0.005. 0.01, and 0.1. These values are selected based on previous DEM rotary drum simulation works (Emady et al., 2016; Syed et al., 2017). To our knowledge, most researchers use a rolling friction value of less than 0.1 in their studies. Specifically, while studying spherical particles, where the surface is considered to be smooth, a lower value of rolling friction is expected to yield more realistic behavior.

Fig. 25 shows the effect of rolling friction on the overall heat transfer coefficient, α, at rotation speeds of 5, 10, 20, and 30 rpm. It can be seen that with increasing rolling friction, the heat transfer coefficient decreases. Comparing with the no rolling case at 5, 10, 20, and 30 rpm, a percentage change in the overall heat transfer coefficient of 2 %, 3 %, 1 %, and -4 % is observed for 0.005 rolling friction; 8 %, 5 %, 1 %, and -2 % is observed for 0.01 rolling friction; and 32 %, 42 %, 26 %, and 28 % is observed for 0.1 rolling friction, respectively. For instance, at 10 rpm, a higher heat transfer coefficient of 24 kW/m^{2}K is observed for the no rolling case, and a lower heat transfer coefficient of 16 kW/m^{2}K is observed at a rolling friction of 0.1. From 0 to 0.1 for 10 rpm, there is a 200 % change in rolling friction, and the change in heat transfer coefficient is 42 %. At lower values of rolling friction, particle circulation in the bed is enhanced, and therefore better heat transfer is achieved. A similar trend is observed at 5 rpm, with a 30 % change in heat

transfer coefficient from 0 to 0.1. Therefore, it can be concluded that rolling friction has a significant effect on the heat transfer between the drum walls and the process material.
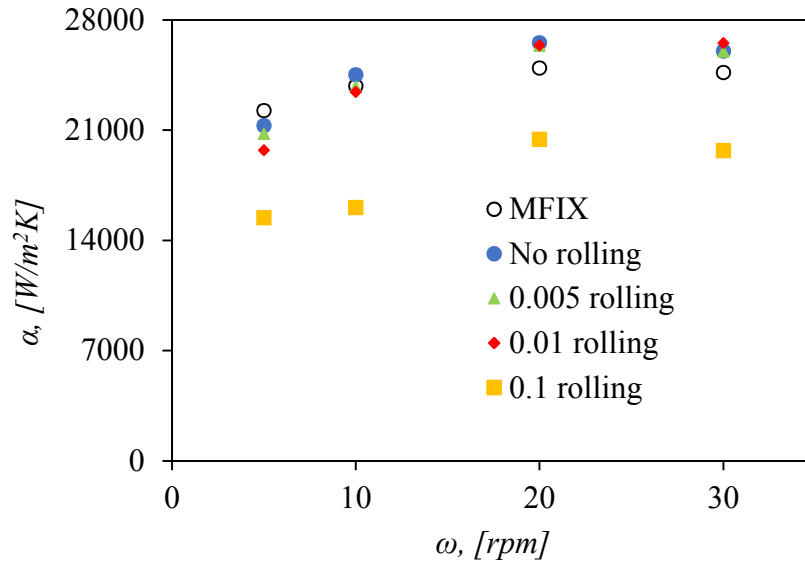
Figure 25. The sensitivity of the overall heat transfer coefficient to the rotation speed at rolling frictions of 0, 0.005, 0.01, and 0.1. All of the solid markers correspond to EDEM simulations.

4.7   Summary and Conclusions

In this study, the contact conduction heat transfer between the wall of a rotary drum and its internal solid particles was investigated. For a bed of monodispersed alumina particles, the conduction model was compared with the experiments published by Chaudhuri et al., (2010). A good agreement in the thermal time constant between the DEM simulations and experimental literature results was observed. Several potential sources for the observed discrepancy were discussed. Among these, to better understand

the role of model parameters, we studied the effects of particle size distribution (PSD) and rolling friction. Three different distributions with the same mean (0.4 cm) and standard deviation (0.035 cm) were generated by MFIX-DEM to study the effect of PSD. It was found that the three size distributions contributed up to approximately 2 % deviation in the observed heat transfer coefficient. Another study to determine the effect of distribution pattern was done using three distributions of the same mean (0.4 cm), but different standard deviations (0, 0.03, and 0.07 cm for homogeneous, narrow, and broad distributions, respectively). It was found that monodispersed particle beds exhibit better heat transfer when compared to polydispersed beds. With a narrow distribution, a better heat transfer rate was achieved than with a broad distribution, as the particles behave more similarly to a homogeneous bed. EDEM simulations were performed at rolling frictions of 0, 0.005, 0.01, and 0.1. It was seen that at lower values of rolling friction, particle circulation in the bed was enhanced and therefore better heat transfer was achieved.

The findings show that it is important to perform validation of computational models against experimental data, in which uncertainty has been assessed and documented through adequate metrics such as confidence intervals. Lack of such assessment can adversely affect the validation exercise. The current study suggests that the particle size distribution, the distribution pattern, and the rolling friction of the particles affect the solid bed heat transfer coefficient. These parameters play an important role in the hydrodynamics of the solid bed in a rotary drum, which in turn affect the conduction heat transfer. Additional simulations were performed to compare MFIX-DEM

76

with EDEM. A good agreement in the trend between heat transfer coefficient versus rotation speed was observed. The findings suggest that DEM simulations have made significant advances, and they are a reliable means to design realistic models. Also, the open source MFIX-DEM code can be a viable alternative to the commercial codes for solving conduction heat transfer problems, thereby eliminating license costs, especially in parallel calculations by multicore workstations or supercomputers with GPU.

In simulations, the drum walls were maintained at a constant temperature and were assumed to be isothermal, but practically the aluminum drum and the side walls are not isothermal, and heat loss may be observed. Although the computational model can be revised to characterize this effect by adding an appropriate heat loss term, it was not considered for the scope of the current work. The conduction heat transfer model was investigated using a scaled-down version of an industrial-sized rotary drum. Scaled-down geometries are usually used in simulation studies to reduce computational time. The effect of scale-up from lab-scale to industrial-scale drums might adversely affect the prediction credibility of the computational model. Therefore, in the future, we plan to perform similar studies to understand the effect of scale-up, and better assess the prediction credibility of the conduction heat transfer model in MFIX-DEM across multiple scales. Also, as the model was validated using only a lab-scale drum, it would be interesting to investigate the particle conduction in other processes, such as fluid beds, flow through pipes, and drying on conveyors. Hence, it is recommended that the model is validated for complex particle systems with different materials and process equipment.

The work considers a stagnant fluid phase. Hence, further work is needed to verify and validate the conduction model with fluid phase interactions. It is known that the gas between particles can affect heat transfer (Morris et al., 2015). Furthermore, the convection heat transfer models must be investigated, as most real processes involve multiphase systems with gas-solid interactions. Additionally, most industrial-scale calcination processes involve high temperatures much greater than 700 K, where radiation heat transfer is significant. Therefore, further work is also needed to investigate its contribution to the overall heat transfer.

4.8   Acknowledgments

5   CONDUCTION HEAT TRANSFER IN A ROTARY DRUM USING INFRARED THERMOGRAPHY

5.1   Abstract

A technique for studying heat transfer in a rotary drum is proposed using infrared (IR) thermography. An IR camera is used to record images to give instantaneous thermal data of particles inside a rotary drum. In this work, the calibration procedure and the methodology used to extract the bulk average temperatures of the particle bed and the drum wall from the IR camera is discussed. The technique provides insightful information on the flow regimes and heat transfer for varying drum fill levels and rotation rates. 3 mm silica beads inside a stainless-steel rotary drum are used at fill levels ranging from 10 – 25 % and rotation rates from 2 – 10 rpm. Higher rotation rates result in maximum steady state average bed temperatures, whereas fill level does not have a conclusive effect.

5.2   Introduction

Next to water, in many industries like foods, pharmaceuticals, ceramics, and semiconductors, granular materials are the second most manipulated substances (Richard et al., 2005). These materials undergo process steps that may include transportation, drying, heating and chemical or physical conversion. In several instances, these materials need to be heated or cooled during processing, and rotary drums (kilns) are the most commonly used process equipment for this purpose. Due to their high heat and mass transfer rates in handling bulk material, rotary drums are widely used fixtures of the

chemical, metallurgical, pharmaceutical, and catalyst industries. Calcination, thermal treatment, gasification, and thermal desorption are some of the well-known processes carried out in rotary drums (Sagastume Gutirrez et al., 2013). These processes are related to high-energy demand; therefore, more knowledge on heat transfer in rotary drums will increase operating efficiency, leading to tremendous energy savings on a global scale.

The heat transfer in a rotary drum is unique compared to other furnaces because it involves not only the gas and the moving bed of solids, but also the rotating drum wall. The heat transfer in such processes is influenced by the material properties (e.g., specific heat capacity, particle size, particle size distribution, particle shape, particle density, particle thermal conductivity) and process parameters (e.g., rotational speed, fill level, drum cross-sectional shape, friction, baffles, size of baffles, and number of baffles) (Emady et al., 2016; Yohannes et al., 2016). In understanding the heat transfer mechanism in these systems, temperature measurement is a key step. Most of the previous heat transfer research on rotary drums involved the use of thermocouples (Bongo Njeng et al., 2018; Chaudhuri et al., 2010; Herz et al., 2012a; Le Guen et al., 2013; Nafsun et al., 2018, 2017). In some cases, the thermocouples are placed inside the drum during processing (Bongo Njeng et al., 2018; Herz et al., 2012a; Le Guen et al., 2013; Nafsun et al., 2016), which is an invasive approach. For example, Herz et al. (2012) developed a continuous temperature measurement system, in which thermocouples can rotate together with the drum. However, here, the thermocouples are inserted into the particle bed and may disturb the flow of the particles. In other cases, the rotating drum is stopped at desired intervals and the thermocouples are inserted into the

drum (Chaudhuri et al., 2010). This resulted in process downtime for measurement, since the rolling had to stop to insert thermocouples into the particle bed. When the drum is stopped, the contact time between the solid bed and the wall increases, and simultaneously heat can be transferred to the particles, which might elevate the solid bed temperature. In all of the above-discussed cases, it is likely that the temperature recorded by a thermocouple is an average measure of the interstitial fluid and particle temperatures. In such cases, the average temperature of the fluid-particle might read a higher/lower value than the actual particle temperature and therefore result in a subsequent rise/fall in the recorded temperature.

In recent years, infrared (IR) thermography, a noninvasive temperature measurement device that measures IR energy and reports it as a temperature value, has been used to study granular heat transfer in rotary drums (Le Guen et al., 2013; X. Liu et al., 2016). Le Guen et al. (2013) used thermal imaging to monitor the in-situ external longitudinal wall temperature of the drum, whereas Liu et al. (2016) monitored the mixing process and heat transfer of hot and cold particles in a drum. In the former case, the particles were heated internally using hot natural gas, whereas, in the latter, the particles were heated outside the drum and poured into the system. Therefore, the continuous heat transfer from the wall-to-particles was not considered, and the wall heat transfer coefficient data extraction was not available.

The present work aims to propose a non-invasive thermal technique for experimental observation of granular heat transfer in a rotary drum. We use an IR thermography camera, enabling simultaneous recording of average particle temperature

and wall temperature (two-dimensional). In the following sections, the experimental setup, the measurement procedure, the calibration technique, and the data acquisition method will be discussed. IR thermography will be used to study the effects of fill level and rotation speed of the drum on granular heat transfer.

5.3   Mixing and heat transfer in rotary drums

An essential characteristic of rotary drums is their ability to effectively mix the drum contents. Mixing, or transverse bed motion, occurs in different forms, depending upon the flow of the particles inside the drum. A better understanding of the bed motion contributes to a precise calculation of the heat transfer and aids in designing the rotary drum. The drum rotation rate (ω), drum radius (R), particle size, and fill level all influence the particle hydrodynamics. The Froude number (Fr) is a dimensionless ratio of the centrifugal force to gravity (g), and describes the flow regimes inside the drum for various rotation rates (Mellmann, 2001):

$$Fr = \frac{\omega^2 R}{g} \tag{1}$$

Conduction heat transfer from the drum walls to the particle bed has a similar profile throughout the length of the drum. Previous researchers have shown that radial dispersion is faster than axial dispersion (Ding et al., 2001; Figueroa et al., 2010); therefore, we model heat transfer within a slice of the drum, neglecting axial dispersion. The heat transfer from the wall to the granular solid, at any given moment, can be calculated from the heat balance equation (Emady et al., 2016):

$$M_s C_{ps} \frac{d}{dt}(T_s) = \alpha e_s A_s L(T_w - T_s) \tag{2}$$

where M_s, C_{ps}, T_s, α, e_s, A_s, L, and T_w, are the particle mass, particle heat capacity, particle temperature, heat transfer coefficient, fraction of the drum circumference touched by particles, drum circumference, length of the drum, and wall temperature, respectively. The solution of Equation 2 is given by the following expression (Emady et al., 2016):

$$ln\left(\frac{T_w - T_s}{T_w - T_s{}^{\circ}}\right) = -\frac{\alpha e_s A_s L}{M_s C_{ps}} t \tag{3}$$

By plotting the experimentally determined values of the natural logarithm of the ratio of $T_w - T_S$ and $T_w - T_S{}^o$ versus elapsed time, α can be calculated from the slope of the best fit straight line drawn, using known particle and drum parameter values.

5.4   Experimental setup

The drum in the experimental setup consists of a 6" ID stainless steel cylinder with 0.5" thickness (see Fig.26). One side of the drum is closed using a 6" OD and 6 mm thick sapphire glass (University Wafer Inc., MA), specifically chosen to give a high transmittance to IR light, with a transmission range from 0.17 μm to 5.5 μm. The sapphire glass is held in place using a 5.7" ID and 11" OD titanium ring with 0.5" thickness. Titanium is chosen due to its light weight, high tensile strength, and low conductivity to minimize heat losses and heat transfer between the drum and the rollers. The other side of the drum is closed using a 6.5" OD and 6 mm thick quartz glass (G.M. Associates, Inc., CA) specifically chosen to handle high temperatures (up to 1200 °C).

Like the sapphire glass, the quartz glass is also held in place using a 6" ID and 11" OD titanium ring with 0.5" thickness. The drum rotates on the two 11" OD titanium wheels using rollers (Stainless Tumbling Media LLC, UT) with variable rotational speed from 0.5 – 14 rpm.
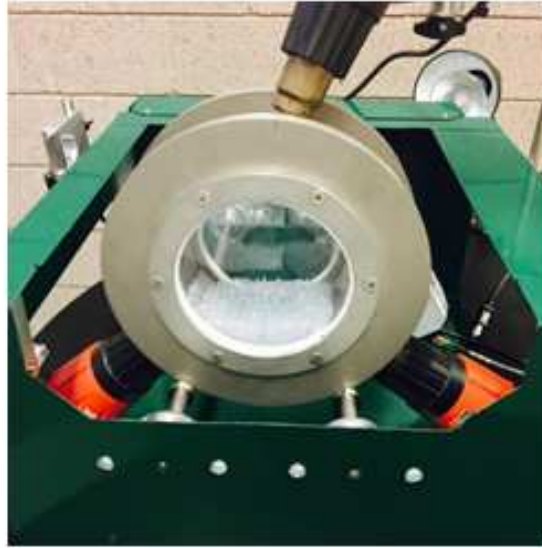
Figure 26. The experimental setup showing the rotary drum, heat guns, and rollers.

The drum is heated using three variable temperature (ranging between 120- 1150 °F) heat guns (Milwaukee Electric Tool Corp., USA) with LED displays to adjust the temperature as desired. The heat guns are placed with equal spacing around the drum, to provide effective uniform heating. 3 mm diameter silica beads (soda-lime-silica glass) purchased from Potters Industries, PA, USA, with particle density of 2.5 g/cm^3 and 99 % sphericity are used as the granular material in the experiments. Silica beads are chosen

for their high applicability as a catalyst, as well as their availability in various particle sizes. An IR camera is used to capture the temperature profile through the sapphire window. More details about the camera specifications and setup are discussed in the later sections. To calibrate the IR camera, a K-type wireless thermocouple (OMEGA Engineering, INC., CT) is used. The thermocouple records the temperature and transmits the signal to a receiver connected to a PC with the OMEGA TC central data recording software.

The particles and the inner walls of the drum are cleaned using an anti-static spray to make sure they are dust- and static-free. The particles and the drum are dried after cleaning to ensure that any excess solution is removed. Once the drum is filled with particles at room temperature, the rollers are turned on, and the drum is set to the desired rotation speed. Simultaneously, the drum wall is heated to the desired temperature using the heat guns. As the drum rotates at a constant speed, the heat guns placed around the drum heat the drum wall uniformly. The IR camera recording is started, and the experiment is run until the average particle bed temperature reaches steady state. Then, the recording is stopped, and the heat guns and rotation are turned off. The drum is removed for disassembly, emptied, and left to cool for the next run.

5.5   Camera setup

An FLIR A6701SC, 640 x 512 resolution, IR camera is used for continuous, noninvasive temperature measurement. Data from the camera is recorded in the FLIR ResearchIR software, which allows for real-time viewing and post-processing data

analysis. The IR camera is sensitive in the 1.5–5.1 µm spectral range. The camera is placed on a tripod in front of the drum, and the position of the tripod is marked to replicate the setup for all of the experiments. The experiments are performed in a completely dark environment, with blackout curtains covering the windows, so that light does not interfere with the IR thermography. The IR camera is internally cooled automatically, and its lens is transparent to infrared radiation. When the lens cools down, due to its low temperature, the radiation leaving the camera through its lens corresponds to room temperature blackbody radiation. This means that, when placing the camera perpendicular to the sapphire window, a cold spot would be visible. In order to eliminate the cold spot, the IR camera is placed at a small angle with respect to the drum side window. The camera tripod position is marked on the ground to ensure consistency between runs. The position that offers the optimal field-of-view of the inner drum wall and particle bed is achieved by placing the camera lens approximately 65 cm away from the drum. A schematic view of the drum and IR camera setup is shown in Fig. 27
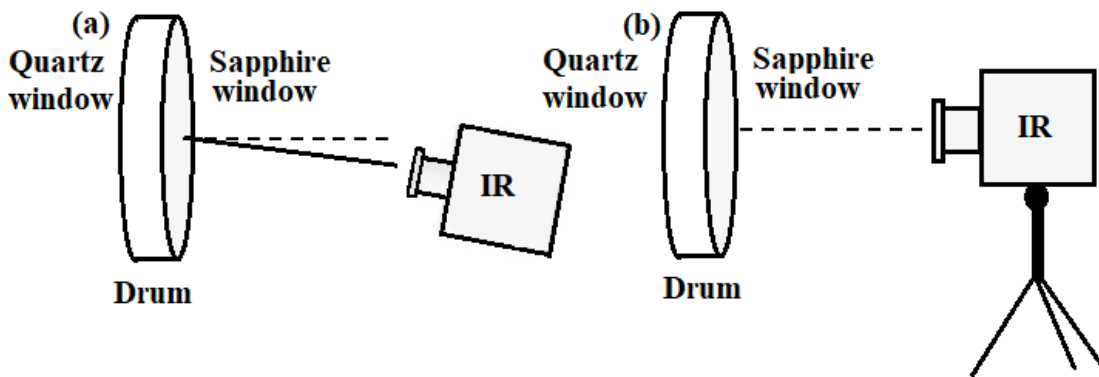
Figure 27. (a) Top view and (b) side view of the experimental setup illustrating the arrangement of the IR camera with respect to the rotary drum.

5.6   IR camera calibration and data acquisition

A heated body (or an object at a temperature above absolute zero), such as a hot particle, emits infrared radiation in all directions. When this energy contacts other objects (e.g., other particles, the drum wall, or the drum window), the energy is absorbed, reflected, or transmitted through the object. Therefore, the fate of incident radiation on an object is determined by three wavelength dependent fractions, namely, absorptance (a), reflectivity (r), and transmittance (t). Since the radiation is either absorbed or reflected or transmitted, we have $a + r + t = 1$. For an object that should be transparent to the IR radiation, like the window of the drum, the transmittance should be close to 1. Therefore, a sapphire window is used, which has a transmittance of about 0.9. Further details on IR radiation can be found in the literature (DeWitt and Nutter, 1988; Patil et al., 2015).

For any particular wavelength and temperature, the amount of infrared radiation emitted depends primarily on the emissivity of the object's surface. Emissivity is defined as the ratio of the energy radiated from a material's surface to that radiated from a perfect emitter (i.e, a blackbody), at the same temperature and wavelength and under the same viewing conditions. It is a dimensionless number between 0 (for a perfect reflector) and 1 (for a perfect emitter). The emissivity of a surface depends not only on the material but also on the morphology of the surface. The emissivity also depends on the temperature of the surface as well as wavelength and angle. Unfortunately, because the emissivity of a material surface depends on many chemical and physical properties, it is often difficult to estimate. It must either be measured or modified (e.g., by coating the surface with high emissivity black paint), to provide a known emissivity value.

The IR camera outputs signals referred to as "counts" for each energy input it receives. The counts value is stored as a 14-bit number, so it has a range of 0 to 16383. Every pixel in an IR image has a respective count value. As the maximum count value for each pixel is 16383, the IR camera cannot record anything higher than that value. For example, when beginning an experiment in the 10 – 90 °C range, the counts value will increase until it approaches 16383 at 90 °C, at which point the camera is "out of range," and cannot interpret the data. This problem is easily avoided by monitoring the temperature throughout the experiment and selecting a higher temperature range available in the software. In the current work, the drum operates between 20-200 °C. To gather accurate temperature data over the complete temperature range, the camera is operated in three different settings: 10 – 90 °C, 35 – 150 °C, and 80 – 200 °C. The maximum count value in a frame for a particular setting is monitored, and once the maximum is reached, the camera range is switched to a higher value. For example, when beginning an experiment in the 10 – 90 °C range, once the maximum count reaches nearly 15000, the frame number is noted and the camera setting is changed to further record data in the 35 – 150 °C range. This way, the IR data is recorded continuously by changing the camera range, without stopping the recording. Since the range is changed once the maximum count value of the frame reaches approximately 15000, the temperature of the frame might not reach the maximum temperature in a particular setting. As seen in Fig. 28, the cursor can be positioned anywhere on the IR image frame to extract the x and y coordinates of the pixel position and the count value of the corresponding pixel. For example, in Fig. 28, (265, 157) is the position of the pixel and 5485 is the count value of the pixel.
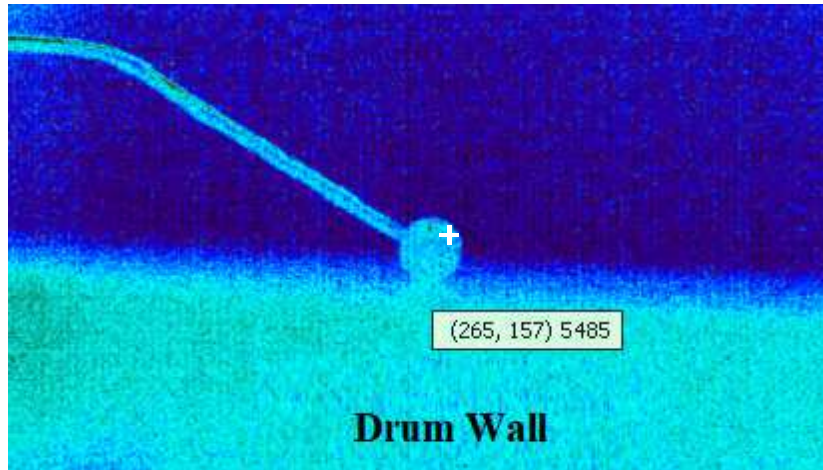
Figure 28. IR image of a single particle placed on the drum wall, touching a thermocouple that is recording the temperature.

For the emitted energy to reach the sensor in the infrared camera, it must pass through the drum window and the atmosphere between the window and the camera lens. Therefore, the calculated temperature value is a function of the emissivity of the particles, the distance between the camera and object, the transmission of the window, and the conditions of the atmosphere (e.g., temperature, humidity, and distance) where the energy passes through on its path from the window to the camera. The FLIR IR camera requires these values in order to convert the thermal signals/counts to a temperature value. However, as mentioned above, every material has different emissivity, and it is not trivial to derive the emissivity value of any material. To overcome this difficulty, we have performed our own calibration for both the particle and the drum wall, for our setup. The calibration is performed by placing a single particle inside the drum, very close to the sapphire window so it is visible for the IR camera. The particle is held in place using a washer to prevent the particle from rolling, and three thermocouples are placed in contact

with the particle through a hole in the quartz window, as shown in Fig. 29. The drum wall is heated, and the temperature profile of the particle is recorded at 1Hz using both the thermocouples and the IR camera simultaneously. The thermocouple temperatures are plotted as a function of the infrared counts value, and a polynomial trend line is fit to create the calibration curve (see Fig. 30). This calibration curve is used in the subsequent data processing procedure to convert the counts to temperature.

(a)   (b)
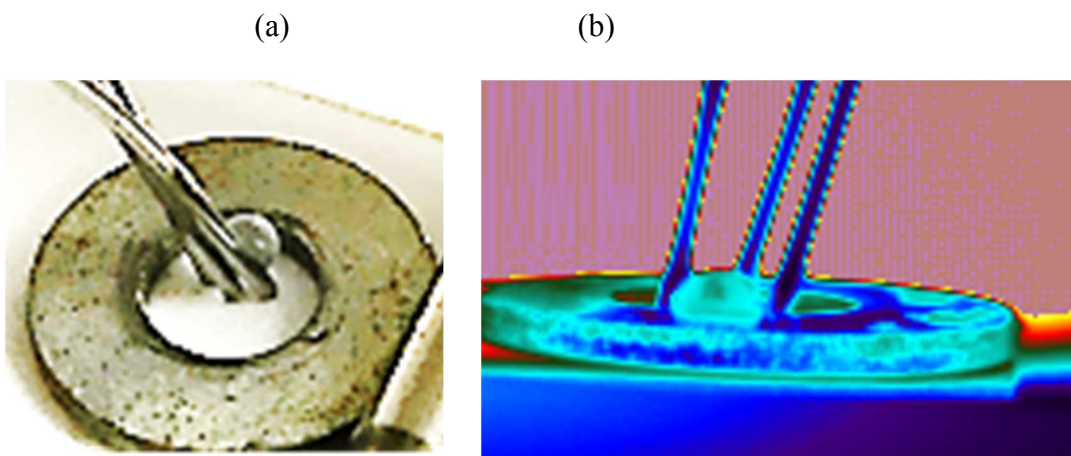
Figure 29. Particle calibration setup showing: (a) three thermocouples in contact with the particle, held in place using a washer, and (b) the corresponding IR image.
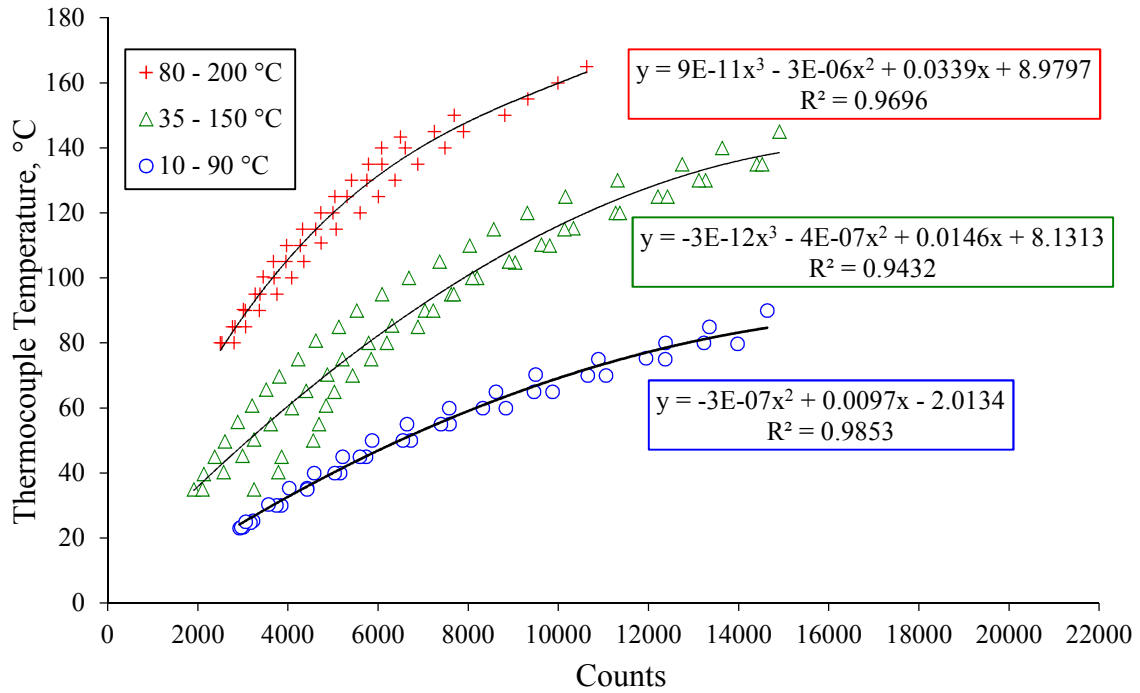
Figure 30. Particle temperature calibration curves for the IR camera, showing the thermocouple temperature versus the IR count for each temperature range.
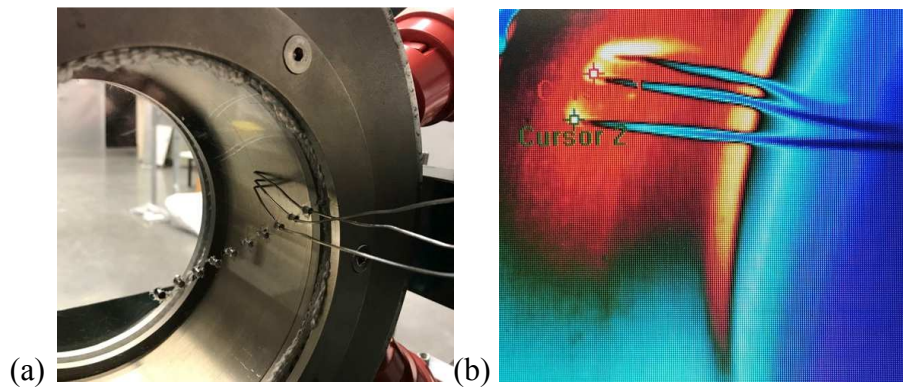
Figure 31. Wall calibration setup showing: (a) thermocouples in contact with the heating drum wall and (b) the corresponding IR image.

A similar calibration is done for the drum wall temperature. Since the emissivity of the drum wall is different from that of the particle bed, the camera is calibrated separately for the drum wall. For this, the empty drum is placed on the rollers and three thermocouples are positioned on the wall close to each other, as shown in Fig. 31(a). All three heat guns are pointed at the same location on the exterior of the drum to quickly heat the drum from room temperature to 200 ˚C. As the drum wall temperature rises, the temperature profile is recorded using the IR camera (see Fig. 31(b)) and thermocouples. Fig. 32 shows the drum wall calibration curves for the three camera ranges. From Fig. 30 and 32, it can be seen that the particle calibration data points are more scattered and have a lower R^2 when compared to the wall data. It is suspected that the temperature difference is due to thermal softening, a heat treatment process in which the local increase in temperature can result in softening of the material, which leads to a heat gradient and changes in the material grain structure (Meyers, 2001). With thermal softening, it is possible that the particle surface exhibits a heat gradient, and the three thermocouples read slightly different temperatures.
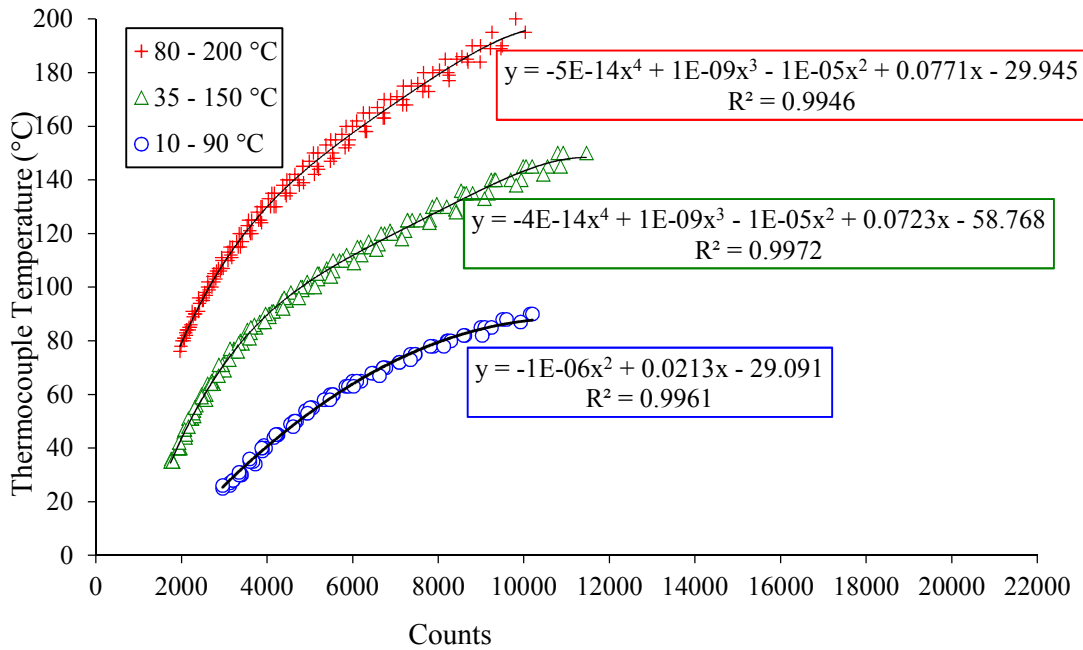
Figure 32. Wall temperature calibration curves for the IR camera, showing the thermocouple temperature versus the IR count for each temperature range.

The FLIR ResearchIR software allows the user to select a "region of interest" (ROI) to view and export data for that region. An ROI is drawn on the inner drum wall and around the particle bed, as shown in Fig. 33, to extract the average counts of the drum wall and the particle bed, respectively. The extracted data is exported into a MATLAB script and converted into temperature values using the calibration curves shown in Fig. 30 and 32.
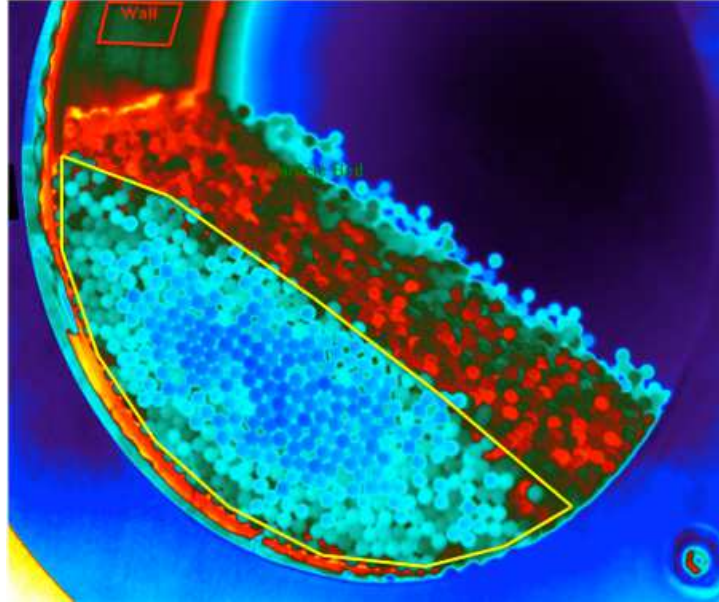
Figure 33. Sample region of interest (ROI) selection for the drum wall (red) and the particle bed (yellow).

5.7   Results and Discussion

Thermal images captured using the IR camera have the potential to be post-processed and used for analyzing the hydrodynamic behavior of the particle bed, just like high-speed images (Santos et al., 2015). Therefore, for a qualitative analysis, the captured IR videos are used to calculate the theoretical flow profiles predicted by Mellmann (2001) using the Froude number (*Fr*) (Equation 1) and fill level. Also, the flow profiles observed from the recorded IR frames are compared with the theoretically expected flow profiles. Experiments are carried out by varying the drum rotation speed from 2-10 rpm and fill level from 10-25 %. These results are presented in Table 7.

Fill %, rpm	Fr (x 10^{-4})	Theoretical Flow Profile based on Fr	Observed Flow Profile from IR images
10 %, 2 rpm	3.4	Rolling or Slumping	Slumping - Surging
10 %, 6 rpm	31	Rolling or Slumping	Slumping - Surging
10 %, 10 rpm	85	Rolling	Rolling - Slumping - Surging
17.5 %, 2 rpm	3.4	Rolling	Rolling - Slumping - Surging
17.5 %, 6 rpm	31	Cascading or Rolling	Slumping - Surging
17.5 %, 10 rpm	85	Cascading or Rolling	Rolling - Slumping
25 %, 2 rpm	3.4	Rolling	Rolling - Slumping - Surging
25 %, 6 rpm	31	Cascading or Rolling	Rolling - Slumping - Surging
25 %, 10 rpm	85	Cascading or Rolling	Rolling - Slumping

Some runs have more than one theoretical flow profile because each flow regime has a wide range of potential Fr and fill levels. As the particles are heated, it is observed that a bed flow transition takes place. Once the experiment started, the observed flow profiles generally agreed with the theoretical flow profiles for all runs, and the flow profile slowly transitioned into another flow regime. All runs in the rolling regime transitioned into the slumping regime, where the particle bed was continuously elevated and leveled off by successive avalanches at the surface. Furthermore, the slumping regime transitioned into surging, where the particles within the bed were no longer mixing together. Instead, the bed moved as one mass, oscillating back and forth along the drum wall. It is suspected that as the particles are heated, particle-particle friction takes

over and inhibits the bed movement, causing a transition from the initially observed flow profile.

For a better visual understanding, the transition can be explained using the IR images of temperature evolution for the 25 % fill level and 6 rpm case (see Fig. 34). In Fig. 34(a), at 10 s, all particles are at room temperature, with a slightly elevated wall temperature. In Fig. 34(b), at 300 s, the particles move uniformly, with static flow of a particle layer on the surface, while the larger part of the bed is transported upwards by solid body rotation. The top layer and side view of the particle bed show equal concentrations of hot and cool particles, indicating that a uniform intermixing is achieved. This type of flow is characterized as being in the rolling regime, with a nearly leveled bed surface. At 900 s, from Fig. 34(c), it can be seen that the particles heat up, forming a hot outer core and a cool inner core. As the particles in contact with the drum wall heat up, they roll over and refresh the surface with hot particles. This type of flow is classified as being in the slumping regime, which results in less solid mixing. From Fig. 9(c), it can be seen that avalanches are formed at the top of the bed, which is a characteristic of the slumping motion. At 1200 s, from Fig. 34(d), it can be seen that the bed is heated as a single mass. Here, the bed slides from the wall, and little to no mixing is observed. This type of flow is characterized as being in the surging regime. At this time, the particle bed and the drum wall are heated to a point where the friction between the wall and the particle bed decreases, and the bed constantly slides from the wall. Here, it is suspected that heating results in softening of the particle and drum surfaces, resulting in slipping.
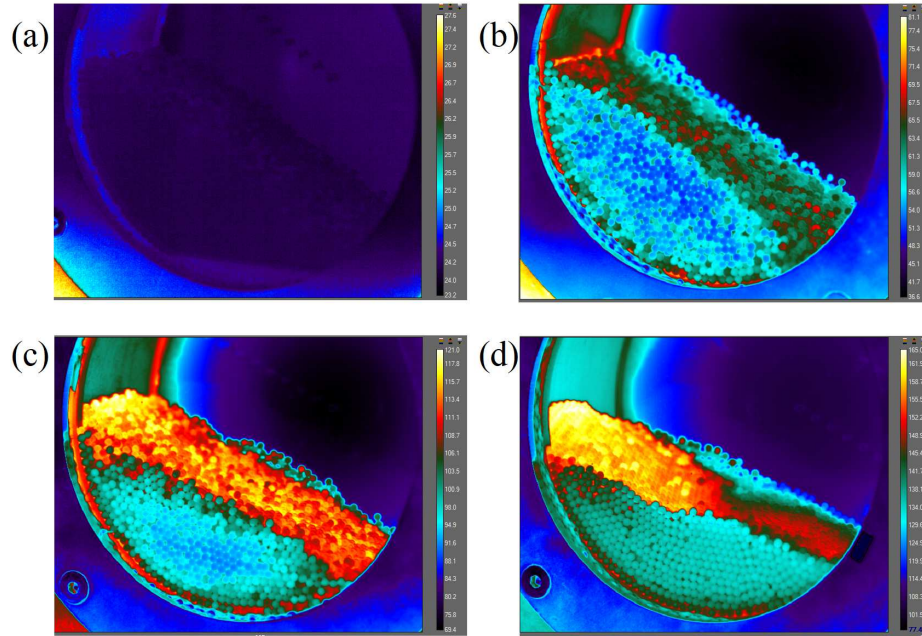
Figure 34. Thermal images showing the temperature evolution for 25% fill level and 6 rpm, at t = (a) 10 s, (b) 300 s, (c) 900 s, and (d) 1500 s.

Although the observed flow profiles agree well with the theoretical profiles for most of the cases, there are a few discrepancies. For example, cascading flow is never observed, although the calculated *Fr* did lie in the cascading regime for a few of the cases. Such discrepancies between the theoretical and observed flow profiles are attributed to the assumptions under which Mellmann (2001) developed the flow profiles. Mellmann (2001) only considered the frictional effects between the wall and the particle bed, with no heat involved. However, the current experiments involve heat transfer, and the observations suggest that particle-particle friction is another critical factor in determining the bed flow profile when the particle bed is heated.
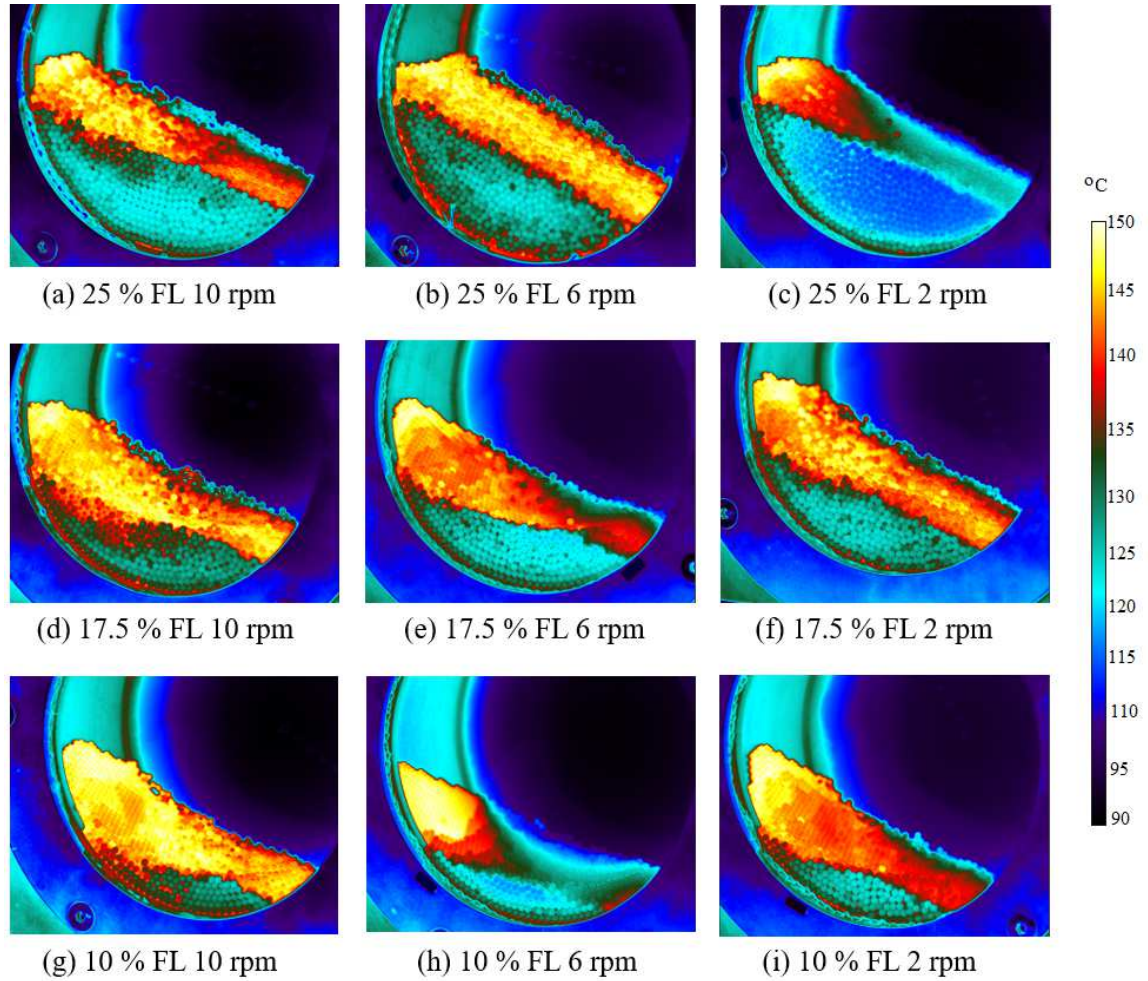
Figure 35. Thermal images at t = 1200 s for each run. The scale is an average of the individual scales from each picture shown.

Fig. 35 shows the thermal images for each set of operating parameters. As rotation rate increases, moving from right to left, the particle bed temperature uniformity increases. Also, from Fig. 35 (a, d, g), it can be seen that a larger concentration of hot particles is found on the top part of the bed, indicating that hot particles are refreshed quickly on the surface. This suggests that an increase in rotation rate enhances mixing and subsequently enhances heat transfer within the drum. A rolling bed, which occurs

with increasing rotation rate (see Table 7), increases the heat transfer between the drum wall and particle bed by increasing the number of wall-particle and particle-particle contacts. As fill level increases, moving from bottom to top in Fig. 35, there is no clear trend in temperature uniformity. Although there is less mass and therefore less resistance to heating the particle bed at lower fill levels, the hydrodynamics are impeded since the bed quickly tends to the slumping or surging regime.
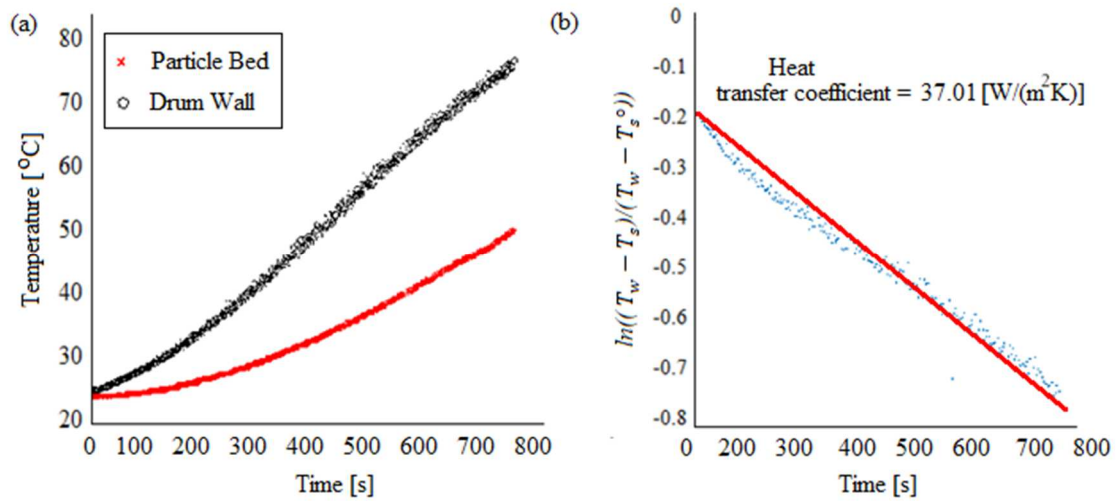
Figure 36. Temperature profiles for 25 % fill level and 10 rpm: (a) Calibrated wall and particle bed temperatures, and (b) Variation of scaled temperature difference with time.

For a quantitative understanding, the wall to solid heat transfer coefficient is calculated for each run. Using the calibrated average particle bed temperature (T_S) and wall temperature (T_W) values, α is calculated using the slope of the natural log of the normalized particle bed temperature versus time (see Equation 3, Fig. 36). This slope is

constant once the average particle bed temperature reaches a steady state, so only the first few minutes of data is sufficient.
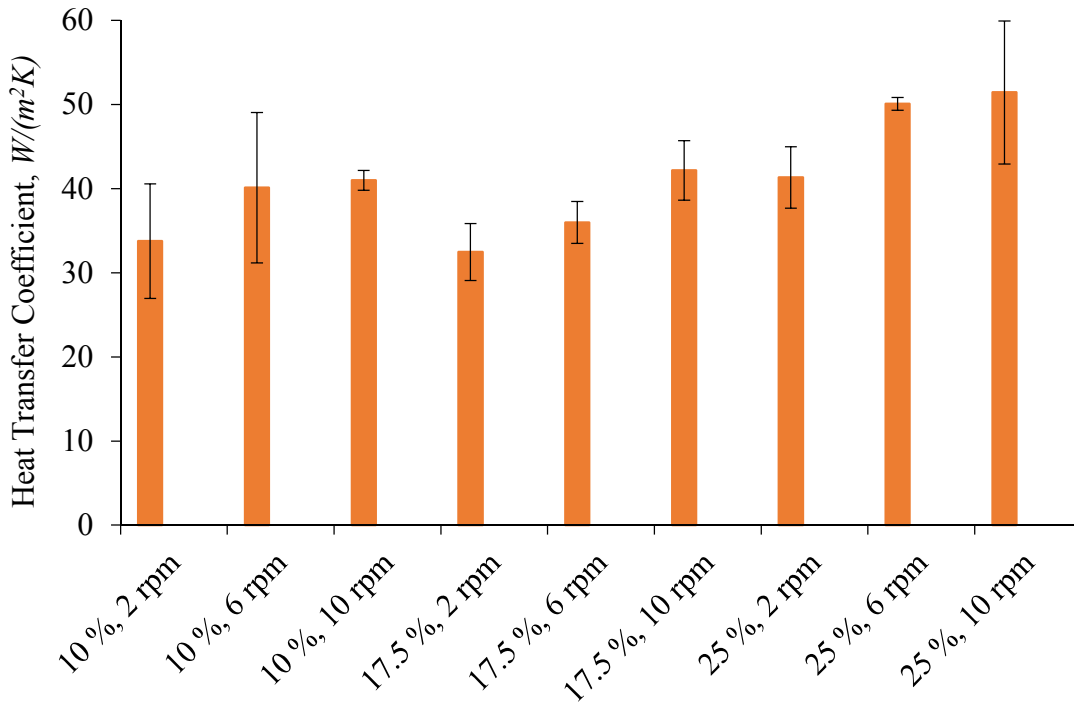
Figure 37. Average wall-to-solid heat transfer coefficient for all fill level and rotation rate combinations studied. The error bars represent 95 % confidence intervals.

For a constant fill level, increasing the rotation rate increased the heat transfer coefficient (see Fig. 37). This confirms the expectation that a rolling bed increases the heat transfer between the drum wall and the particle bed by increasing the number of wall-particle and particle-particle contacts. Although there is less mass and therefore less resistance to heating the particle bed at lower fill levels, the hydrodynamics are impeded since the bed tends toward the slumping regime. Increasing the fill level increases the

number of wall-to-particle contacts and the mass of the particle bed to be heated. However, increasing the fill level had the competing effects of improving the hydrodynamics, while also increasing the resistance to heat transfer due to the larger bed mass. For a constant rotation rate, this caused the heat transfer coefficient to decrease as fill level increased from 10 % to 17.5 %, and increase as fill level increased from 17.5 % to 25 %. Therefore, a clear trend explaining the effect of fill level is not observed in the current study. In every case, the average bed temperature achieved is a maximum at higher rotation rates and higher fill levels.

5.8   Conclusions

A non-invasive infrared imaging technique is proposed for experimental observation of the flow regime and heat transfer process in a rotary drum. A detailed IR camera calibration and data acquisition method is presented. This study investigated the effects of fill level and rotation rate on the steady-state average bed temperature, using 3 mm silica beads in a stainless-steel rotary drum. The drum is heated externally to supply heat to the system via wall to particle bed conduction. Increasing the rotation rate resulted in an increase in the heat transfer coefficient, with fill level having no conclusive effect. The proposed technique is only able to capture the thermal data from an exposed surface of the particle bed. Future work is needed to understand the relationship between the process observed from the bed surface and that in the whole bed.

Our results demonstrate the proposed measuring approach, with which information about the flow regime and heat transfer process can be obtained

simultaneously. However, there are a few limitations to this technique that are similar to other optical and visual- based measuring methods. The current technique is only able to capture 2D images of an exposed bed surface, and therefore thermal data of only the surface particles on the top of the bed and those in contact with the window are extracted. Thus, only radial variation in the temperature profile is captured.

6   CONVECTION HEAT TRANSFER IN A ROTARY DRUM USING DEM

6.1   Abstract

This work utilizes infrared imaging to investigate the effects of fill level and rotation rate on the particle bed hydrodynamics and the average wall-particle heat transfer coefficient in a rotary drum. 3 mm silica beads and a stainless-steel rotary drum with an ID of 6 in. and a length of 3 in. are used at fill levels of 10 %, 17.5 %, and 25 %, and rotation rates of 2 rpm, 6 rpm, and 10 rpm. The effects of these factors in the presence of conduction and forced convection are investigated. It was concluded that the inlet air velocity is dominated by the particle friction effects and maintains a uniform flow profile. The maximum heat transfer coefficient was achieved at a high rotation rate and high fill level. Heat losses from the system were dominated by natural convection between the hot air in the drum and the external surroundings.

6.2   Introduction

Particulates are solid materials that exhibit properties of solids, liquids, and gases due to their ability to deform like a solid, flow like a liquid, and compress like a gas. They vary significantly in size, from fine powders to large rocks and boulders. The characteristics of each particulate system are different and depend on the material composition, particle size, particle size distribution, and shape, to name a few factors. For example, a single grain of sand may behave much differently than a sandbox. Applying enough downward force to a single sand particle will likely shear it into multiple smaller

particles. The same force applied to a sandbox will do nothing but force the particles to compress without breakage. This pseudo-random nature of particulates is what makes them challenging to study and model compared to conventional solids, liquids, and gases (Rhodes, 2008).

Many industries use particulates to create an array of products. Powders are present in the pharmaceutical, cement, food, and cosmetic industries, among many others. Each industry may utilize different unit operations involving heat and mass transfer between particles. The rotary drum is one example of a common piece of equipment used for heating, drying, agglomeration, and reacting (Rhodes, 2008). One specific application is the production of cement clinker. According to the International Energy Agency (2019), this process requires more than 3 GJ per ton of clinker produced. In 2016, the cement industry consumed about 1019 J, or 2 % of global energy consumption. Large energy requirements and insufficient models necessitate a high demand for research on rotary drums. Even minuscule increases in operating efficiency can result in dramatic energy savings due to the large global scale of particulate processing. A challenge is that companies do not want to shut down processes for optimization research because shut down results in lost revenue. Therefore, more research is needed at the lab and pilot plant scale to improve these processes.

Heat transfer inside rotary kilns occurs via conduction, convection and radiation. The heat transfer modes can be divided into heat transfer outside, inside and across the kiln wall. Each mode may involve one or more heat transfer mechanisms. In general, radiative transfer is dominant at > 1000°C (Barr et al., 1989; Gorog et al., 1981, 1982).

The relative importance of each mode depends on the solid, gas and kiln wall thermo-physical properties; kiln designs; and kiln operating conditions. A good understanding of the conduction heat transfer and the effectos of rotation speed and fill level are presented in Chapters 4 and 5 using both simulations and experiments. The current chapter focuses on understanding the convection heat transfer mechanism in rotary drums.

For indirect heating operations at temperatures up to 873°C, Ding et al. (2001) indicated that heat transfer from the covered wall to the covered bed is the dominant mechanism in supplying heat to the bed. Heat transfer between the freeboard gas and the exposed bed accounts for only a small portion. The heat transfer rate between the freeboard gas and the exposed wall may be comparable to that between the covered wall and the covered bed, indicating that both steps could be controlling. Li et al. (2005) reported that heat transfer from covered wall to covered bed and convection heat transfer from freeboard gas to exposed bed play a crucial role in the fast heating of solids at the kiln inlet (up to 427 ˚C). Gorog et al. (1982) stated that in the high temperature regions of the kiln (>927 ˚C), 60 to 80 % of the heat received by the solids results from their radiative interaction with the freeboard gas and exposed wall. With the low temperature regions of the kiln (>927 ˚C), 70 % of heat received by the solids results from the combination of freeboard convection and the regenerative heating of the wall. Tscheng and Watkinson (1979) and Barr et al. (1989) indicated that the heat transfer coefficients between the freeboard gas and exposed bed are in the order of five to ten times the values between the gas and the exposed wall.

There have been several efforts to quantify the heat transfer coefficient due to convection between the particle bed and fluid (air), and between the wall and fluid. The fluid-particle convective heat transfer coefficient was calculated to be about 3 W/(m²K) by Debacq, Thammavong, Vitu, & Dupoizat (2011). Shi, Vargas, & McCarthy (2008) over-estimated the fluid-particle convective heat transfer coefficient to be a maximum of 8 W/(m²K). Calculations for the wall-fluid heat transfer coefficient were less than 1 W/(m²K) (Njeng et al., 2018). Since these heat transfer coefficients are at least one order of magnitude smaller than typical values for the wall-particle conductive heat transfer coefficient, the effects of fluid-particle and wall-particle convection are neglected when there is no moving fluid in the drum.

Shi et al. (2008) calculated the fluid-particle heat transfer coefficient using correlations for the Nusselt number. For low fluid velocities ($Re_f < 100$):

$$Nu = \frac{h_f d_p}{k_f} = 0.03 Re_f^{1.3} \tag{1}$$

where Nu, h_f, k_f, d_p, and Re_f are the Nusselt number, fluid-particle heat transfer coefficient, fluid thermal conductivity, particle diameter, and fluid Reynolds number, respectively. The Reynolds number is calculated by:

$$Re_f = \frac{d_p u_f \rho_f}{\mu_f} \tag{2}$$

where d_p, u_f, ρ_f, and μ_f are the particle diameter, fluid velocity, fluid density, and fluid viscosity, respectively. The Biot number is calculated to show that the internal resistance is low for silica, indicating that the particles heat as isothermal bodies with no internal temperature gradient (Shi et al., 2008; Chaudhuri et al., 2010; Oschmann & Kruggel-Emden, 2018). The Biot number can be calculated using:

$$Bi = \frac{h_f r_p}{k_p} \tag{3}$$

where Bi, r_p, and k_p are the Biot number, particle radius, and particle thermal conductivity, respectively. As the particle thermal conductivity increases and the particle size decreases, Bi approaches 0. For $Bi \ll 1$, the isothermal particle assumption is valid. The available experimental data in this field relies exclusively on thermocouples to measure temperatures of particulate systems. Some researchers have used imaging techniques to study the flow behavior of particulate systems, such as Lueptow, Akonur and Shinbrot (2000). However, there is a lack of research employing infrared thermal imaging techniques to rotary drum applications. This research aims to fill this gap by studying the convection heat transfer mechanisms in the rotary drum using the infrared thermography methodology developed in Chapter 5. The wall-particle heat transfer coefficient is calculated using Equation 4 to understand the conduction and convection behaviour. Further, the effects of fill level and rotation rate on heat transfer in the rotary drum is also investigated.

6.3   Experimental Setup

The rotary drum setup used in this study is presented in Chapter 5.4. However, to study the effects of convection heat transfer, the setup was modified to introduce forced convection into the drum system. For the conduction setup, one side of the drum is closed using a quartz window and another side is covered using a sapphire window. For the convection studies, besides the sapphire window that is used for IR imaging, a quartz window with holes to pump hot air into the drum is used.
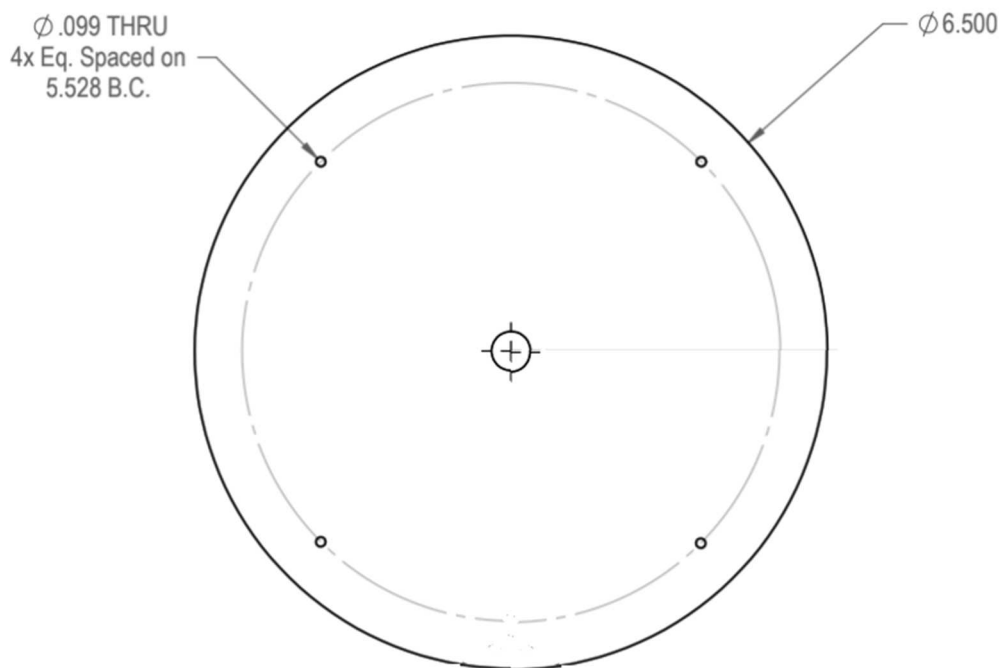
Figure 38. Quartz window specifications with air inlet hole in the center. All dimensions are in inches. Φ indicates diameter and B.C is bolt circle.

The quartz window used, pictured in Fig. 38, features a central inlet hole for hot air to be forced into the drum for internal heating. It also has four smaller holes around the edge to let air outside, in order to release the pressure from inside the drum. The particles

of interest in this study are soda-lime-silica glass beads. Silica is a common catalyst

support material, so a good understanding of its heat transfer properties will help improve

its operating efficiencies (Chaudhuri et al., 2010). The beads are 3 mm in diameter with

90 % sphericity and a thermal conductivity of 0.7 – 1.3 W/(mK), from Potters Industries.

Four heat guns are used to heat the drum externally and internally. Three external

heat guns are positioned equidistantly around the drum to heat the drum wall for

conductive heating to the particle bed inside the drum. The internal heat gun is attached

to an air duct that connects with pipe fittings to a temperature sensor and the air inlet port.

This heat gun serves to insert a hot air stream into the drum to heat the particle bed inside

the drum via forced convection. The heat gun settings are given in Table 8.

Table 8. Heat Gun Settings Used for the Four Heat Guns.

	Temperature (˚C)	Flow rate (cfm)
3 X External heat guns	316	17.6
1 X Internal heat gun	149	10.6

An FLIR A6700SC infrared camera is used for continuous, noninvasive

temperature measurement. Data from the camera is recorded in the FLIR ResearchIR

software, which allows for real-time viewing and post-processing data analysis. The

camera measures electromagnetic radiation, so natural and artificial lighting in the room

can skew measurements. More details about the IR camera, calibration, and data

acquisition are presented in Chapter 5. The experiments are performed in a completely

dark environment, with blackout curtains covering the windows. The entire rotary drum

setup is shown in Fig. 39.
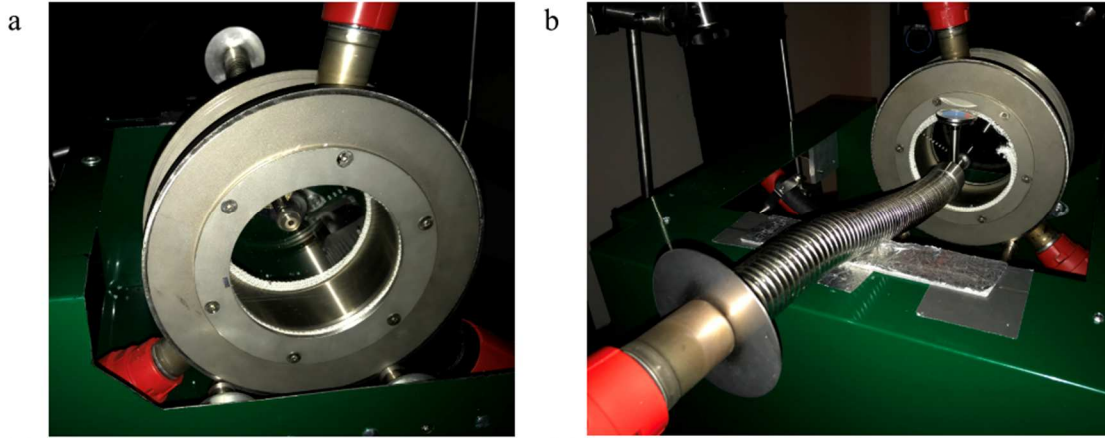
Figure 39. Rotary drum experimental setup. a) Front view of empty drum with

sapphire window. b) Rear view of empty drum with air inlet duct and quartz window.

6.4   Experimental Procedure

There are four heat sources used: one heat gun to supply hot air to the inside of

the drum, and three heat guns for heating the exterior drum wall. The schematic showing

the heat sources is presented in Fig. 40. Dry silica particles are weighed to the desired fill

level and placed inside the drum. The quartz window is secured in place with the titanium

plate and bolts, and then the drum is placed on the rollers. The rotation motor is started at

the desired rotation rate, and the heat guns are turned on. The infrared camera recording

is started and the experiment is run until the average particle bed temperature reaches

steady state. As the system temperature increases, the camera temperature range is

switched in the ResearchIR software from $10 - 90$ °C to $35 - 150$ °C, and then to $80 -$

200 °C. The frame number for each range transition is recorded so the applicable calibration curve can be applied during data analysis. Once the average particle bed temperature reaches steady state, the recording is stopped and the heat guns and rotation are turned off. The drum is removed for disassembly, emptied, and left to cool for the next run. The particles are rinsed with water to remove any dust or particulate contaminants and left to dry overnight. To determine the effects of rotation rate and fill level on the average wall-particle heat transfer coefficient, rotation speeds of 2, 6, and 10 rpm are used at fill levels of 10, 17.5, and 25 %. The experimental setup can achieve a maximum rotation speed of 14 rpm; therefore, rotation speeds well below 14 rpm are selected.
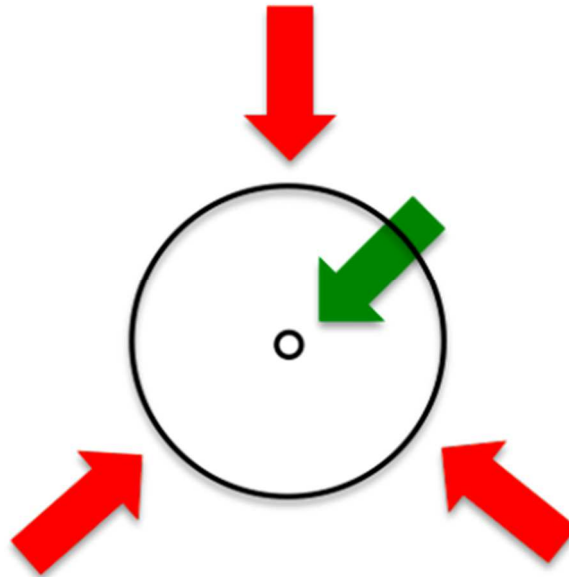
Figure 40. Schematic of the experimental setup using external (red) and internal (green) heat sources.

6.5 Results and Discussion

6.5.1 Flow Profile

A qualitative analysis of the flow profile is done using the captured IR videos. The videos are used to calculate the theoretical flow profiles predicted by Mellmann (2001) using the Froude number (*Fr*, Equation 2.2) and fill level. Also, the flow profiles observed from the recorded IR frames are compared with the theoretically expected flow profiles. These results are presented in Table 9.

Table 9. Theoretical and Observed Flow Profiles Based on Froude Number (Fr) and Fill Level.

Fill %, rpm	*Fr* (x 10⁻⁴)	Theoretical Flow Profile based on *Fr*	Observed Flow Profile from IR images
10 %, 2 rpm	3.4	Rolling or Slumping	Slumping
10 %, 6 rpm	31	Rolling or Slumping	Slumping
10 %, 10 rpm	85	Rolling	Rolling
17.5 %, 2 rpm	3.4	Rolling	Slumping
17.5 %, 6 rpm	31	Cascading or Rolling	Rolling
17.5 %, 10 rpm	85	Cascading or Rolling	Rolling
25 %, 2 rpm	3.4	Rolling	Rolling
25 %, 6 rpm	31	Cascading or Rolling	Rolling
25 %, 10 rpm	85	Cascading or Rolling	Rolling

Some runs have more than one theoretical flow profile because each flow regime has a wide range of potential *Fr* and fill levels. Once the experiment started, the observed flow profiles generally agreed with the theoretical flow profiles for all runs. It is worth noting that in the presence of pure conduction (Chapter 5.7), as the particles are heated, it is observed that a bed flow transition takes place. Once the experiment started, the observed flow profiles generally agreed with the theoretical flow profiles for all runs, and the flow profile slowly transitioned into another flow regime (see Table 7). It was observed that particle-particle friction took over and inhibited the bed movement, causing a transition from the initially observed flow profile. However, in the case of conduction and convection heat transfer presented in this chapter, the particles are in the presence of the hot inlet air stream. This air in the drum effectively fluidized the particle bed so that the fluidization velocity dominated the friction coefficient. In this case, the particle bed followed the same flow profile throughout each run as the temperature increased. In the case of 17.5 % fill level and 2 rpm, the theoretical flow did not match the observed flow profile; this is because each flow regime has a wide range of potential *Fr* and fill levels.

Although the observed flow profiles agree well with the theoretical profiles for most of the cases, there are a few discrepancies. For example, in the case of 17.5 % fill level and 6 rpm, cascading flow is never observed, although some of the calculated *Fr* did lie in the cascading regime. Discrepancies such as this between the theoretical and observed flow profiles are attributed to the assumptions under which Mellman (2001) developed the flow profiles. He only considered the frictional effects between the wall

and particle bed. However, the experimental observations suggest that particle-particle friction dominates when the particle bed is heated.

6.5.2   Heat Transfer

Fig. 41 shows the thermal images for each set of operating parameters. The images are captured at the point where the average bed temperature is determined to reach steady-state. The temperature scale is calculated as an average of the scales shown on each individual image. As rotation rate increases, moving from right to left, the particle bed temperature uniformity increases. Also, from Fig. 41 (a, d, g), it can be seen that a larger concentration of hot particles is found on the top part of the bed and along the drum wall, indicating that hot particles are heated due to wall-particle conduction and particle-freeboard gas convection. This suggests that an increase in rotation rate enhances mixing and subsequently enhances heat transfer within the drum. A rolling bed, which occurs with increasing rotation rate (see Table 9), increases the heat transfer between the drum wall and particle bed by increasing the number of wall-particle, particle-particle, and particle-air contacts. As fill level increases, moving from bottom to top in Fig. 41, a similar temperature profile is observed, where the particles are heated along the drum wall and along the freeboard gas. As time progress, heat is transferred through particle-air-particle convection as well. However, as fill level increases, there is no clear trend in temperature uniformity. It can also be observed that, although each particle bed was said to be at steady-state since the average temperature stopped increasing, large radial temperature gradients still existed in each case. This was especially true at the low rotation rates, seen in Fig. 41 (c, f, i). Additionally, the top layer of particles was much

hotter than the bulk average, showing the impact of convection from the hot inlet gas in this setup.
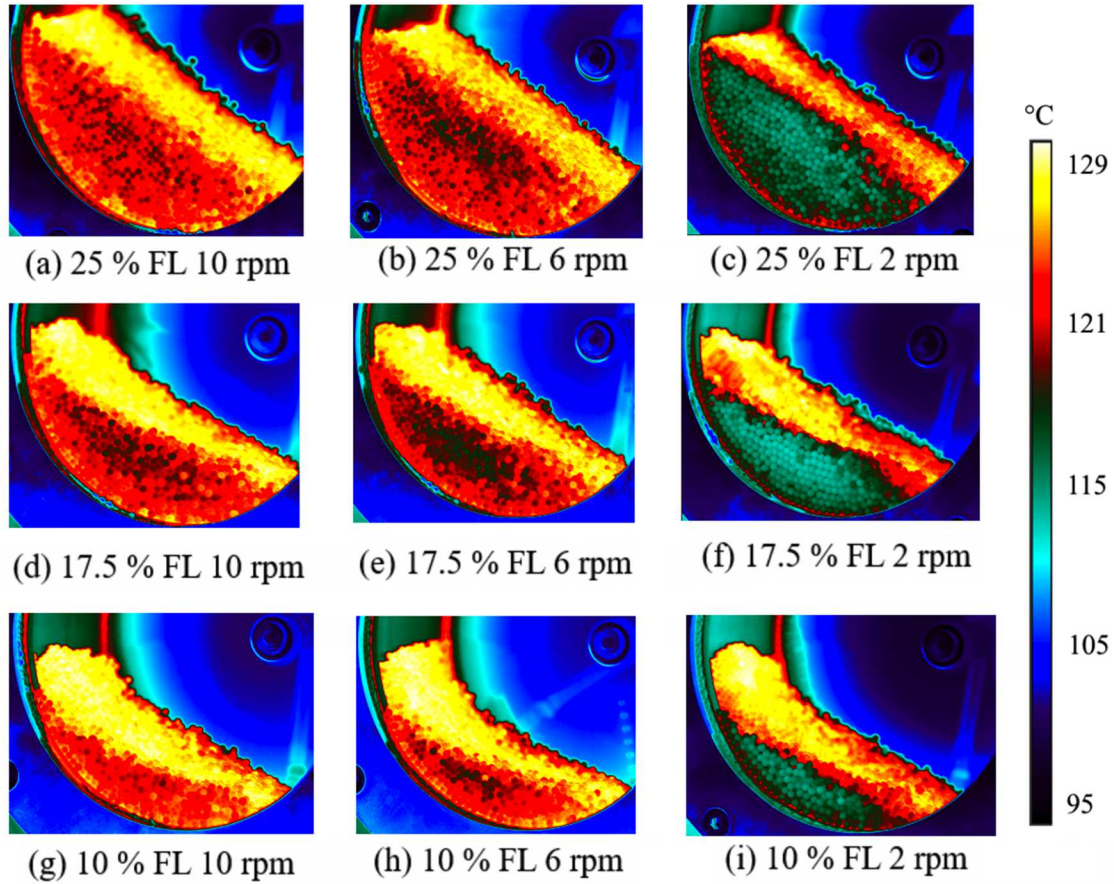
Figure 41. Thermal images at steady-state average bed temperature. The scale is an average of the individual scales for each picture shown.

The temperature profiles for each run are also analyzed to observe trends in the average bed temperature over time. The curves presented in Fig. 42 show the average particle bed temperature profiles for each set of operating parameters. The curves show that lower fill levels allowed for higher steady-state average bed temperatures. Lower fill

115

levels also resulted in the fastest heating rates, indicated by the larger slopes observed from 0 min to 30 min. Higher rotation rates increased the average bed temperature in every case except for the 10 % fill level with 2 rpm. Steady-state average bed temperatures and standard deviation between trials for each set of operating parameters are listed in Table 10.
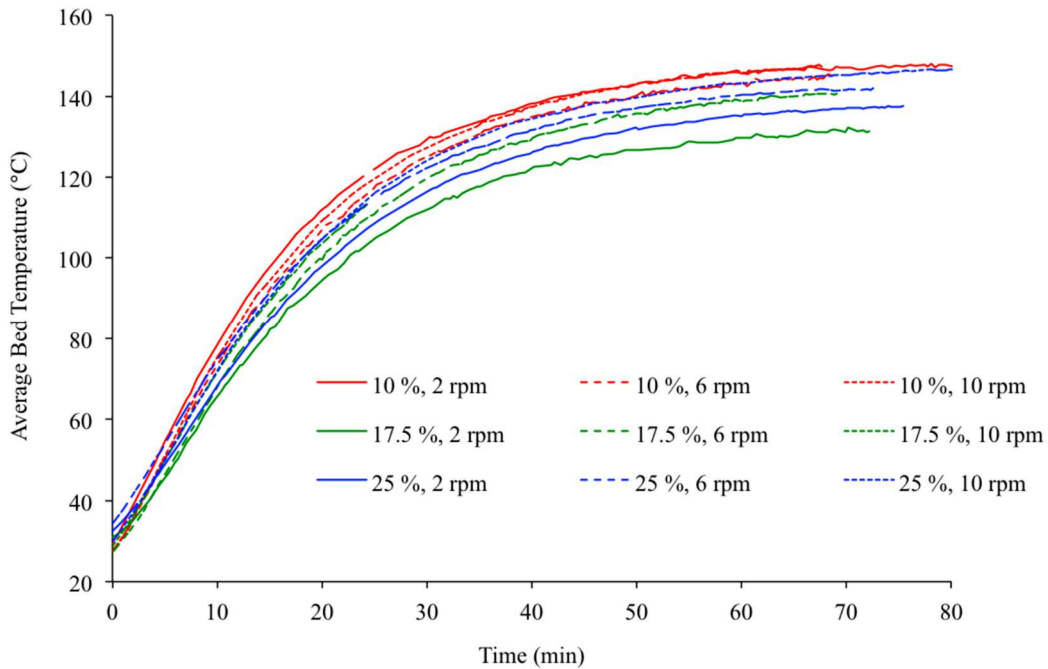
Figure 42. Average particle bed temperature profiles for each set of operating parameters.

Table 10. Steady-state Average Bed Temperatures and Standard Deviation Between Trials for Each Set of Operating Parameters. Temperatures Are Listed in Ascending Order.

Fill %, rpm	Steady-State Avg. Bed Temperature (°C)
25 %, 2 rpm	111 ± 2
17.5 %, 2 rpm	112 ± 2
25 %, 6 rpm	116 ± 1
10 %, 2 rpm	116 ± 5
17.5 %, 6 rpm	117 ± 1
10 %, 10 rpm	119 ± 2
17.5 %, 10 rpm	119 ± 1
25 %, 10 rpm	119 ± 2
10 %, 6 rpm	120 ± 3

The results show that decreasing the fill level and increasing the rotation rate result in higher steady-state average bed temperatures. With lower fill level, the particle bed is less massive. Therefore, applying the same energy input to a lower mass results in a higher temperature. As rotation rate increases, the number of particle-wall, particle-particle, and particle-fluid contacts increase. Heat energy in the system can only be transferred via these contacts, so increasing the number of contacts per unit time increases the heat transfer rate and consequently the steady-state average particle bed temperature.

These results support the findings by others in the literature. Emady et al. (2016) determined that increasing the rotation rate in the range of 0 – 10 rpm increased conductive heating performance in their simulations, as is observed in these experiments in the presence of conduction and convection. Additionally, lower fill levels exhibited

faster heating rates, as shown by Nguyen et al. (2014) in their simulations. Mellman (2001) suggested that operation in the rolling flow regime optimizes heating performance, which is observed in most cases in these experiments. Three of the four runs with the highest steady-state average bed temperature showed a rolling profile, but the run with the highest steady-state temperature (10 %, 6 rpm) is slumping. This discrepancy can be attributed to differences in the assumptions made to theorize the bed profile regimes and the reality of these experiments. The bed profiles described by Mellman (2001) are derived with the assumption that the drum wall is smooth. However, the experimental drum wall may not be perfectly smooth due to wear from friction between the drum wall and particles over time.

As fill level increases, the particle bed gains mass and volume, causing the rolling flow profile. Above fill levels of 10 %, bed stagnation is nearly impossible due to the large mass of particles present at the bed peak, causing them to roll down the top bed face. This bed motion profile generally results in an increased number of particle contacts and enhanced mixing within the bed. However, the presence of extra mass in the drum at high fill levels impedes the path to steady-state since the energy input is constant. Over a short operating range, a large bed mass should reach a smaller steady-state temperature than a smaller bed mass. With increasing rotation rate, more particles are forced along the drum wall to the bed peak per unit time, where they roll down the bed face and either mix into the bed or come in contact again with the drum wall and go around for another rotation. The particle bed core experiences an increased rate of agitation, allowing more mixing with the outer layer of particles. Therefore, increasing the rotation rate will

118

increase the steady-state bed temperature due to an increased number of particle-wall and particle-particle contacts.

6.5.3   Wall-Particle Heat Transfer Coefficient

Fig. 43 shows the average wall-particle heat transfer coefficient for each set of fill levels and rotation rates. For a constant fill level, increasing the rotation rate increased the heat transfer coefficient. This confirms the expectation that a rolling bed increases the heat transfer between the drum wall and particle bed by increasing the number of wall-particle and particle-particle contacts. The effect of fill level at a constant rotation rate is not as significant. Although there is less mass and therefore less resistance to heating the particle bed at lower fill levels, the hydrodynamics are impeded since the bed tends to the slumping or surging regime. At low fills levels, the effect of convection is also minimized. Convection has a larger impact on the heat transfer coefficient as the fill level increases, due to the larger surface area achieved with a larger particle bed. Not only is the exposed surface larger, but the total bed surface area also increases since the hot air penetrates the interstitial spaces between particles.

Fig. 44 shows the contour plot for wall-particle heat transfer coefficient for each fill level and rotation rate. This contour plot demonstrates the increasing impact of convection at higher fill levels for a constant rotation rate. The wall-particle heat transfer coefficient is maximized at 25 % fill level and 10 rpm because the surface area for heat

transfer is largest and the flow profile is rolling, maximizing the wall-particle and

particle- particle contacts.
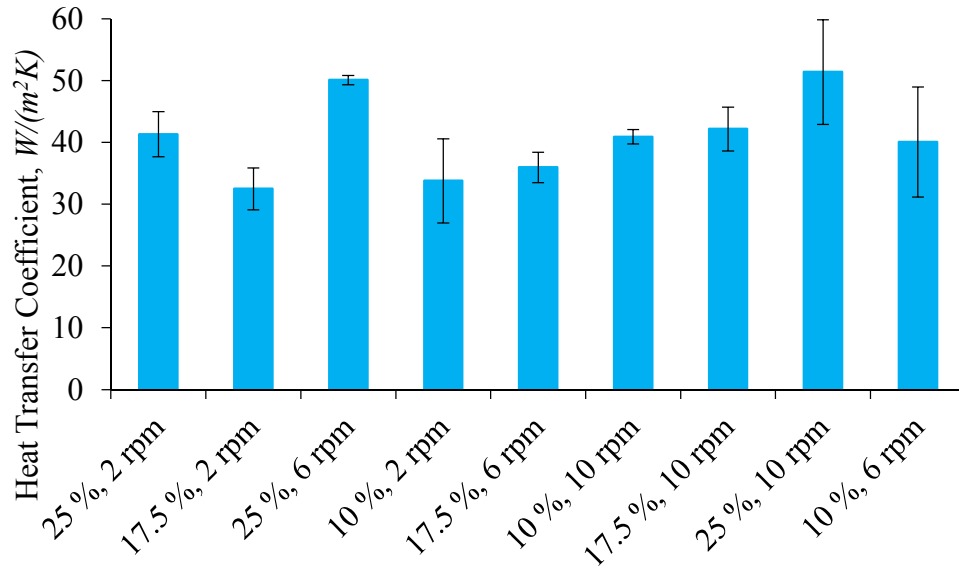
Figure 43. Average wall-to-particle heat transfer coefficient for all fill level and

rotation rate combinations studied. The error bars represent 95 % confidence intervals.
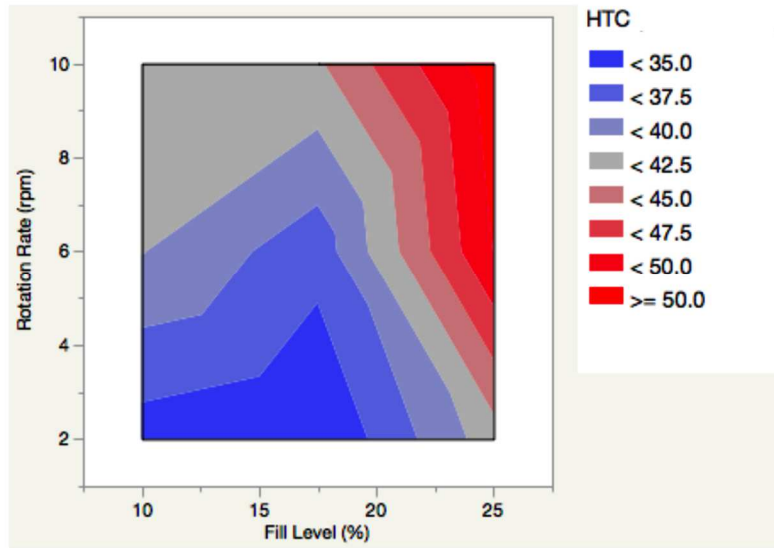
Figure 44. Contour plot of the average wall-particle heat transfer coefficient (HTC) as a function of fill level and rotation rate. HTC units are W/(m²K).

6.5.4 Fluid-Particle Heat Transfer Coefficient

The procedure outlined in Equations 1 and 2 is followed to calculate the fluid-particle heat transfer coefficient due to forced convection by the rotation of the drum wall in a closed system (Shi et al., 2008). The maximum value for h_f is 2.7 W/(m²K) at 10 rpm. This is close to the values found by Shi et al. (2008) and Debacq et al. (2011). A fluid-particle heat transfer coefficient of 2.7 W/(m²K) is more than an order of magnitude smaller than the wall-particle heat transfer coefficient in each case. This suggests that the heat loss is not driven by the forced convection due to the wall rotation, but rather by natural convection due to the temperature gradient between the air inside the drum and the air outside the drum. The Biot number calculated using Equation 3 shows that no temperature gradient exists within each particle. Using the maximum value for h_f of 2.7 W/(m²K), the Biot number is calculated to be less than 0.004. This is much less than one, indicating that internal conductive resistance is lower than external convective resistance, so each particle has a uniform temperature.

6.6 Conclusions

This research investigated the effects of fill level and rotation rate on the particle bed hydrodynamics, the wall-particle heat transfer, and the fluid-particle heat transfer using 3 mm silica beads in a stainless steel rotary drum. Experiments were carried out to understand the contributions of conduction and convection at fill levels of 10 %, 17.5 %,

and 25 %, and rotation rates of 2 rpm, 6 rpm, and 10 rpm. Heat guns were used for external and internal heating to introduce forced convection to the system. A qualitative analysis of the flow profile was done using the captured IR videos. The predicted flow profiles estimated using the experiments agreed with the theoretical flow profiles calculated using the the Froude number.The contributions of convection on the wall-particle heat transfer coefficient increased as the fill level increased due to the additional surface area available for particle-fluid contact. The results showed that decreasing the fill level and increasing the rotation rate resulted in higher steady-state average bed temperatures. The heat loss was not driven by the forced convection due to the wall rotation, but rather by natural convection due to the temperature gradient between the air inside the drum and the air outside the drum. Combing the flow profiles with the thermal profile of the bed, it can be concluded that a rolling bed increases the heat transfer between the drum wall and the particle bed by increasing the number of wall-particle and particle-particle contacts.

7   SUMMARY and CONCLUSIONS

The primary objective of this thesis was to investigate the hydrodynamics and heat transfer of silica beads using hopper bin and rotary drum process equipment.

Hopper bin experiments were conducted to study the segregation of bi-disperse silica beads. In addition, the effects of various process parameters were investigated.

- Two types of micro-glass beads with distinct size distributions were used to fill the hopper in two possible packing arrangements, i.e., well-mixed and layered configurations, with varying mass (particle number) ratios. For the well-mixed configuration, due to segregation effects, the fine particles clustered at the hopper bottom towards the end of the discharge. For the layered configuration, the coarse particles packed at the hopper bottom discharge first, opening a channel for the fine particles on the top.

- The effect of wall surface roughness on discharge rate was investigated. A 3D-printed hopper with ABSplus thermoplastic and a glass-blown borosilicate glass hopper were used for the wall roughness studies. It was found that discharge rate increased with increasing wall roughness. However, the effect of wall roughness had very minimal effect on discharge.

- The effect of particle surface roughness was investigated using 2.1 mm diameter silica beads. The discharge rate was estimated to be inversely proportional to (the root mean square roughness of the particle)$^{0.59}$.

A stainless steel rotary drum was used to investigate the effect of contact conduction heat transfer in silica beads. As heat transfer in rortary drums is a complex process, it is not easy to understand the process using experiments. Therefore, discrete element method (DEM) simulations were used for modelling and validated using experiments. The validated DEM model was used to investigate the effects of process parameters on heat transfer. In addition, a new temperature measurement technique was established using infrared (IR) thermography. The set-up was used to study the effects of process parameters.

- Simulations were performed to compare the performance of open-source (MFIX-DEM) and commercial code (EDEM) models with experimental data. The wall to particle heat transfer in a rotary drum was investigated using alumina particles. The thermal time constant, τ, was calculated to quantitatively compare the performance of the two DEM models. The value of τ was 175.4 s for the experiment, 185.2 s for the MFIX-DEM simulation, and 158.7 s for EDEM simulation. Even though there was a discrepancy in τ, in general, there was a good agreement between the simulaion and experimental results.

- MFIX-DEM simulations were performed to study the effect of particle size distribution (PSD) on heat transfer. Three different distributions with the same mean (0.4 cm) and standard deviation (0.035 cm) were used. It was found that the three size distributions contributed up to approximately 2 % deviation in the observed heat transfer coefficient. Another study to determine the effect of distribution pattern was done using three distributions of the same mean (0.4 cm), but different standard deviations (0, 0.03, and 0.07 cm for homogeneous, narrow, and broad distributions, respectively). It was found that monodispersed particle beds exhibit better heat transfer when compared to polydispersed beds. With a narrow distribution, a better heat transfer rate was achieved than with a broad distribution, as the particles behave more similarly to a homogeneous bed.

- EDEM simulations were performed at rolling frictions of 0, 0.005, 0.01, and 0.1. It was seen that at lower values of rolling friction, particle circulation in the bed was enhanced and therefore better heat transfer was achieved.

- A lab-scale rotary drum was constructed to conduct heat transfer experiments. The set-up was built in such a way that it could handle up to 1000 ˚C, suitable to perform high temperature experiments. The drum in the experimental setup consisted of a 6" ID stainless steel cylinder with 0.5" thickness. One side of the drum was closed using a 6" OD and 6 mm thick sapphire glass, specifically chosen to give a high transmittance to IR light, with a transmission range from 0.17 μm to 5.5 μm. The

sapphire glass was held in place using a 5.7" ID and 11" OD titanium ring with 0.5" thickness. The other side of the drum was closed using a 6.5" OD and 6 mm thick quartz glass specifically chosen to handle high temperatures (up to 1200 °C). Like the sapphire glass, the quartz glass was also held in place using a 6" ID and 11" OD titanium ring with 0.5" thickness. The drum rotated on the two 11" OD titanium wheels using rollers with variable rotational speed from 0.5 – 14 rpm.

• An IR camera was used to record images to give instantaneous thermal data of particles inside a rotary drum. The calibration procedure and the methodology used to extract the bulk average temperatures of the particle bed and the drum wall from the IR camera was discussed. The technique provides insightful information on the flow regimes and heat transfer.

• Experiments were performed using IR thermography. 3 mm silica beads inside a stainless-steel rotary drum were used at fill levels ranging from 10 – 25 % and rotation rates from 2 – 10 rpm. The effects of fill level and rotation speed on conduction heat transfer were investigated. Higher rotation rates resulted in maximum steadystate average bed temperatures, whereas fill level did not have a conclusive effect.

- Experiments were performed to understand conduction with forced convection. Particle-particle friction caused the particle bed to stagnate at elevated temperatures in conduction, while the inlet air velocity in convection dominated the particle friction effects to maintain the flow profile. The maximum heat transfer coefficient was achieved at a high rotation rate and low fill level in conduction, and at a high rotation rate and high fill level in convection.

Conduction and convection exhibited the same flow profile, but in conduction the particle bed stagnated as the particles heated and particle-particle friction increased. The contributions of convection on the wall-particle heat transfer coefficient increased as the fill level increased due to the additional surface area available for particle-fluid contact. Fluid-particle forced convection was found to be negligible in the closed system, suggesting that heat loss from the system was dominated by natural convection due to the temperature gradient between the drum contents and the external environment. These findings provide a new method for studying the heat transfer in rotary drum systems and contribute to increasing operating efficiencies and energy savings on a global scale.

8   RECOMMENDATIONS FOR FUTURE WORK

- The effect of particle surface roughness using different sized silica beads should be studied.

- Images captured using the infrared (IR) camera can be converted to RGB images and the particle image velocimetry (PIV) technique can be used to calculate the velocity vectors in order to quantitatively verify the particle bed flow profile. The PIV can be combined with IR thermography to obtain combined quantitative (i.e., hydrodynamic and thermal) data sets. The combined technique will provide insightful information on the heat transfer.

- Additional experiments should be done studying forced convection at varying inlet air temperatures and flow rates. Studying materials other than silica at varying particle size distributions would provide more knowledge of the flow profile transitions at elevated temperatures.

- To better understand the heat transfer mechanisms in the rotary drum system, shorter experiments should be run while recording at a higher frame rate to quantify localized wall-particle and particle-particle heat fluxes.

- The present experimental set-up must be further developed to incorporate an induction coil around the drum in order to quickly heat the drum above 600 ˚C, so that the radiation heat transfer mechanism can be studied. Further, the set-up can be used to understand the effects of process parameters like rotation speed, fill level, and particle size on radiation heat transfer.

- A series of experiments incorporating each mode of heat transfer (conduction, convection, and radiation) should be carried out in a rotary drum. The experiments must aim at recording, while the solids flow, the temperature profiles of the freeboard gas, the solid particle bulk and the wall, as well as the power supplied for heating, over a range of operating conditions. Based on the data, the experimental wall-to-solid heat transfer coefficient can be determined through an energy balance.

- A model based on dimensional analysis should be proposed to calculate the wall-to-solid heat transfer coefficient for low to high heating temperatures (100 – > 500 °C). The experimental and calculated theoretical results can be compared to estimate the heat lost through the system. The calculated heat losses can be used to develop an understanding of the discrepancy observed in Chapter 4 while validating the conduction heat transfer mechanism.

REFERENCES

Ahn, H., Başaranoğlu, Z., Yilmaz, M., Buğutekin, A., Gül, M.Z., 2008. Experimental investigation of granular flow through an orifice. Powder Technol. 186, 65–71. https://doi.org/10.1016/j.powtec.2007.11.001

Anand, A., Curtis, J.S., Wassgren, C.R., Hancock, B.C., Ketterhagen, W.R., 2008. Predicting discharge dynamics from a rectangular hopper using the discrete element method (DEM). Chem. Eng. Sci. 63, 5821–5830. https://doi.org/10.1016/j.ces.2008.08.015

Arteaga, P., Tüzün, U., 1990. Flow of binary mixtures of equal-density granules in hoppers-size segregation, flowing density and discharge rates. Chem. Eng. Sci. https://doi.org/10.1016/0009-2509(90)87093-8

Austin, L.G., Shoji, K., Hogg, R., Carlson, J., Flemmer, R.L.C., 1978. Flow rates of dry powders in inclinded rotating cylinders under open-ended discharge conditions. Powder Technol. 20, 219–225. https://doi.org/10.1016/0032-5910(78)80052-7

Batchelor, G.K., O'Brien, R.W., 1977. Thermal or Electrical Conduction Through a Granular Material. Proc. R. Soc. A Math. Phys. Eng. Sci. 355, 313–333. https://doi.org/10.1098/rspa.1977.0100

Beckman, J.R., Campagnolo, J.F., Kratzke, K., 1998. Rotating Drum Heat Exchanger. Chem. Eng. Commun. 168, 1–11. https://doi.org/10.1080/00986449808912704

BJ, E., J, G., R, D., 1994. The Legacy of Neglect in the United-States. Chem. Eng. Prog. 90, 32–43.

Boateng, A.A., Barr, P. V., A. A, Boateng., P. V, B., 1996. A thermal model for the rotary kiln including heat transfer within the bed. Int. J. Heat Mass Transf. 39, 2131–2147. https://doi.org/10.1016/0017-9310(95)00272-3

Bongo Njeng, A.S., Vitu, S., Clausse, M., Dirion, J.-L., Debacq, M., 2018. Wall-to-solid heat transfer coefficient in flighted rotary kilns: Experimental determination and modeling. Exp. Therm. Fluid Sci. 91, 197–213. https://doi.org/10.1016/J.EXPTHERMFLUSCI.2017.10.024

Bui, R.T., Simard, G., Charette, A., Kocaefe, Y., Perron, J., 1995. Mathematical modeling of the rotary coke calcining kiln. Can. J. Chem. Eng. 73, 534–545. https://doi.org/10.1002/cjce.5450730414

Chatterjee, A., Sathe, A. V., Srivastava, M.P., Mukhopadhyay, P.K., 1983. Flow of

materials in rotary kilns used for sponge iron manufacture: Part I. Effect of some operational variables. Metall. Trans. B 14, 375–381. https://doi.org/10.1007/BF02654356

Chaudhuri, B., Muzzio, F.J., Tomassone, M.S., 2010. Experimentally validated computations of heat transfer in granular materials in rotary calciners. Powder Technol. 198, 6–15. https://doi.org/10.1016/j.powtec.2009.09.024

Chaudhuri, B., Muzzio, F.J., Tomassone, M.S., 2006. Modeling of heat transfer in granular flow in rotating vessels. Chem. Eng. Sci. 61, 6348–6360. https://doi.org/10.1016/j.ces.2006.05.034

Chen, S., Adepu, M., Emady, H., Jiao, Y., Gel, A., 2017. Enhancing the physical modeling capability of open-source MFIX-DEM software for handling particle size polydispersity: Implementation and validation. Powder Technol. 317, 117–125. https://doi.org/10.1016/j.powtec.2017.04.055

Das Gupta, S., Khakhar, D. V., Bhatia, S.K., 1991. Axial transport of granular solids in horizontal rotating cylinders. Part 1: Theory. Powder Technol. 67, 145–151. https://doi.org/10.1016/0032-5910(91)80151-8

de Silva, S.R., Dyrøy, A., Enstad, G.G., 2000. Segregation Mechanisms and Their Quantification Using Segregation Testers. Springer, Dordrecht, pp. 11–29. https://doi.org/10.1007/978-94-015-9498-1_2

DeWitt, D.P., Nutter, G.D. (Eds.), 1988. Theory and Practice of Radiation Thermometry, Theory and Practice of Radiation Thermometry. John Wiley & Sons, Inc., Hoboken, NJ, USA. https://doi.org/10.1002/9780470172575

Dhanjal, S.K., Barr, P. V., Watkinson, a. P., 2004. The rotary kiln: An investigation of bed heat transfer in the transverse plane. Metall. Mater. Trans. B 35, 1059–1070. https://doi.org/10.1007/s11663-004-0062-0

Dietiker, J.F., 2013. Documentation of open-source MFIX – DEM software for gas-solids. Géotechnique 29, 47–65.

Ding, Y.L., Forster, R., Seville, J.P.K., Parker, D.J., 2002. Segregation of granular flow in the transverse plane of a rolling mode rotating drum. Int. J. Multiph. Flow 28, 635–663.

Ding, Y.L., Forster, R.N., Seville, J.P.K., Parker, D.J., 2001. Some aspects of heat transfer in rolling mode rotating drums operated at low to medium temperatures. Powder Technol. 121, 168–181. https://doi.org/10.1016/S0032-5910(01)00343-6

Emady, H.N., Anderson, K. V., Borghard, W.G., Muzzio, F.J., Glasser, B.J., Cuitino, A., 2016. Prediction of conductive heating time scales of particles in a rotary drum. Chem. Eng. Sci. 152, 45–54. https://doi.org/10.1016/j.ces.2016.05.022

Enstad, G., 1975. On the theory of arching in mass flow hoppers. Chem. Eng. Sci. https://doi.org/10.1016/0009-2509(75)85051-2

Figueroa, I., Vargas, W.L., Ã, J.J.M., 2010. Mixing and heat conduction in rotating tumblers. Chem. Eng. Sci. 65, 1045–1054. https://doi.org/10.1016/j.ces.2009.09.058

Frankowski, P., Morgeneyer, M., 2013. Calibration and validation of DEM rolling and sliding friction coefficients in angle of repose and shear measurements, in: AIP Conference Proceedings. pp. 851–854. https://doi.org/10.1063/1.4812065

Georgallis, M., Nowak, P., Salcudean, M., Gartshore, I.S., 2002. Mathematical modelling of lime kilns. Pulp Pap. Canada 103, 44–47.

Govender, I., 2016. Granular flows in rotating drums: A rheological perspective. Miner. Eng. 92, 168–175. https://doi.org/10.1016/j.mineng.2016.03.021

Grajales, L.M., Xavier, N.M., Henrique, J.P., Thoméo, J.C., 2012. Mixing and motion of rice particles in a rotating drum. Powder Technol. https://doi.org/10.1016/j.powtec.2012.02.028

Gui;, N., Ji, J.G.Z., Gui, N., Gao, J., Ji, Z., 2013. Numerical Study of Mixing and Thermal Conduction of Granular Particles in Rotating Tumblers. AIChE J. 59, 1906–1918. https://doi.org/10.1002/aic

Gui, N., Yan, J., Xu, W., Ge, L., Wu, D., Ji, Z., Gao, J., Jiang, S., Yang, X., 2013. DEM simulation and analysis of particle mixing and heat conduction in a rotating drum. Chem. Eng. Sci. 97, 225–234. https://doi.org/10.1016/j.ces.2013.04.005

Herz, F., Mitov, I., Specht, E., Stanev, R., 2012a. Experimental study of the contact heat transfer coefficient between the covered wall and solid bed in rotary drums. Chem. Eng. Sci. 82, 312–318. https://doi.org/10.1016/j.ces.2012.07.042

Herz, F., Mitov, I., Specht, E., Stanev, R., 2012b. Experimental study of the contact heat transfer coefficient between the covered wall and solid bed in rotary drums. Chem. Eng. Sci. https://doi.org/10.1016/j.ces.2012.07.042

Huang, J., da Silva, M.V., Krabbenhoft, K., 2013. Three-dimensional granular contact dynamics with rolling resistance. Comput. Geotech. 49, 289–298. https://doi.org/10.1016/j.compgeo.2012.08.007

Iwan Harsono, 2009. Heat Transfer Mechanisms in an Indirectly Heated Rotary Kiln with Lifters and Its Role in Scaling. PhD Thesis Curtin University of Technology.

Jenike, A.W., 1967. Quantitative design of mass-flow bins. Powder Technol. https://doi.org/10.1016/0032-5910(67)80042-1

Jiang, M., Zhao, Y., Liu, G., Zheng, J., 2011. Enhancing mixing of particles by baffles in a rotating drum mixer. Particuology 9, 270–278.

Jolliffe, I.G., Newton, J.M., 1983a. The effect of dosator nozzle wall texture on capsule filling with the mG2 simulator. J. Pharm. Pharmacol. https://doi.org/10.1111/j.2042-7158.1983.tb04253.x

Jolliffe, I.G., Newton, J.M., 1983b. Capsule filling studies using an mG2 production machine. J. Pharm. Pharmacol. https://doi.org/10.1111/j.2042-7158.1983.tb04273.x

Jolliffe, I.G., Newton, J.M., 1982. Practical implications of theoretical consideration of capsule filling by the dosator nozzle system. J. Pharm. Pharmacol. https://doi.org/10.1111/j.2042-7158.1982.tb04710.x

Kawecki, W., Kurcyusz, E., Manitius, A., 1974. Mathematical Model of the Aluminum Oxide Rotary Kiln. Ind. Eng. Chem. Process Des. Dev. 13, 132–142. https://doi.org/10.1021@i260050a007

Ketterhagen, W.R., Curtis, J.S., Wassgren, C.R., Kong, A., Narayan, P.J., Hancock, B.C., 2007. Granular segregation in discharging cylindrical hoppers : A discrete element and experimental study. Chem. Eng. Sci. 62, 6423–6439. https://doi.org/10.1016/j.ces.2007.07.052

Komossa, H., Wirtz, S., Scherer, V., Herz, F., Specht, E., 2015. Heat transfer in indirect heated rotary drums filled with monodisperse spheres: Comparison of experiments with DEM simulations. Powder Technol. 286, 722–731. https://doi.org/10.1016/j.powtec.2015.07.022

Kramers, H., Croockewit, P., 1952. The passage of granular solids through inclined rotary kilns. Chem. Eng. Sci. 1, 259–265. https://doi.org/10.1016/0009-2509(52)87019-8

Kwapinska, M., Saage, G., Tsotsas, E., 2008. Continuous versus discrete modelling of heat transfer to agitated beds. Powder Technol. 181, 331–342. https://doi.org/10.1016/J.POWTEC.2007.05.025

Kwapinska, M., Saage, G., Tsotsas, E., 2006. Mixing of particles in rotary drums : A comparison of discrete element simulations with experimental results and

penetration models for thermal processes 161, 69–78.
https://doi.org/10.1016/j.powtec.2005.08.038

Lamarche, C.Q., Liu, P., Kellogg, K.M., Hrenya, C.M., 2017. Fluidized-bed
measurements of carefully-characterized, mildly-cohesive (Group A) particles.
https://doi.org/10.1016/j.cej.2016.10.119

Landry, J.W., Grest, G.S., 2005. Jamming in granular hopper flow. arXiv Prepr. cond-
mat/0506110 5.

Le Guen, L., Huchet, F., Dumoulin, J., Baudru, Y., Tamagny, P., 2013. Convective heat
transfer analysis in aggregates rotary drum reactor. Appl. Therm. Eng. 54, 131–139.
https://doi.org/10.1016/j.applthermaleng.2013.01.025

Lebas, E., Hanrot, F., Ablitzer, D., Houzelot, J. □L, 1995. Experimental study of
residence time, particle movement and bed depth profile in rotary kilns. Can. J.
Chem. Eng. 73, 173–180. https://doi.org/10.1002/cjce.5450730202

Lehmberg, J., Hehl, M., Schügerl, K., 1977. Transverse mixing and heat transfer in
horizontal rotary drum reactors. Powder Technol. 18, 149–163.
https://doi.org/10.1016/0032-5910(77)80004-1

Liu, H., Yin, H., Zhang, M., Xie, M., Xi, X., 2016. Numerical simulation of particle
motion and heat transfer in a rotary kiln. Powder Technol. 287, 239–247.
https://doi.org/10.1016/j.powtec.2015.10.007

Liu, X., Gong, J., Zhang, Z., Wu, W., 2016. An image analysis technique for the particle
mixing and heat transfer process in a pan coater. Powder Technol. 295, 161–166.
https://doi.org/10.1016/j.powtec.2016.03.029

Liu, X.Y., Specht, E., 2010. Temperature distribution within the moving bed of rotary
kilns: Measurement and analysis. Chem. Eng. Process. Process Intensif. 49, 147–
150. https://doi.org/10.1016/j.cep.2010.01.008

Lybaert, P., 1987. Wall-particles heat transfer in rotating heat exchangers. Int. J. Heat
Mass Transf. 30, 1663–1672. https://doi.org/10.1016/0017-9310(87)90312-7

Makse, H.A., 1999. Continuous Avalanche Segregation of Granular Mixtures in Thin
Rotating Drums. Phys. Rev. Lett. 83, 3186–3189.
https://doi.org/10.1103/PhysRevLett.83.3186

Martins, M.A., Oliveira, L.S., Franca, A.S., 2001. Modeling and simulation of petroleum
coke calcination in rotary kilns. Fuel 80, 1611–1622. https://doi.org/10.1016/S0016-
2361(01)00032-1

McGlinchey, D., 2009. Characterisation of Bulk Solids, Characterisation of Bulk Solids. https://doi.org/10.1002/9781444305456

Mellmann, J., 2001. The transverse motion of solids in rotating cylinders-forms of motion and transition behavior. Powder Technol. 118, 251–270. https://doi.org/10.1016/S0032-5910(00)00402-2

Mesnier, A., Rouabah, ;, Cogné, ;, Peczalski, ;, Vessot-Crastes, ;, Vacus, ;, Andrieu, ;, 2018. Mechanical and thermal segregation of milli-beads during contact heating in a rotary drum. DEM modeling and simulation 11–14. https://doi.org/10.4995/ids2018.2018.7423

Meyer, J., Fuchs, R., Staedler, T., Jiang, X., 2014. Effect of surface roughness on sliding friction of micron-sized glass beads. Friction 2, 255–263. https://doi.org/10.1007/s40544-014-0045-3

Meyers, M.A., 2001. Plasticity: Adiabatic Shear Localization, in: Encyclopedia of Materials: Science and Technology. https://doi.org/10.1016/b0-08-043152-6/01257-2

Miller C.O., Smith B.A, Schuette, 1942. Factor influencing the operation of rotary dryers. Trans AIChE 38, 841.

Mohseni, M., Peters, B., 2016. Effects of particle size distribution on drying characteristics in a drum by XDEM: A case study. Chem. Eng. Sci. 152. https://doi.org/10.1016/j.ces.2016.07.004

Morris, A.B., Pannala, S., Ma, Z., Hrenya, C.M., 2015. A conductive heat transfer model for particle flows over immersed surfaces. Int. J. Heat Mass Transf. 89, 1277–1289. https://doi.org/10.1016/j.ijheatmasstransfer.2015.06.004

Musser, J.M.H., 2011. Modeling of Heat Transfer and Reactive Chemistry for Particles in Gas-Solid Flow Utilizing Continuum-Discrete Methodology (CDM). PhD Thesis West Virginia University.

Nafsun, A.I., Herz, F., Liu, X., 2018. Influence of material thermal properties and dispersity on thermal bed mixing in rotary drums. Powder Technol. 331, 121–128. https://doi.org/10.1016/j.powtec.2018.01.072

Nafsun, A.I., Herz, F., Specht, E., Komossa, H., Wirtz, S., Scherer, V., Liu, X., 2017. Thermal bed mixing in rotary drums for different operational parameters. Chem. Eng. Sci. 160, 346–353. https://doi.org/10.1016/j.ces.2016.11.005

Nafsun, A.I., Herz, F., Specht, E., Scherer, V., Wirtz, S., 2016. Heat Transfer

Experiments in a Rotary Drum for a Variety of Granular Materials. Exp. Heat Transf. 29, 520–535. https://doi.org/10.1080/08916152.2015.1036180

Nguyen, H.T., Cosson, B., Lacrampe, M.F., Krawczak, P., 2015. Numerical simulation on the flow and heat transfer of polymer powder in rotational molding. Int. J. Mater. Form. 8, 423–438. https://doi.org/10.1007/s12289-014-1185-8

Ortiz, O.A., Suárez, G.I., Nelson, A., 2005. Dynamic simulation of a pilot rotary kiln for charcoal activation. Comput. Chem. Eng. 29, 1837–1848. https://doi.org/10.1016/j.compchemeng.2005.03.005

Patil, A. V, Peters, E.A.J.F., Sutkar, V.S., Deen, N.G., Kuipers, J.A.M., 2015. A study of heat transfer in fluidized beds using an integrated DIA/PIV/IR technique. Chem. Eng. J. 259, 90–106. https://doi.org/10.1016/j.cej.2014.07.107

Peray, kurt E., Waddell, J.J., 1986. the Rotary Cement Kiln. Chem. Publ. Co. 1–5. https://doi.org/10.1007/s13398-014-0173-7.2

Piton, M., Huchet, F., Le Corre, O., Edan Le Guen, L., Cazacliu, B., Le Guen, L., Cazacliu, B., 2015. A coupled thermal-granular model in flights rotary kiln: Industrial validation and process design. Appl. Therm. Eng. 75, 1011–1021. https://doi.org/10.1016/j.applthermaleng.2014.10.052

Pohlman, N.A., Severson, B.L., Ottino, J.M., Lueptow, R.M., 2006. Surface roughness effects in granular matter: Influence on angle of repose and the absence of segregation. Phys. Rev. E - Stat. Nonlinear, Soft Matter Phys. https://doi.org/10.1103/PhysRevE.73.031304

Richard, P., Nicodemi, M., Delannay, R., Ribière, P., Bideau, D., 2005. Slow relaxation and compaction of granular systems. Nat. Mater. 4, 121–128. https://doi.org/10.1038/nmat1300

Rovaglio, M., Manca, D., Biardi, G., 1998. Dynamic modeling of waste incineration plants with rotary kilns. Chem. Eng. Sci. 53, 2727–2742. https://doi.org/10.1016/S0009-2509(98)00081-5

Sagastume Gutirrez, A., Cogollos Martnez, J.B., Vandecasteele, C., 2013. Energy and exergy assessments of a lime shaft kiln. Appl. Therm. Eng. https://doi.org/10.1016/j.applthermaleng.2012.07.013

Saleh, K., Golshan, S., Zarghami, R., 2018. A review on gravity flow of free-flowing granular solids in silos – Basics and practical aspects. Chem. Eng. Sci. https://doi.org/10.1016/j.ces.2018.08.028

Samadani, A., Pradhan, A., Kudrolli, A., 2000. Visualization of Segregation in Granular Flows Inside Silos. Springer, Dordrecht, pp. 53–60. https://doi.org/10.1007/978-94-015-9498-1_4

Santos, D.A., Dadalto, F.O., Scatena, R., Duarte, C.R., Barrozo, M.A.S., 2015. A hydrodynamic analysis of a rotating drum operating in the rolling regime. Chem. Eng. Res. Des. 94, 204–212. https://doi.org/10.1016/j.cherd.2014.07.028

Savage, S.B., Lun, C.K.K., 1988. Particle size segregation in inclined chute flow of dry cohesionless granular solids. J. Fluid Mech. https://doi.org/10.1017/S002211208800103X

Schliinder, E.U., n.d. Heat Transfer to Packed and Stirred Beds from the Surface of Immersed Bodies Wkmeiibergang zwischen ruhenden und mechanisch durchmischten Schiittgiitern und darin eingebetteten Heizfkhen.

Schlünder, E.-U., Mollekopf, N., 1984. Vacuum contact drying of free flowing mechanically agitated particulate material. Chem. Eng. Process. Process Intensif. 18, 93–111. https://doi.org/10.1016/0255-2701(84)85012-6

Schmid, P.J., 2011. Application of the dynamic mode decomposition to experimental data, in: Experiments in Fluids. https://doi.org/10.1007/s00348-010-0911-3

Shi, D., Vargas, W.L., McCarthy, J.J., 2008. Heat transfer in rotary kilns with interstitial gases. Chem. Eng. Sci. 63, 4506–4516. https://doi.org/10.1016/j.ces.2008.06.006

Sleppy, J.A., Puri, V.M., 1996. Size-segregation of granulated sugar during flow. Trans. Am. Soc. Agric. Eng. https://doi.org/10.13031/2013.27636

Standish, N., Kilic, A., 1985. Comparison of stop—start and continuous sampling methods of studying segregation of materials discharging from a hopper. Chem. Eng. Sci. 40, 2152–2153. https://doi.org/10.1016/0009-2509(85)87036-6

Suiker, A.S.J., Fleck, N.A., 2004. Frictional collapse of granular assemblies. J. Appl. Mech. Trans. ASME 71, 350–358. https://doi.org/10.1115/1.1753266

Syamlal, M., 1998. MFIX documentation numerical technique. Tech. Note DOE/MC31346-5824, NTIS/DE98002029, Natl. Energy Technol. Lab. Dep. Energy 5824, DE-AC21-95MC31346.

Syed, Z., Tekeste, M., White, D., 2017a. A coupled sliding and rolling friction model for DEM calibration. J. Terramechanics 72, 9–20. https://doi.org/10.1016/J.JTERRA.2017.03.003

Syed, Z., Tekeste, M., White, D., 2017b. A coupled sliding and rolling friction model for DEM calibration. J. Terramechanics 72, 9–20. https://doi.org/10.1016/j.jterra.2017.03.003

Thammavong, P., Debacq, M., Vitu, S., Dupoizat, M., 2011. Experimental Apparatus for Studying Heat Transfer in Externally Heated Rotary Kilns. Chem. Eng. Technol. 34, 707–717. https://doi.org/10.1002/ceat.201000391

To, K., Lai, P.Y., Pak, H.K., 2001. Jamming of granular flow in a two-dimensional hopper. Phys. Rev. Lett. 86, 71–74. https://doi.org/10.1103/PhysRevLett.86.71

Tscheng, S.H., Watkinson, A.P., 1979. Convective heat transfer in a rotary kiln. Can. J. Chem. Eng. 57, 433–443. https://doi.org/10.1002/cjce.5450570405

Tsotsas, E., 2019. Particle-particle heat transfer in thermal DEM: Three competing models and a new equation. Int. J. Heat Mass Transf. 132, 939–943. https://doi.org/10.1016/J.IJHEATMASSTRANSFER.2018.12.090

Tüzün, U., Arteaga, P., 1992. A microstructural model of flowing ternary mixtures of equal-density granules in hoppers. Chem. Eng. Sci. https://doi.org/10.1016/0009-2509(92)85010-9

Vàhl, L., Kingma, W.G., 1952. Transport of solids through horizontal rotary cylinders. Chem. Eng. Sci. 1, 253–258. https://doi.org/10.1016/0009-2509(52)87018-6

Van Belle, L., Van Rompay, S., Uddin, M.H., Ozalp, N., Vleugels, J., 2018. DESIGN AND EXPERIMENTAL TESTING OF A CARBON FEEDER FOR A SOLAR THERMAL RECEIVER. Begell House, pp. 763–777. https://doi.org/10.1615/tfec2018.env.024512

Vargas, W.L., McCarthy, J.J., 2001. Heat Conduction in Granular Materials. AIChE 47, 1052–1059.

Vaziri Hassas, B., Caliskan, H., Guven, O., Karakas, F., Cinar, M., Celik, M.S., 2016. Effect of roughness and shape factor on flotation characteristics of glass beads. Colloids Surfaces A Physicochem. Eng. Asp. 492, 88–99. https://doi.org/10.1016/j.colsurfa.2015.12.025

Venkataraman, K.S., Fuerstenau, D.W., 1986. Effect of lifter shape and configuration on material transport part I: In rotating drums. Powder Technol. 46, 23–32. https://doi.org/10.1016/0032-5910(86)80095-X

Wensrich, C.M., Katterfeld, A., 2012. Rolling friction as a technique for modelling particle shape in DEM. Powder Technol. 217, 409–417.

https://doi.org/10.1016/J.POWTEC.2011.10.057

Wes, G.W.J., Drinkenburg, A.A.H., Stemerding, S., 1976. Heat transfer in a horizontal rotary drum reactor. Powder Technol. 13, 185–192. https://doi.org/10.1016/0032-5910(76)85003-6

Williams, J.C., 1977. The rate of discharge of coarse granular materials from conical mass flow hoppers. Chem. Eng. Sci. https://doi.org/10.1016/0009-2509(77)80202-9

Xie, Q., Chen, Z., Hou, Q., Yu, A.B., Yang, R., 2017. DEM investigation of heat transfer in a drum mixer with lifters. Powder Technol. 314, 175–181. https://doi.org/10.1016/j.powtec.2016.09.022

Xu, T., Torres, P.D., Beck, L.W., Haw, J.F., 1984. Catalyst prepartion by impregnation and activity distribution. Chem. Eng. Sci. 39, 859–864.

Yang, W.J., Zhou, Z.Y., Yu, A.B., 2015. Particle scale studies of heat transfer in a moving bed. Powder Technol. 281, 99–111. https://doi.org/10.1016/j.powtec.2015.04.071

Yazdani, E., Hashemabadi, S.H., 2019. DEM simulation of heat transfer of binary-sized particles in a horizontal rotating drum. Granul. Matter 21, 6. https://doi.org/10.1007/s10035-018-0857-3

Yohannes, B., Emady, H., Anderson, K., Paredes, I., Javed, M., Borghard, W., Muzzio, F.J., Glasser, B.J., Cuitino, A.M., 2016. Scaling of heat transfer and temperature distribution in granular flows in rotating drums. Phys. Rev. E - Stat. Nonlinear, Soft Matter Phys. 94. https://doi.org/10.1103/PhysRevE.94.042902

Zhang, Z., Liu, Y., Zhao, X., Xiao, Y., Lei, X., 2019. Mixing and Heat Transfer of Granular Materials in an Externally Heated Rotary Kiln. Chem. Eng. Technol. 42, 987–995. https://doi.org/10.1002/ceat.201800232

Zhu, H.P., Zhou, Z.Y., Yang, R.Y., Yu, A.B., 2008. Discrete particle simulation of particulate systems: A review of major applications and findings. Chem. Eng. Sci. https://doi.org/10.1016/j.ces.2008.08.006

Zygo Corporation, 2014. Optical Profilers - How Optical Profilers Work [WWW Document]. Zygo Metrol. Bus. Segm. URL https://www.zygo.com/?/met/profilers/opticalprofilersabout.htm

APPENDIX A

SCHEMATIC OF OPTICAL PROFILOMETER WORKING PRINCIPLE
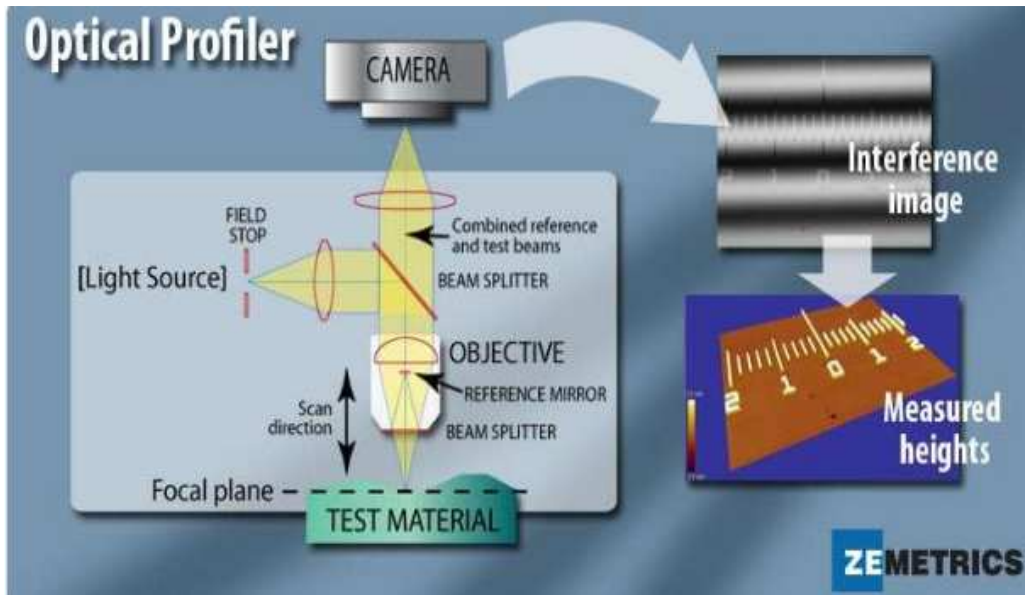
Figure A 1 Image of a profilometer working principle (Zygo).

APPENDIX B

CALCULATING e_s

The fraction of the drum wall touched by particles, e_s, was calculated using ImageJ software. Images of the particle bed were analyzed at each fill level and rotation rate to determine e_s for each fill level. Figure A2 shows an example of this procedure.
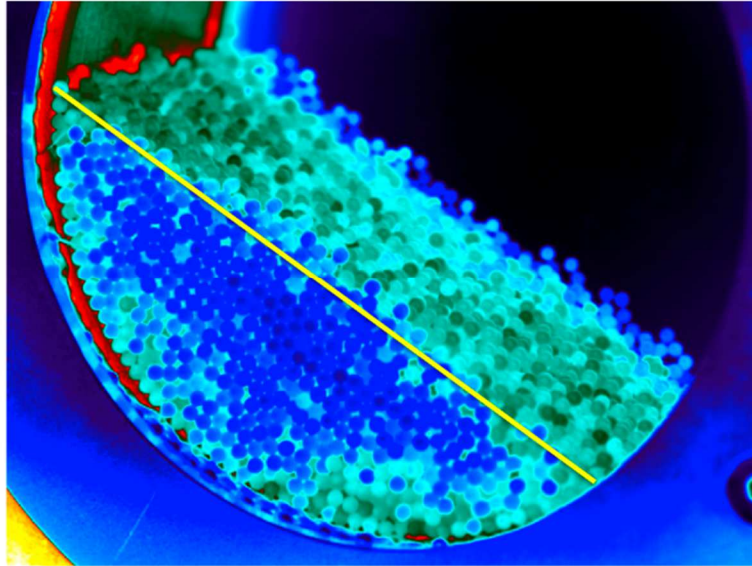
Figure A 2 Image of a 25 % fill level, 10 rpm run used to determine e_s.

The yellow line in Fig. A2 was drawn in ImageJ software to determine the length of the chord, C, intersecting the circle. The scale was set on the image by selecting the diameter of a particle and setting its length to 3 mm. With the length of the chord known, the arc length of the portion of the wall touched by particles was calculated. The fraction of the drum wall touched by particles is the arc length divided by the drum circumference, D. After simplification, the relationship between C and e_s reduces to Equation A1. The e_s values found for each fill level were: 0.19 for 10 % fill, 0.25 for 17.5 % fill, and 0.28 for 25 % fill.

$$e_s = \frac{1}{\pi} sin^{-1} \frac{C}{D} \tag{A1}$$

APPENDIX C

MATLAB SCRIPT FOR CALCULATING THE HEAT TRANSFER COEFFICIENT

```matlab
%-----------------------------------------------------------------%
%          Variables exported from the Camera                     %
%          WHAT:                    NAME:             %
%          Frames                   F                %
%          Real Time               time              %
%          Wall temperature         W_Temp            %
%          Particles average temperature    P_avgTemp         %
%-----------------------------------------------------------------%
clear ; clc;
datestr(clock, 0)
z=cputime;
%------------------------ INPUTS --------------------------------------%
filename = 'filename.xlsx'; % create the file location for data
Prompt1 = 'What is the fill level?';
FillLevel = input(Prompt1); % fill level of the drum
%-----------------------------------------------------------------------%
PI = 3.14159265;
L = 0.0762 ; % drum length, m
A  = pi*0.1524; % drum circumference, m
Cp_s  = 800; % silica specific heat capacity, J/(kg*K)
%----------------------- OPEN FILE  ----------------------------------%
% Read the second column from the Excel file %
F = xlsread(filename,'A:A');
```

146

```matlab
time = xlsread(filename,'C:C');

W_Temp = xlsread(filename,'D:D');

P_avgTemp = xlsread(filename,'E:E');

F1 = length(F); %total data points

CalW_temp= zeros([F1 1]); % create an empty array for the calibrated wall temperature

CalP_temp= zeros([F1 1]); % create an empty array for the calibrated avg particle
temperature

for x=1:F1

    CalW_temp(x)=-1*10^-6*W_Temp(x).^2+0.0213*W_Temp(x)-29.091;

    % to account for the missing temperature data, replace the missing data point with
the preceding value.

    % first replace all NaN cells by 0 and then assign the value to all the zeros

    CalW_temp(isnan(CalW_temp))=0; % replaces all the NaN by a value 0

    if CalW_temp(x)==0 % if condition replaces only values that are 0

        CalW_temp(x)=CalW_temp(x-1);

    end

    CalP_temp(x)=-3*10^-7*P_avgTemp(x).^2+0.0097*P_avgTemp(x)-2.0134;


    % to account for the missing temperature data, replace the missing data point with
the preceding value.

    % first replace all NaN cells by 0 and then assign the value to all the zeros

    CalP_temp(isnan(CalP_temp))=0; % replaces all the NaN by a value 0

     if CalP_temp(x)==0
```

```
        CalP_temp(x)=CalP_temp(x-1);

    end

end

Tinitial= CalP_temp(1); % set initial particle temperature

LNFUN = log((CalW_temp - CalP_temp)./(CalW_temp - Tinitial)) ;

figure(1)

plot(time,CalP_temp,'r*',time,CalW_temp,'ko')

xlabel('Time [s]')

ylabel('Temperature [^oC]')

legend('Solid bed','Drum wall','Location','northwest')

p = polyfit(time, LNFUN(1:F1),1); % trendline

ln_reg = polyval(p,time(1:F1));  % linear regression curve

% assign es value based on Fill level

if (FillLevel==10)

    es=0.19;

elseif (FillLevel==17.5)

    es=0.25;

else

    es=0.28;

end

M_particle  =  0.0215*FillLevel-0.0008; % derived the equation from the relationship

between fill level and mass of particles

ht_c= p(1).*-1*M_particle.*Cp_s/(es*A*L);
```

```
figure(2)

plot(time, LNFUN,'.',time,ln_reg) ; %ln_fun plot

xlabel('Time [s]')

ylabel('ln((T_{w}-T_{s})/(T_{w}-T_{s0}))')

txt = ['Heat Transfer Coefficient = ' num2str(ht_c) ' [W/(m^2K)]'];

text(150,-0.2,txt,'Color','red','FontSize',12)

e = cputime-z
```

APPENDIX D

RAW DATA FOR CONDUCTION HEAT TRANSFER EXPERIMENTS

(a)

(b)
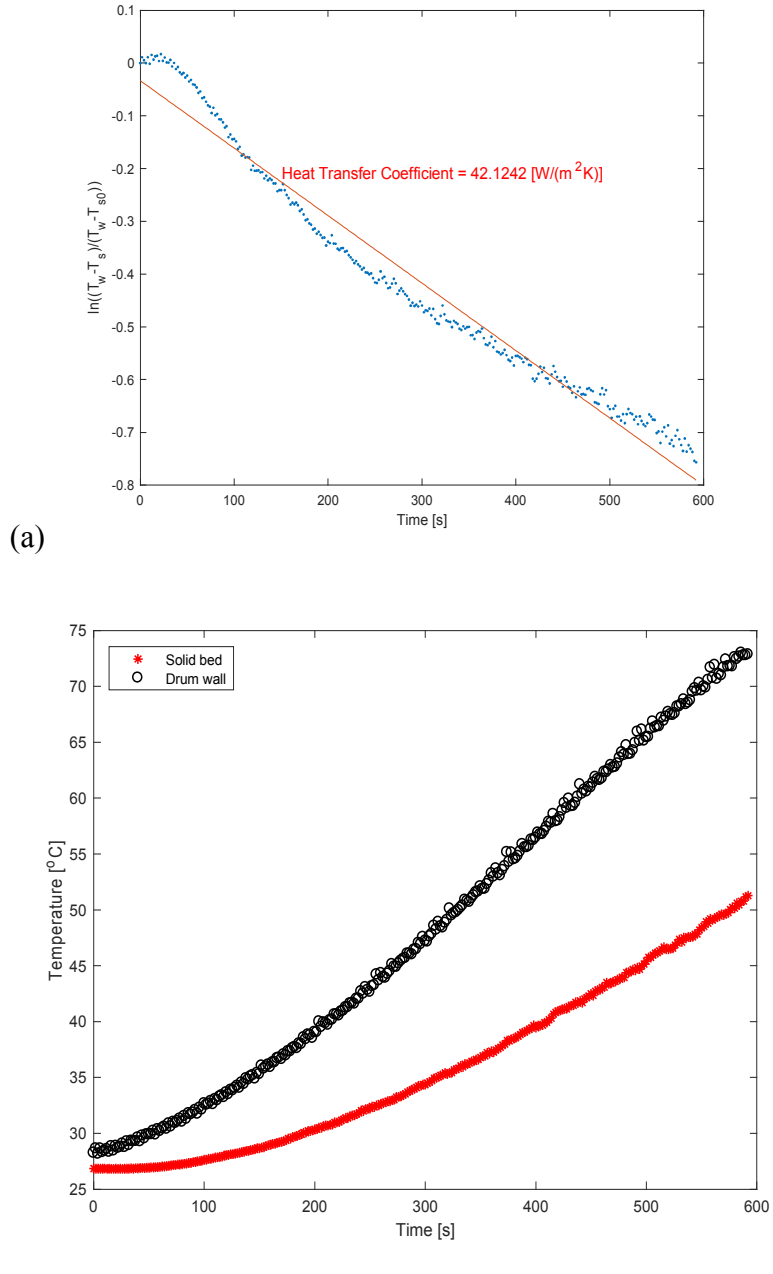
Figure A 3 (a) Heat transfer coefficient and (b) average temperatures at 17.5 %

fill level and 10 rpm for trial 1.
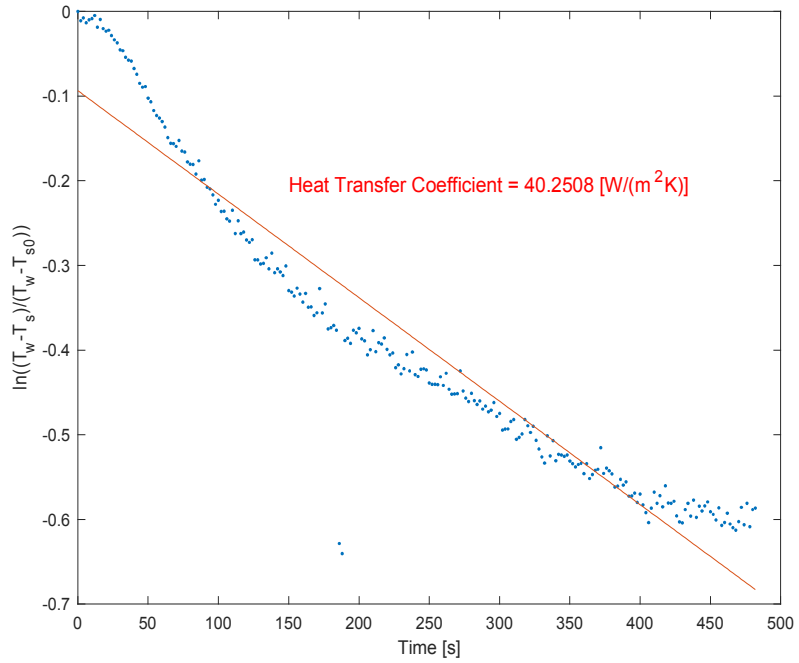
(a)
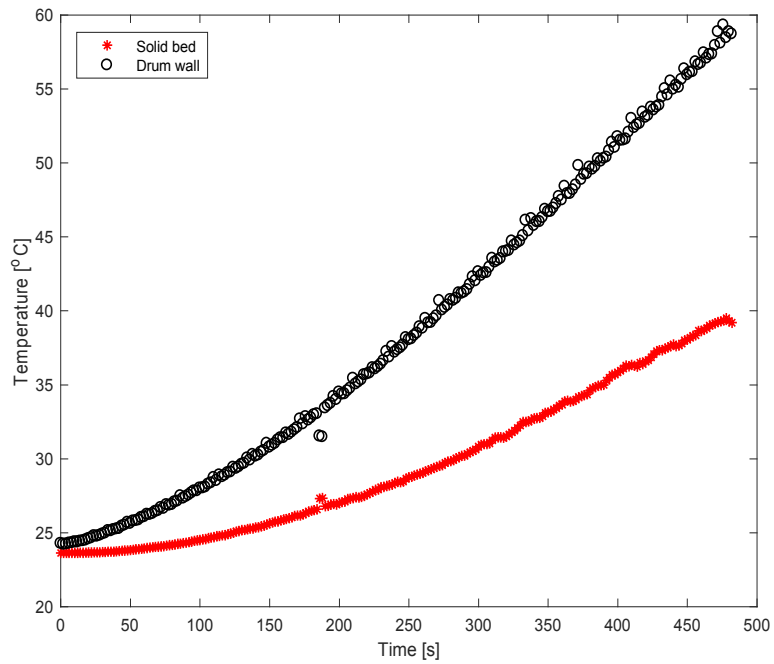
(b)

Figure A 4 (a) Heat transfer coefficient and (b) average temperatures at 17.5 %

fill level and 10 rpm for trial 2.
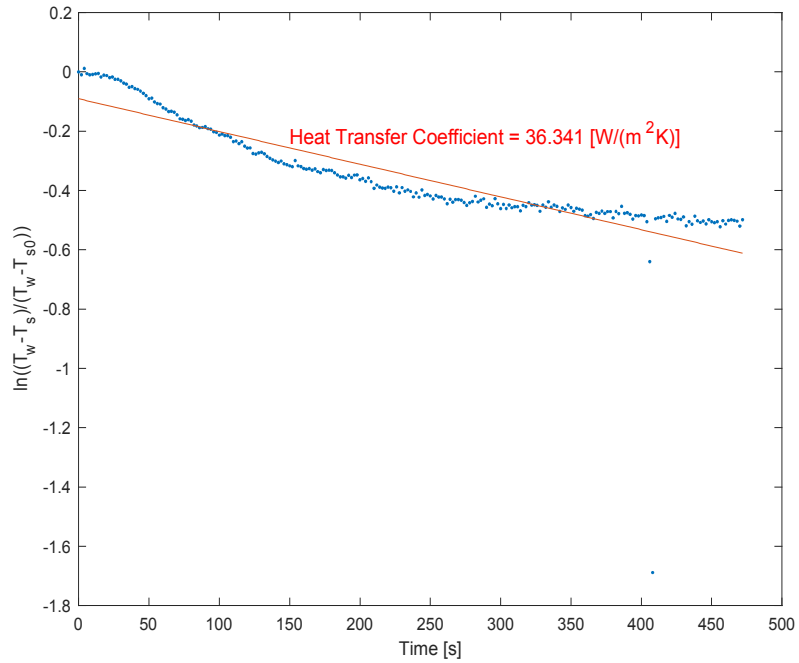
(a)
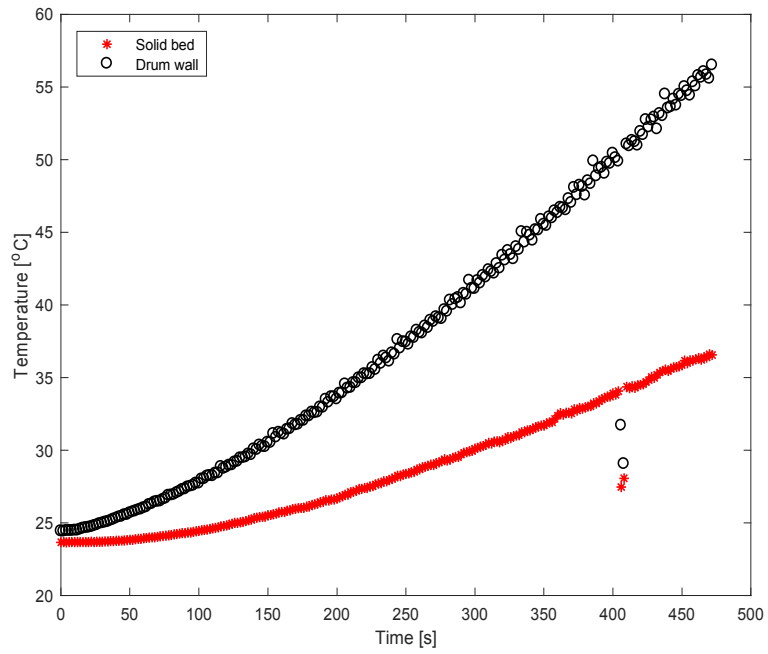
(b)

Figure A 5 (a) Heat transfer coefficient and (b) average temperatures at 17.5 %

fill level and 10 rpm for trial 3.
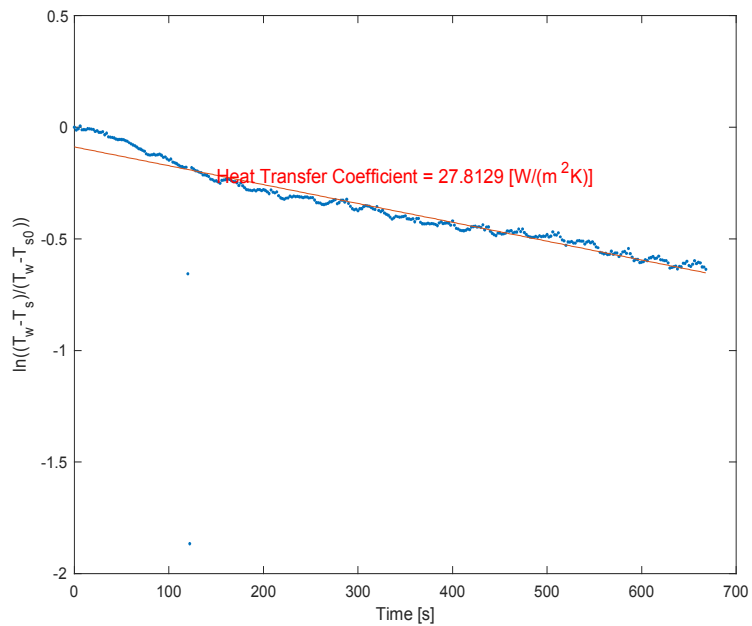
(a)
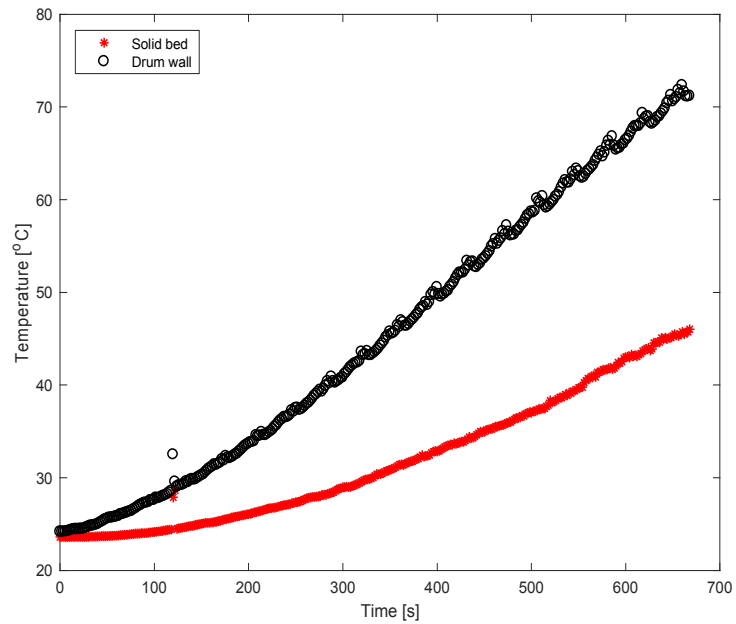
(b)

Figure A 6 (a) Heat transfer coefficient and (b) average temperatures at 17.5 %

fill level and 2 rpm for trial 1.

154
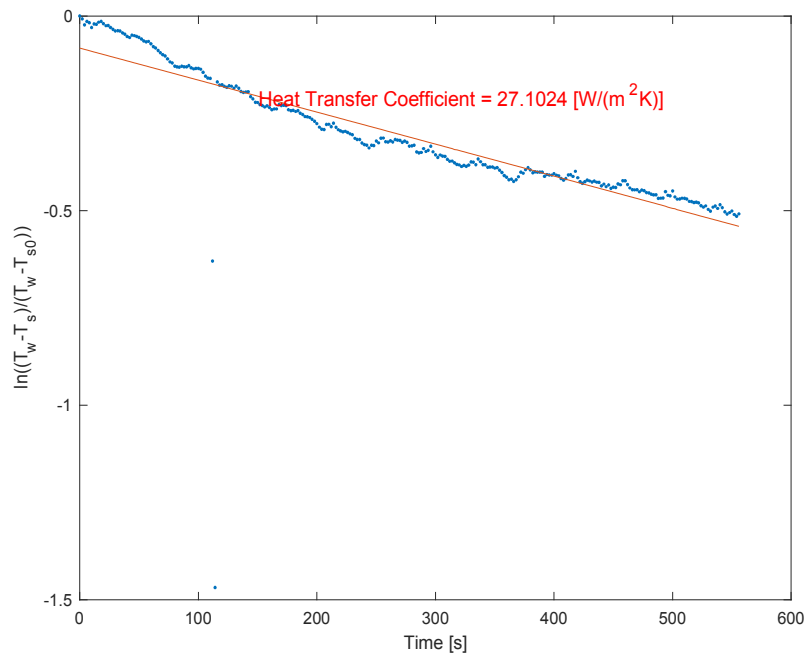
(a)
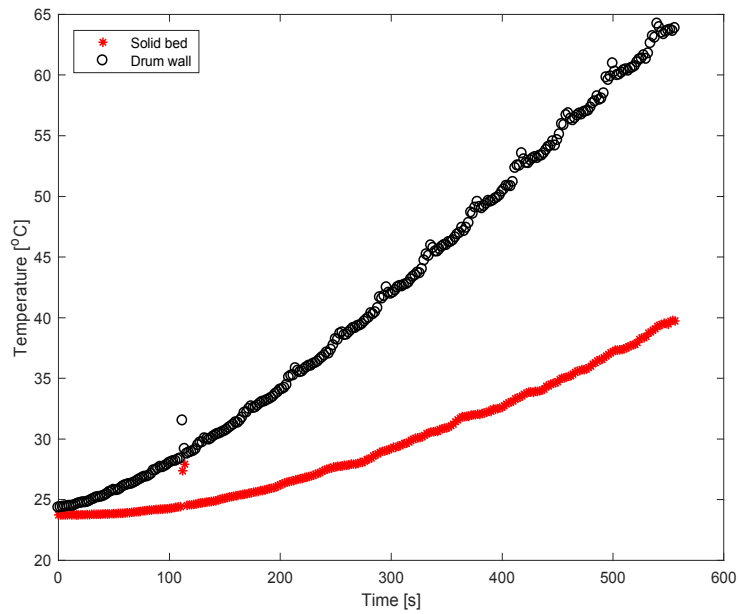
(b)

Figure A 7 (a) Heat transfer coefficient and (b) average temperatures at 17.5 %

fill level and 2 rpm for trial 2.
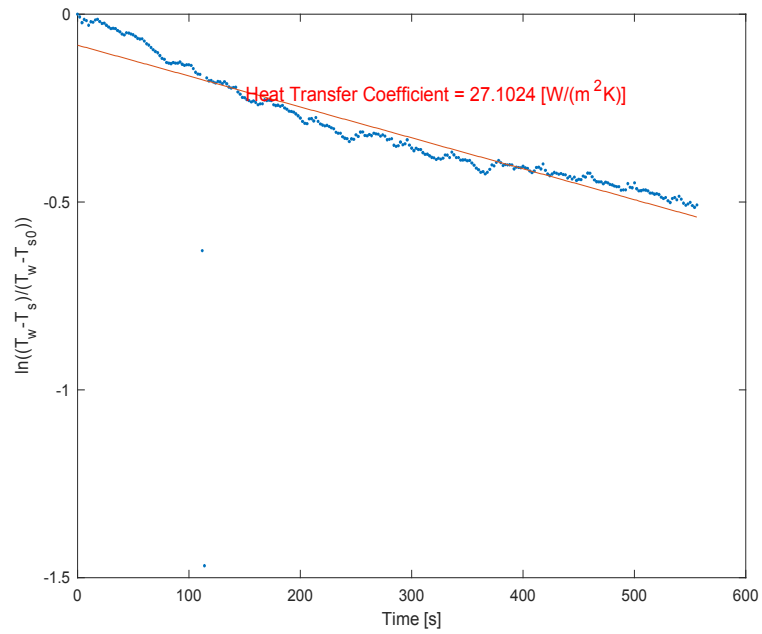
(a)
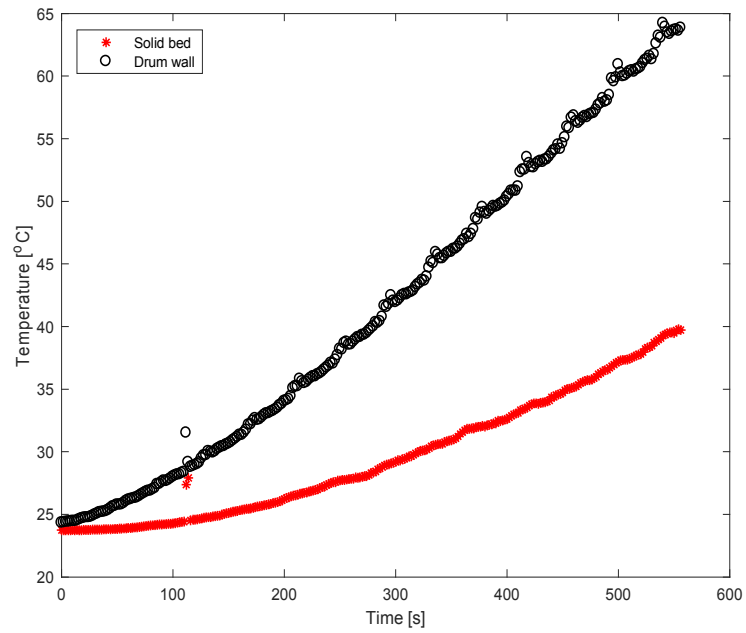
(b)

Figure A 8 (a) Heat transfer coefficient and (b) average temperatures at 17.5 %

fill level and 2 rpm for trial 3.
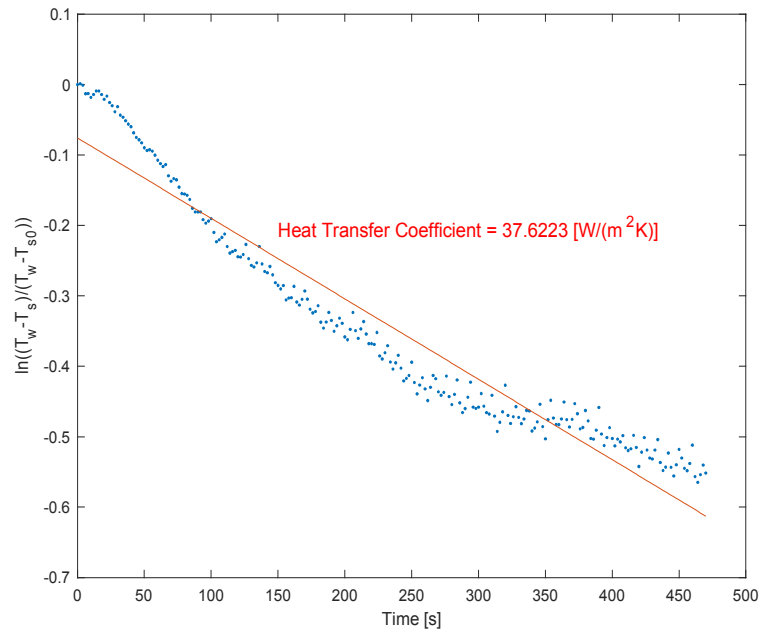
(a)
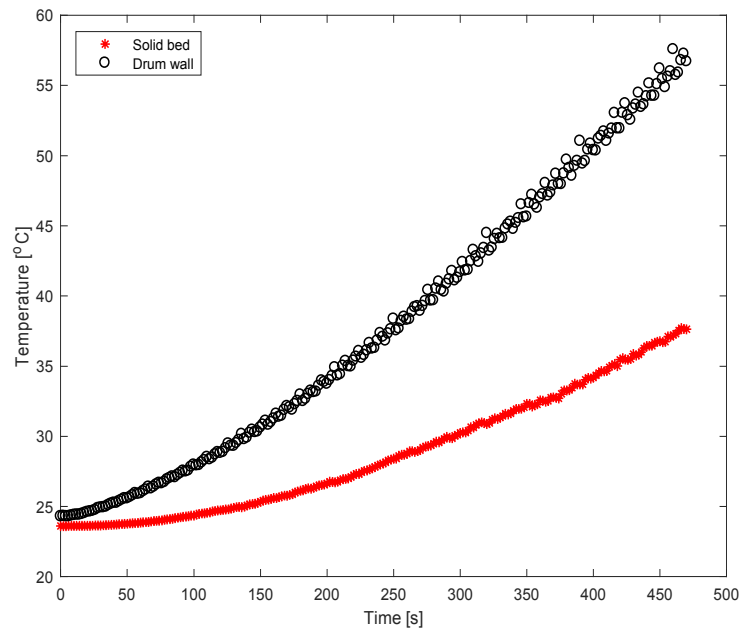
(b)

Figure A 9 (a) Heat transfer coefficient and (b) average temperatures at 17.5 %

fill level and 6 rpm for trial 1.
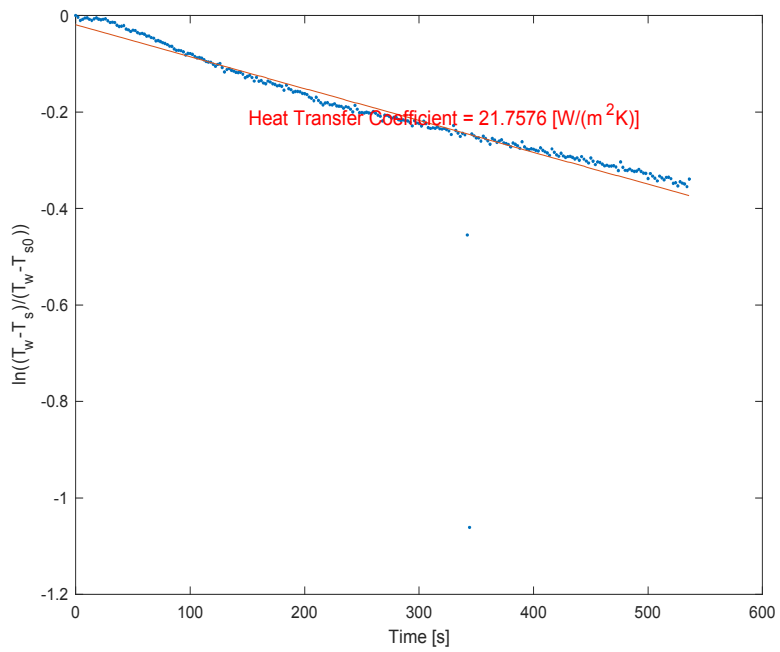
(a)
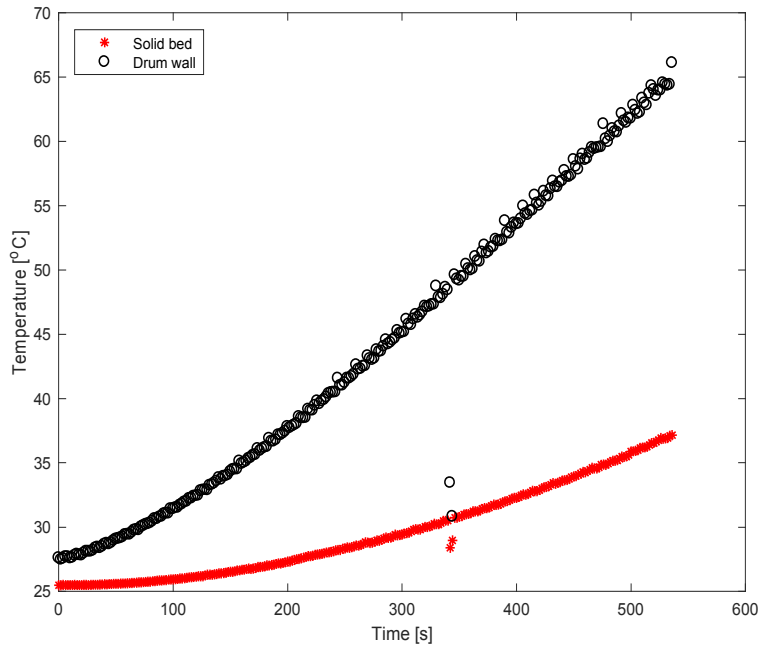
(b)

Figure A 10 (a) Heat transfer coefficient and (b) average temperatures at 17.5 %

fill level and 6 rpm for trial 2.

158
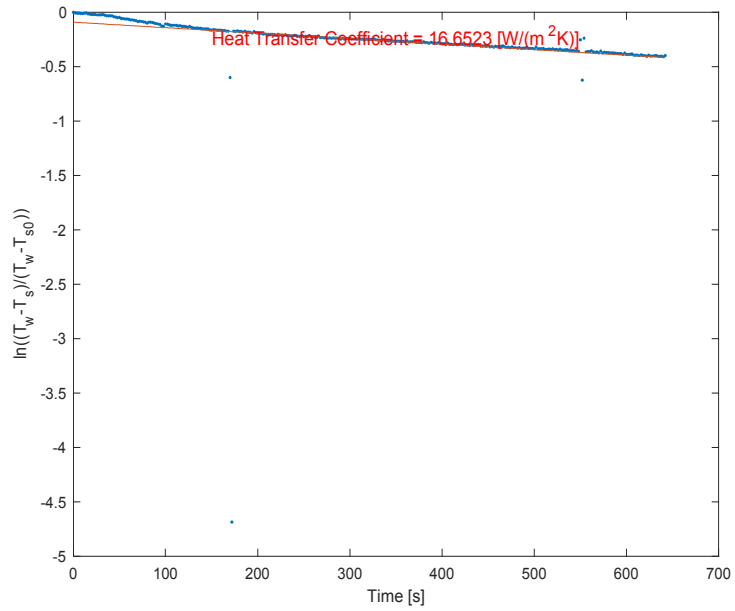
(a)
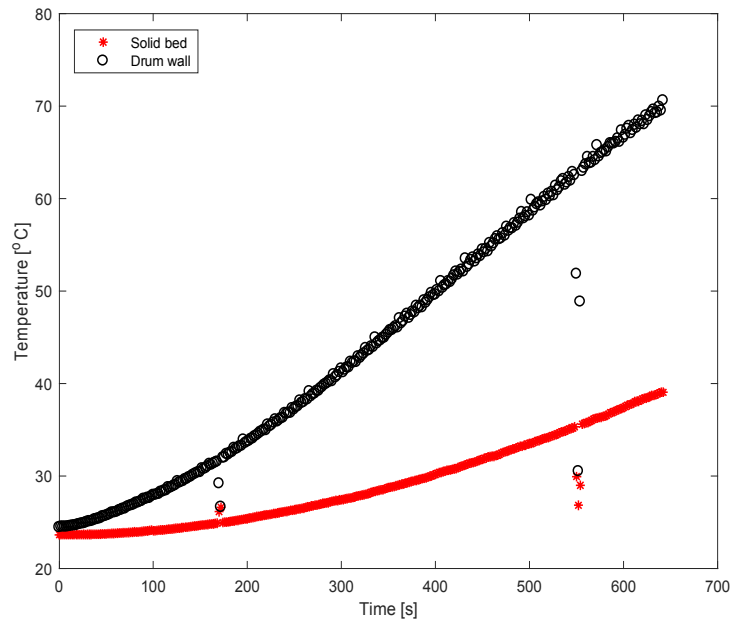
(b)

Figure A 11 (a) Heat transfer coefficient and (b) average temperatures at 17.5 %

fill level and 6 rpm for trial 3.

159
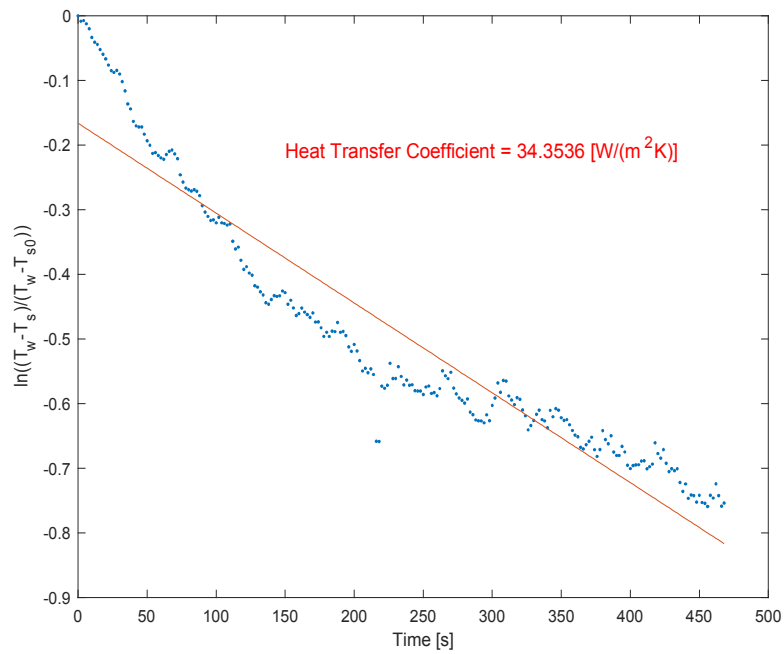
(a)
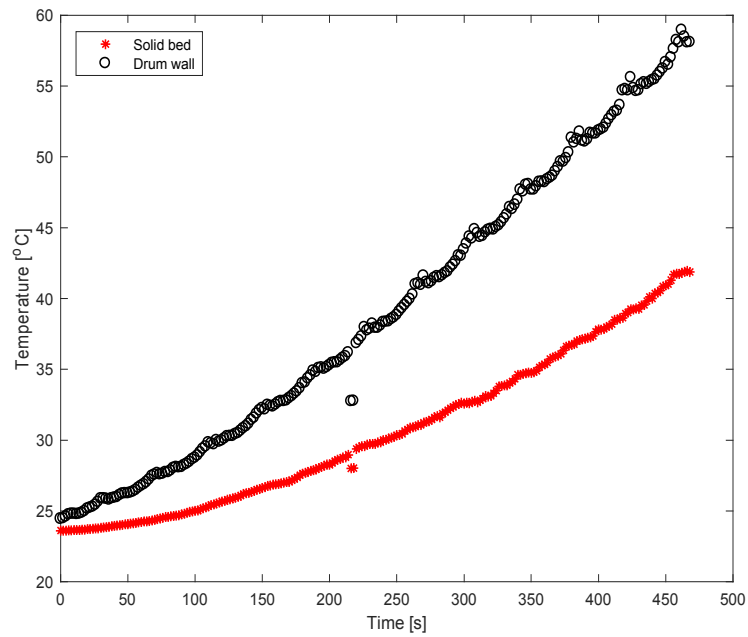
(b)

Figure A 12 (a) Heat transfer coefficient and (b) average temperatures at 10 %

fill level and 2 rpm for trial 1.
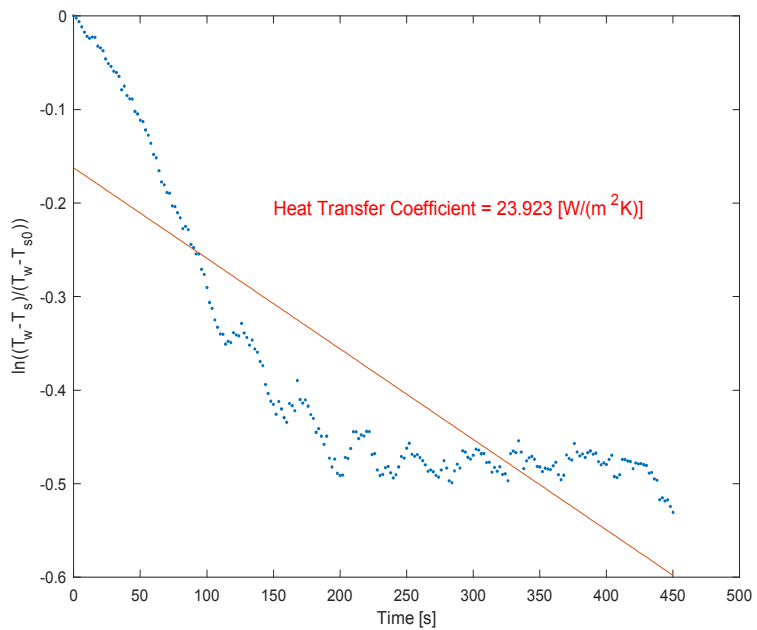
(a)
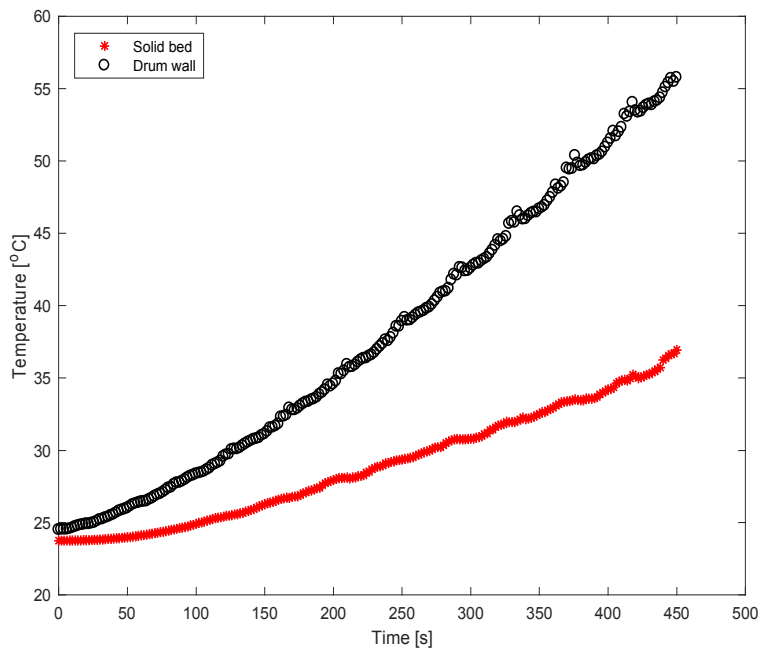
(b)

Figure A 13 (a) Heat transfer coefficient and (b) average temperatures at 10 %

fill level and 2 rpm for trial 2.
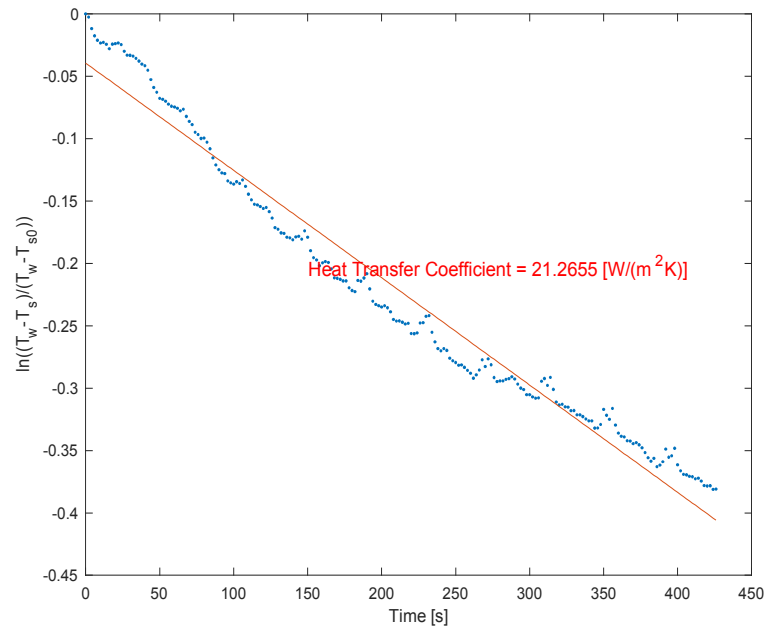
(a)
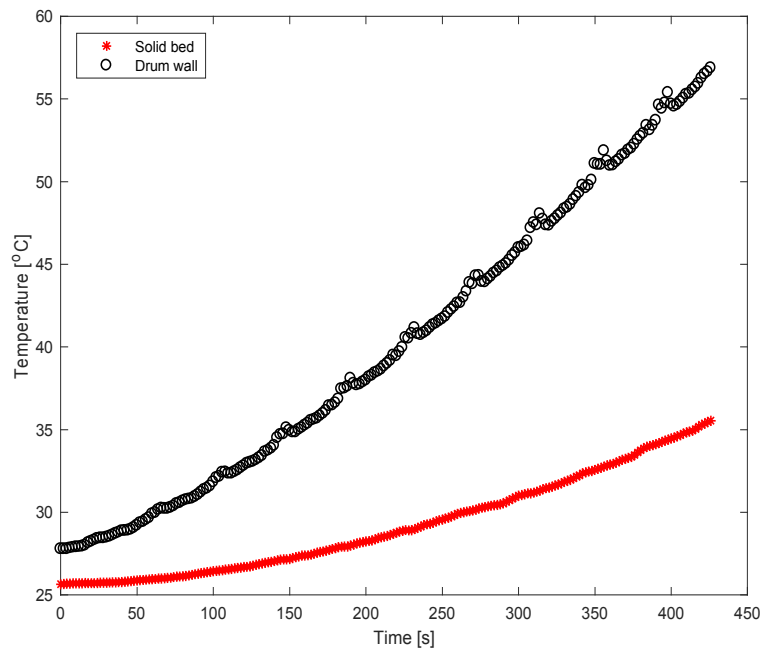
(b)

Figure A 14 (a) Heat transfer coefficient and (b) average temperatures at 10 %

fill level and 2 rpm for trial 3.
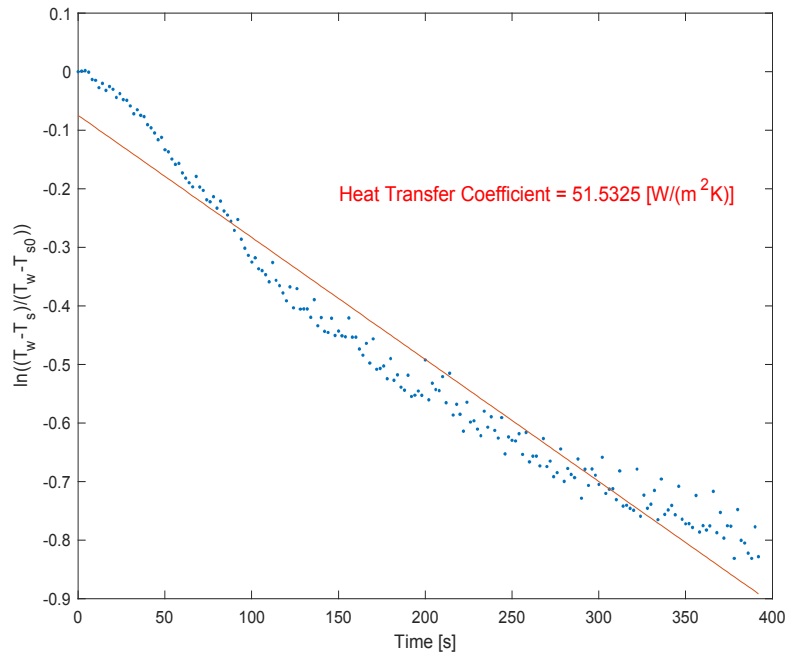
(a)
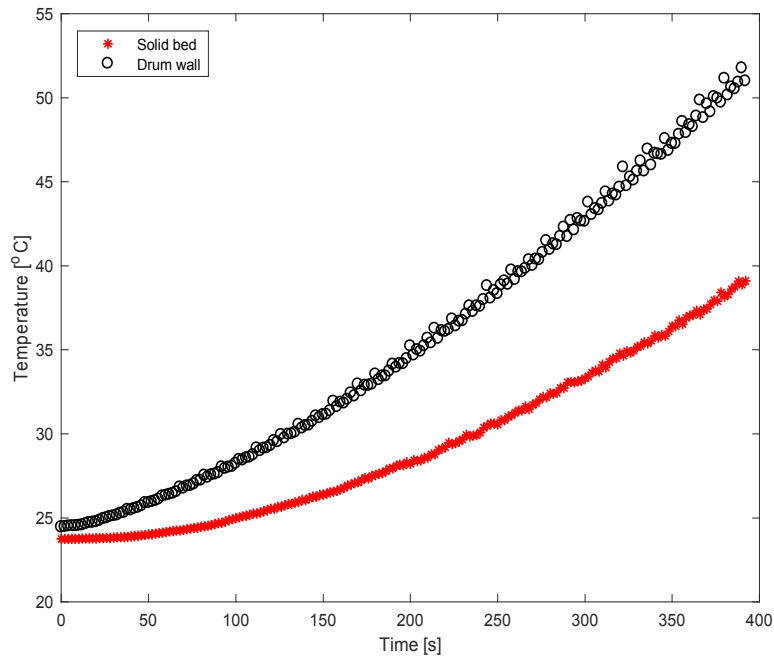
(b)

Figure A 15 (a) Heat transfer coefficient and (b) average temperatures at 10 %

fill level and 10 rpm for trial 1.
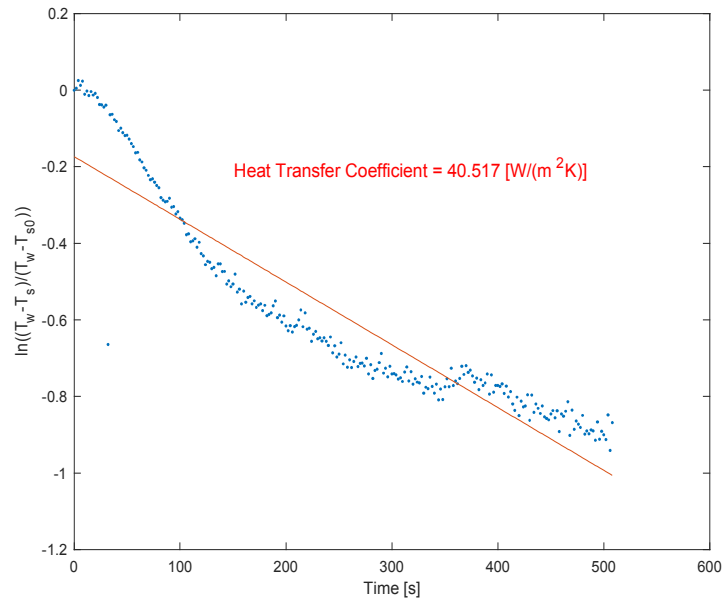
(a)
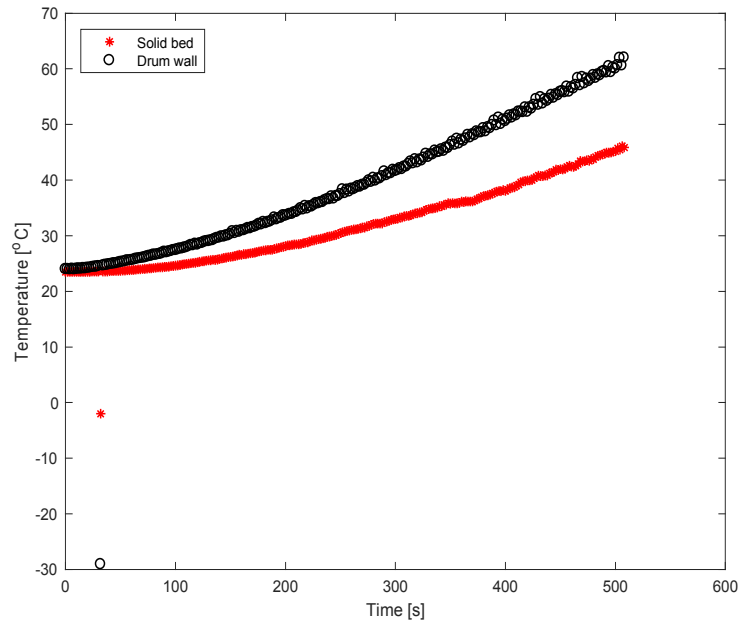
(b)

Figure A 16 (a) Heat transfer coefficient and (b) average temperatures at 10 %

fill level and 10 rpm for trial 2.
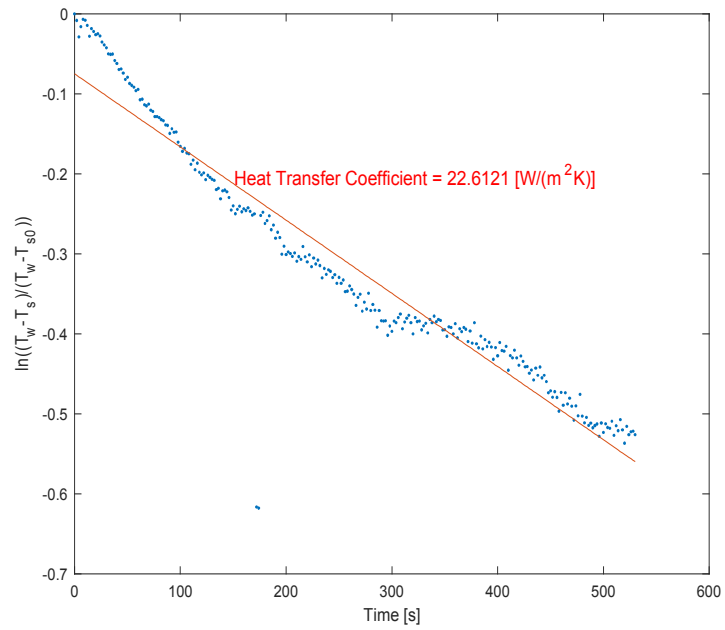
(a)
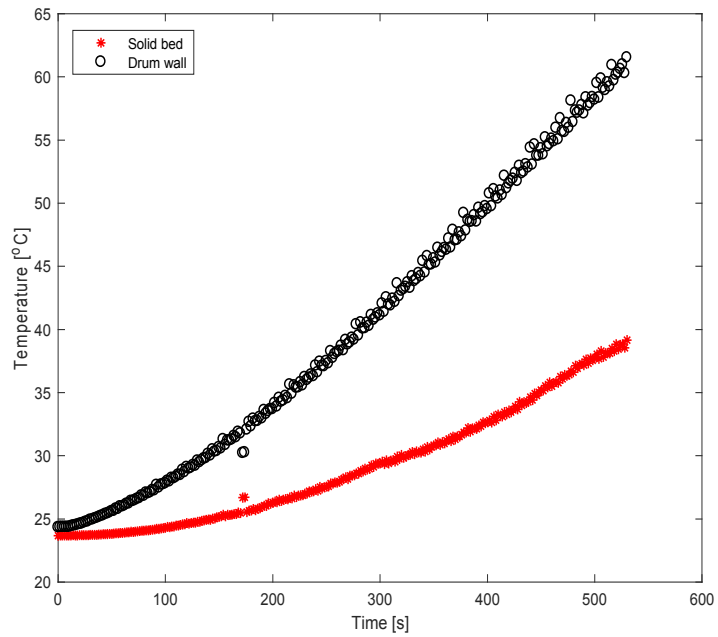
(b)

Figure A 17 (a) Heat transfer coefficient and (b) average temperatures at 10 %

fill level and 10 rpm for trial 3.
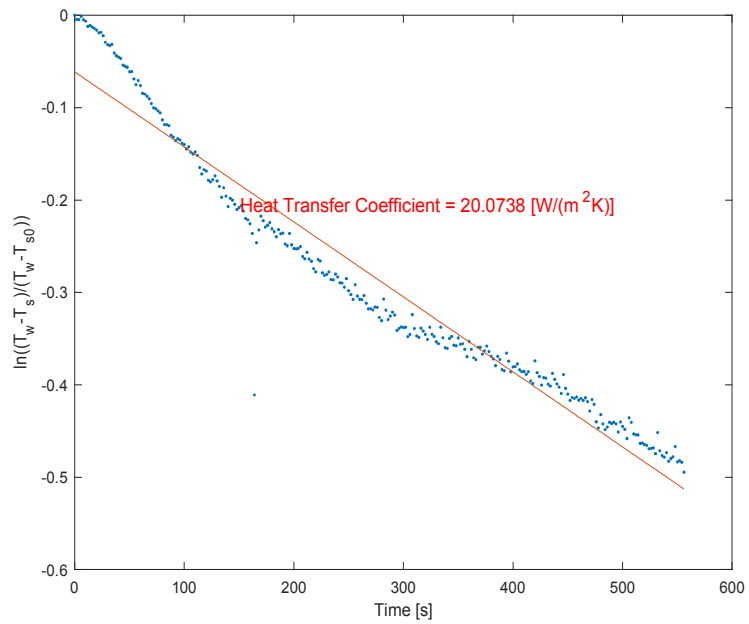
(a)
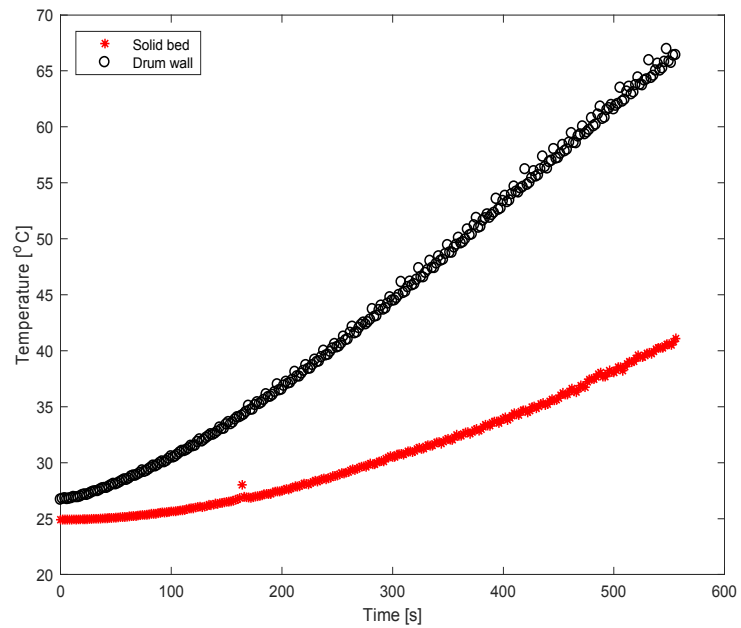
(b)

Figure A 18 (a) Heat transfer coefficient and (b) average temperatures at 10 %

fill level and 6 rpm for trial 1.
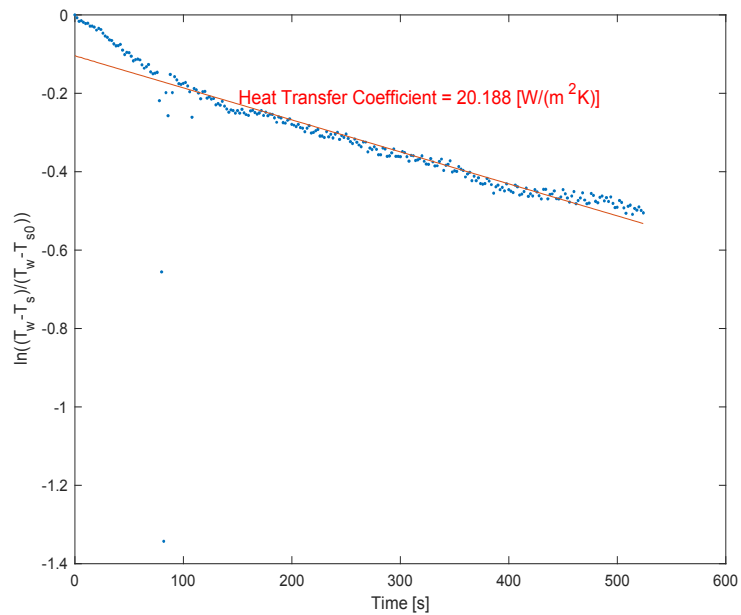
(a)
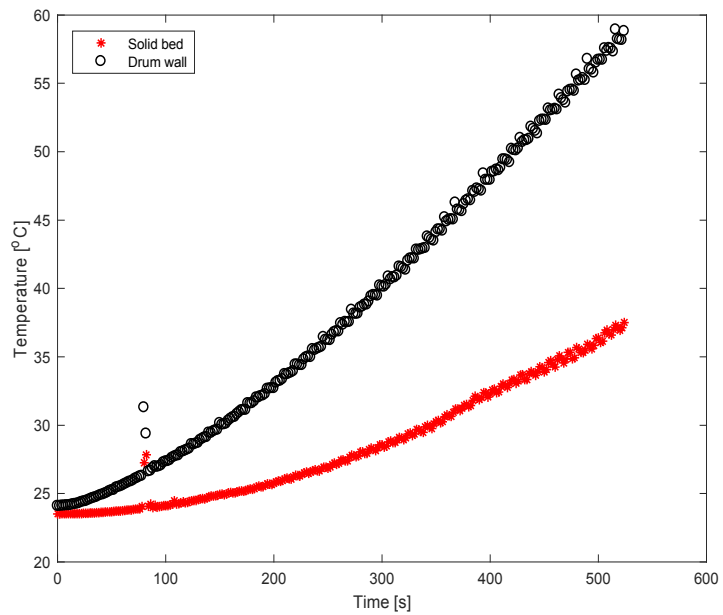
(b)

Figure A 19 (a) Heat transfer coefficient and (b) average temperatures at 10 %

fill level and 6 rpm for trial 2.

167
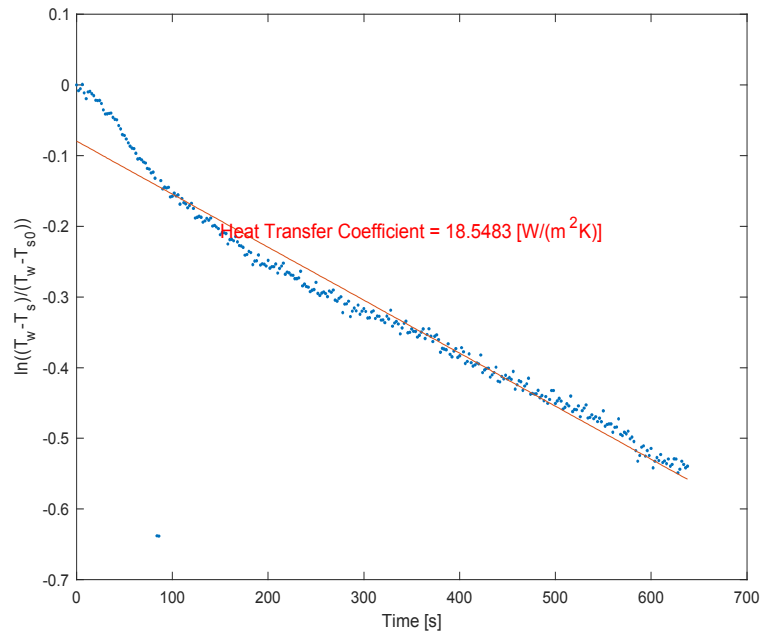
(a)
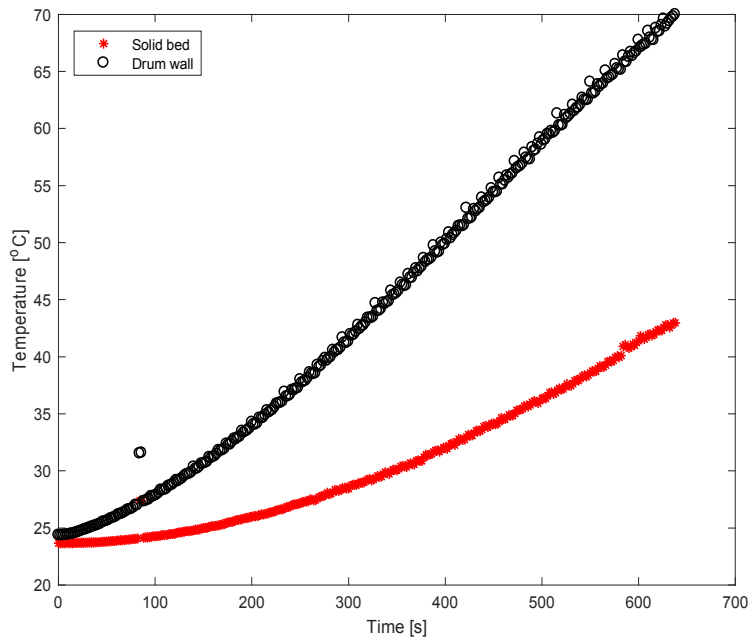
(b)

Figure A 20 (a) Heat transfer coefficient and (b) average temperatures at 10 %

fill level and 6 rpm for trial 3.
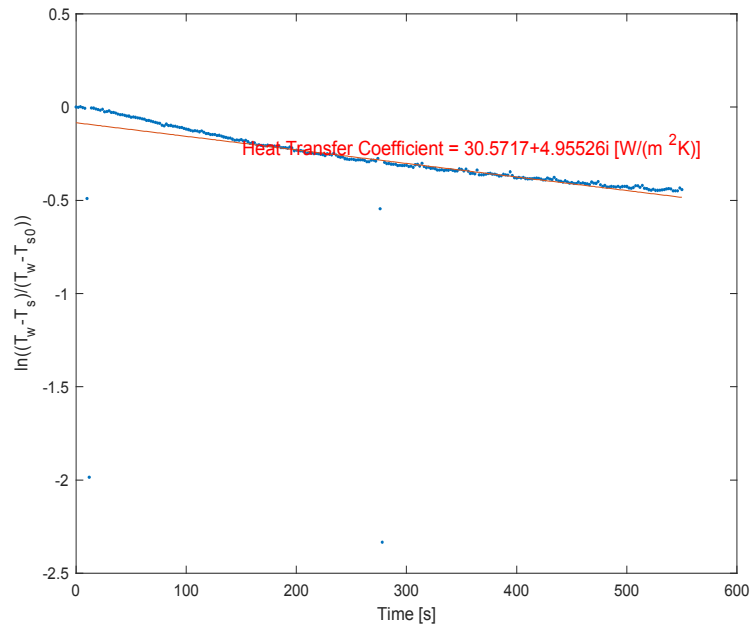
(a)
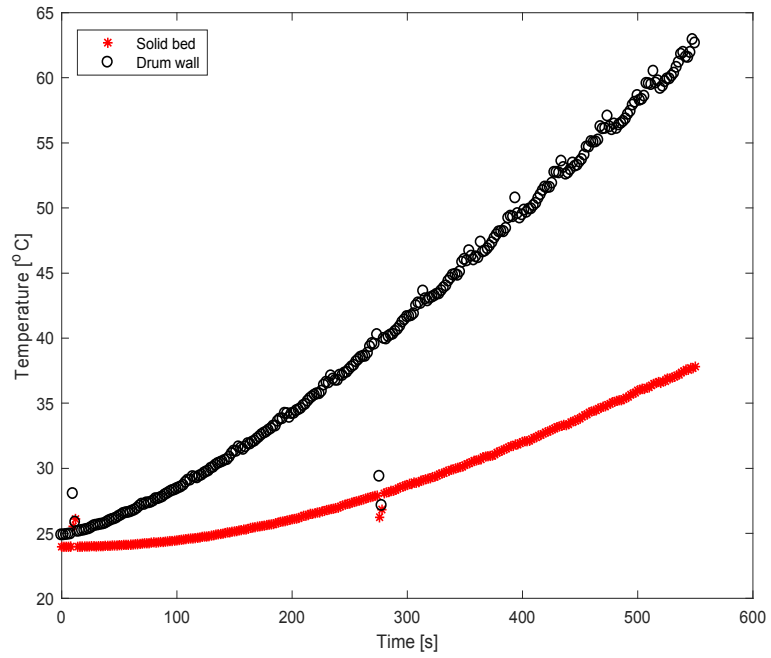
(b)

Figure A 21 (a) Heat transfer coefficient and (b) average temperatures at 25 %

fill level and 2 rpm for trial 1.
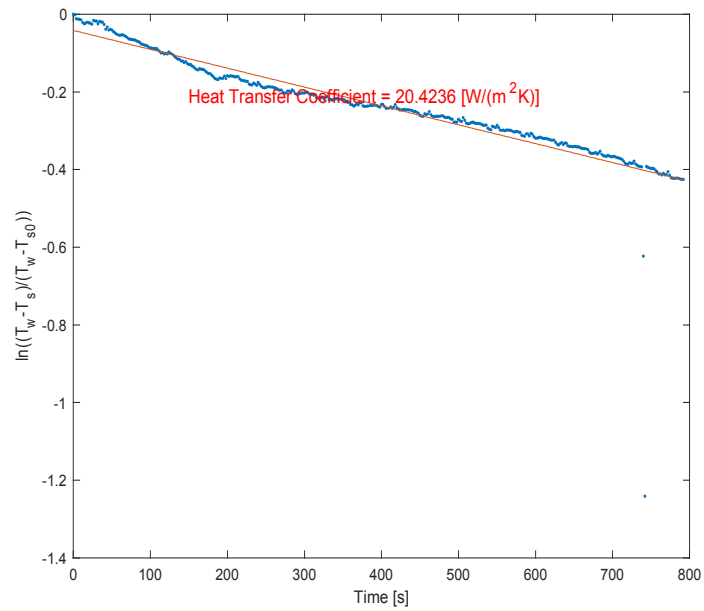
(a)
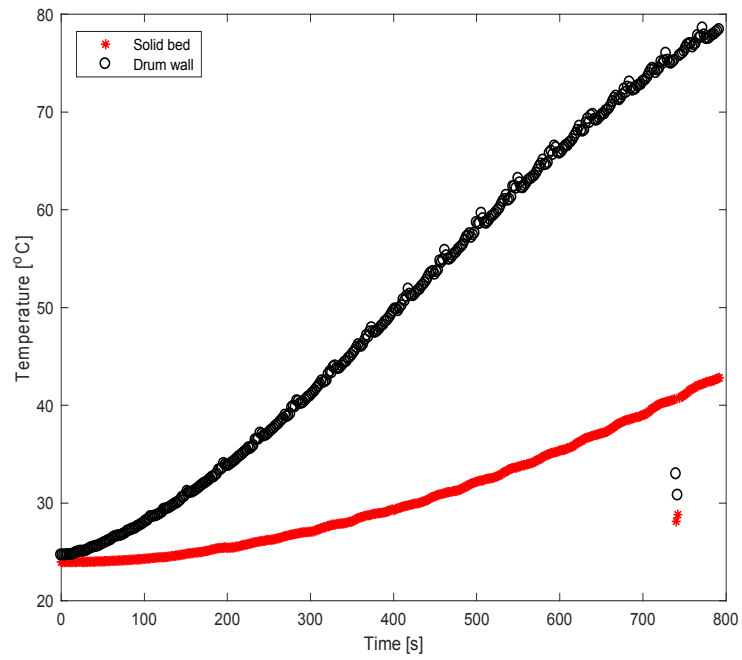
(b)

Figure A 22 (a) Heat transfer coefficient and (b) average temperatures at 25 %

fill level and 2 rpm for trial 2.
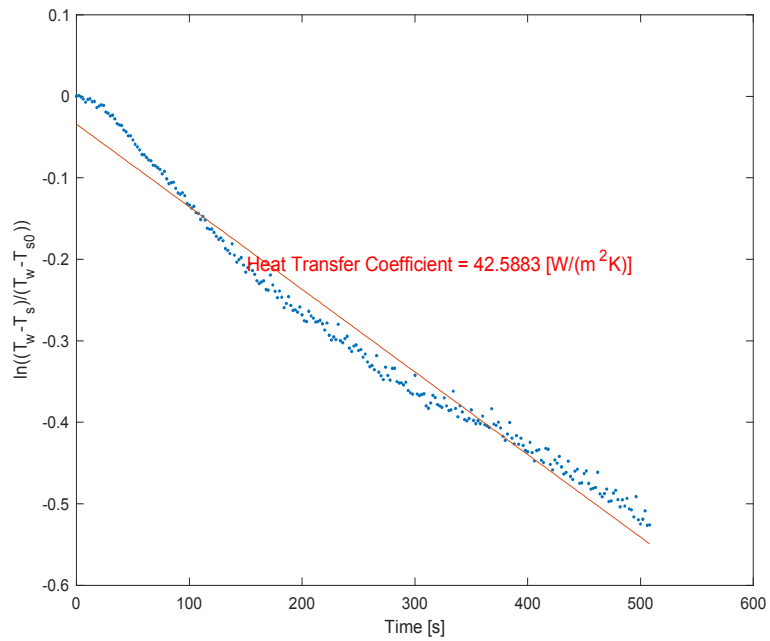
(a)
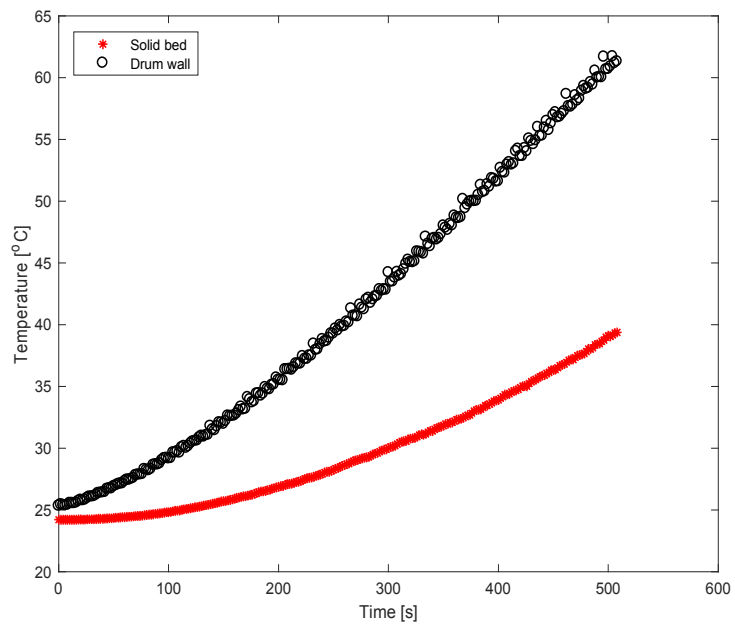
(b)

Figure A 23 (a) Heat transfer coefficient and (b) average temperatures at 25 %

fill level and 6 rpm for trial 1.
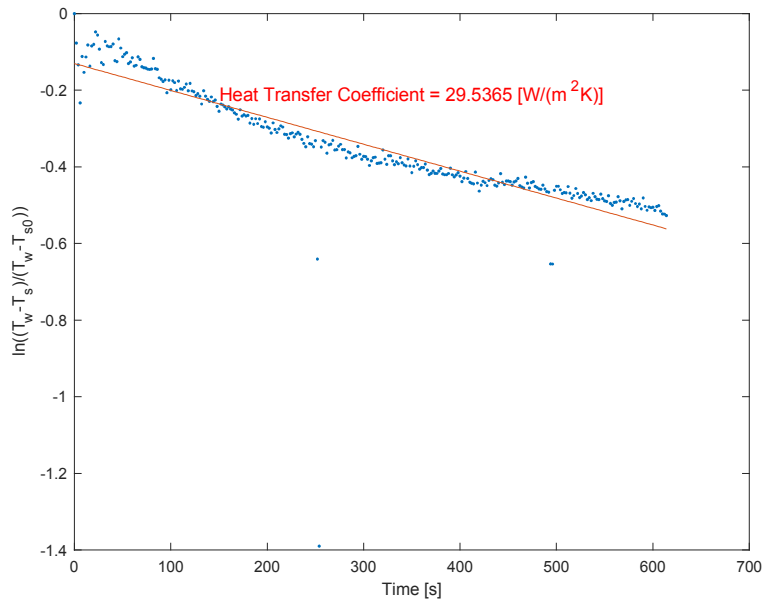
(a)
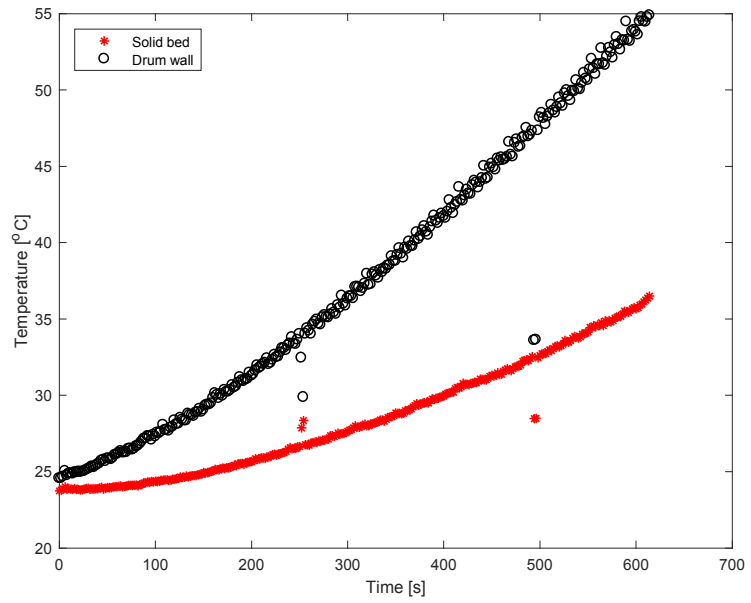
(b)

Figure A 24 (a) Heat transfer coefficient and (b) average temperatures at 25 %

fill level and 6 rpm for trial 2.
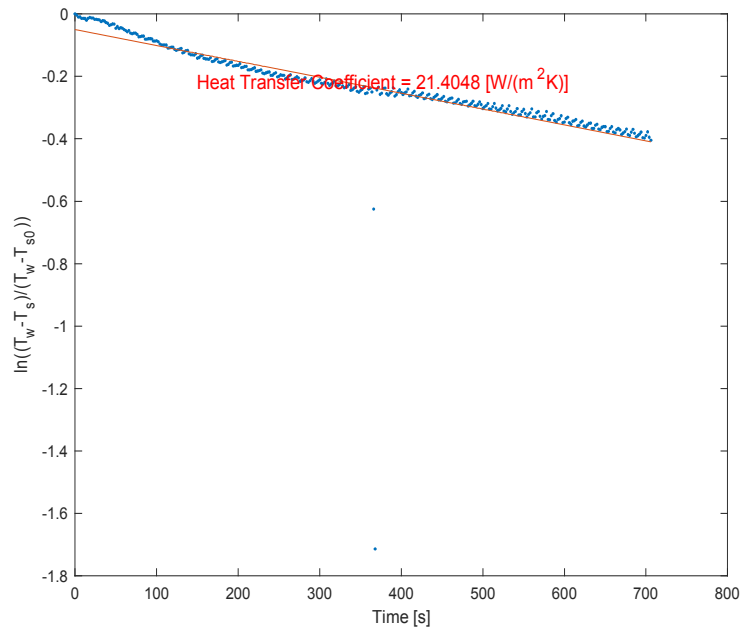
(a)
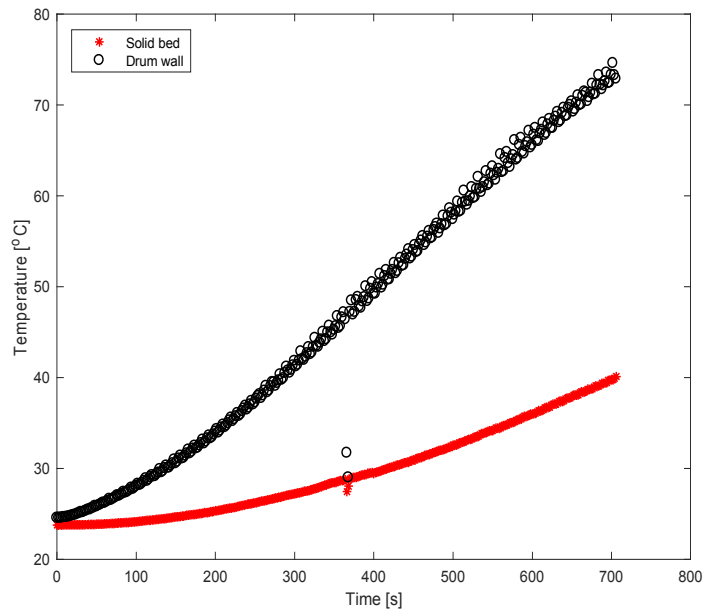
(b)

Figure A 25 (a) Heat transfer coefficient and (b) average temperatures at 25 %

fill level and 6 rpm for trial 3.
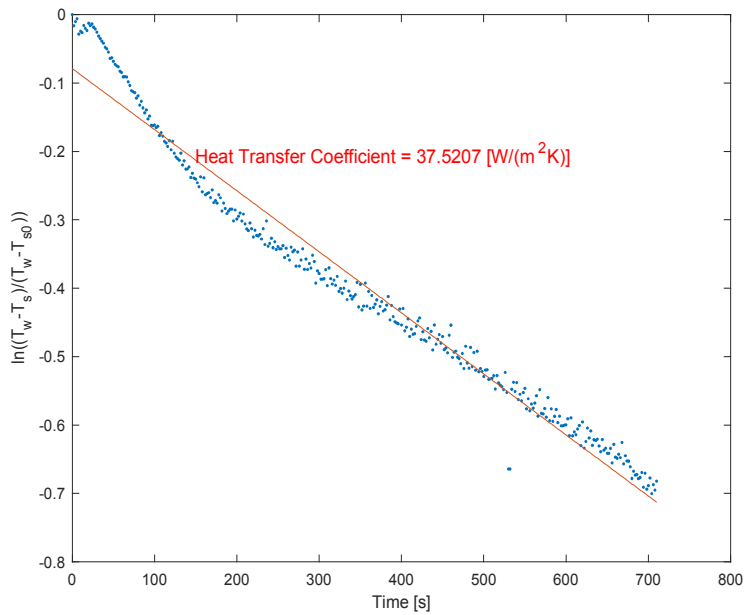
(a)
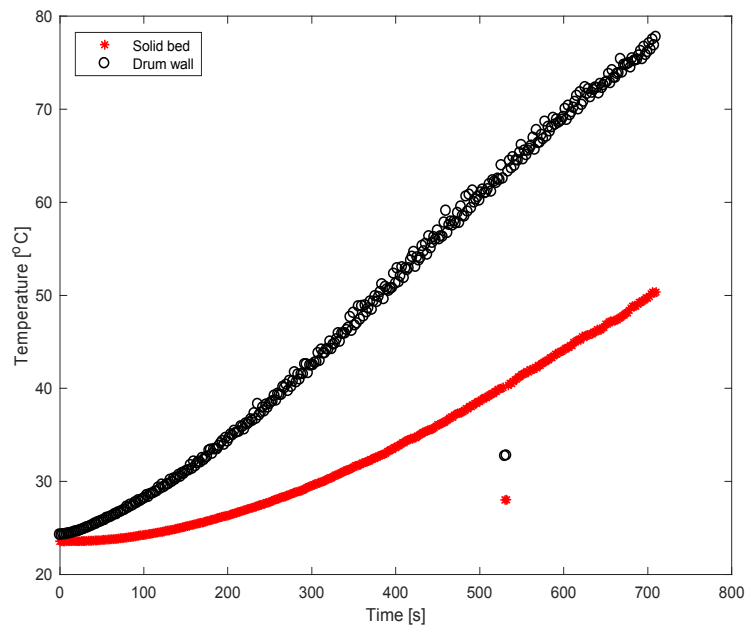
(b)

Figure A 26 (a) Heat transfer coefficient and (b) average temperatures at 25 %

fill level and 10 rpm for trial 1.
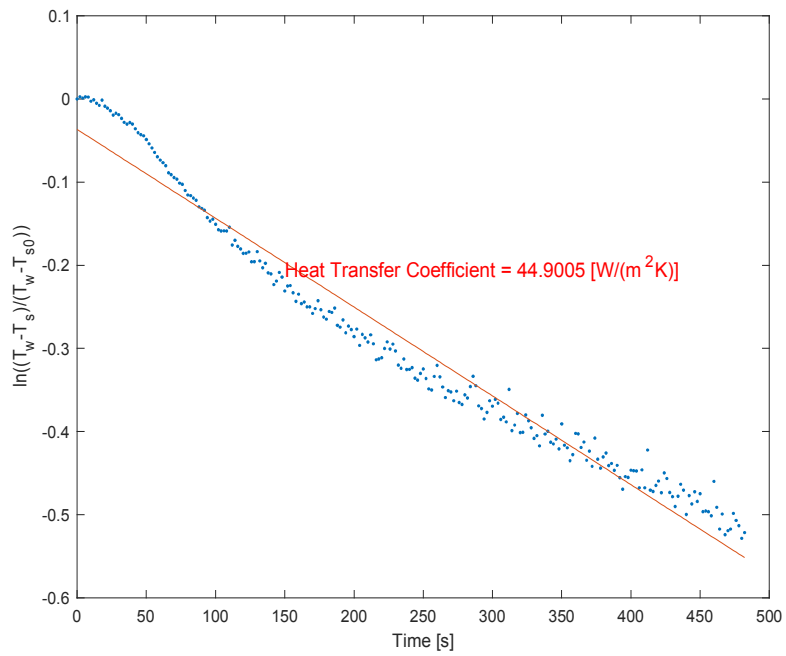
(a)
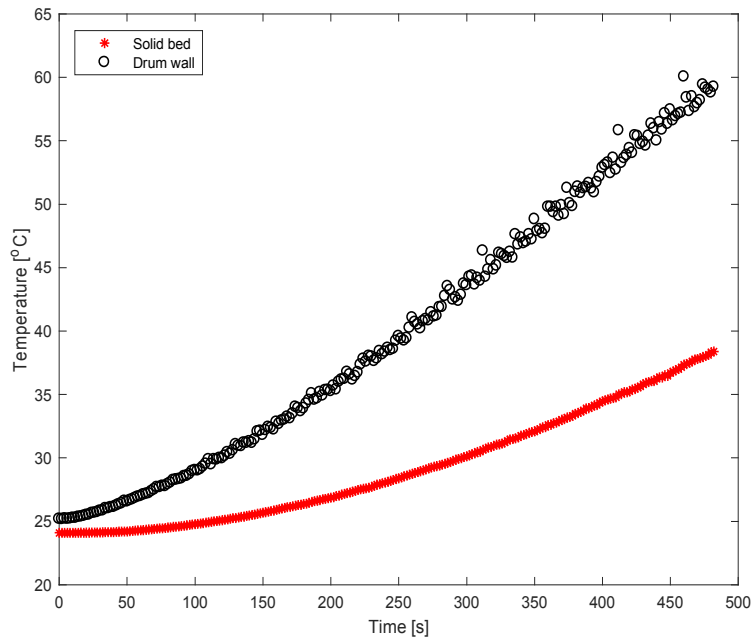
(b)

Figure A 27 (a) Heat transfer coefficient and (b) average temperatures at 25 %

fill level and 10 rpm for trial 2.
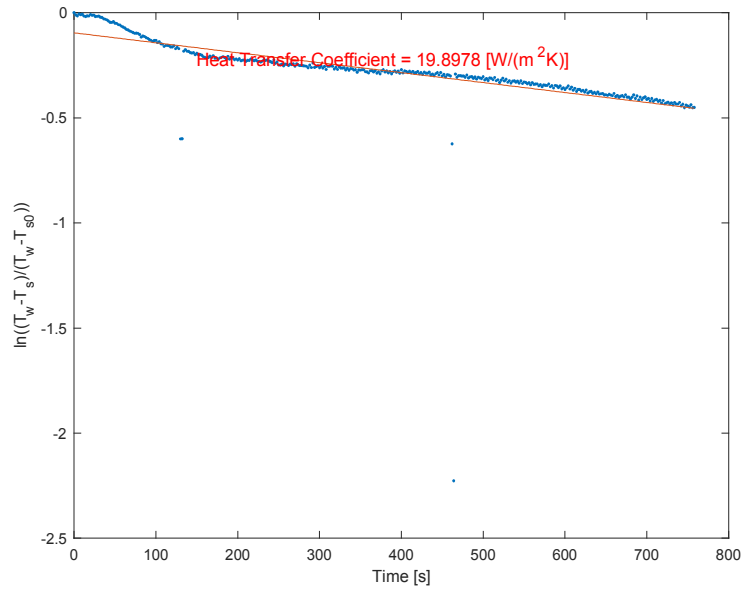
(a)
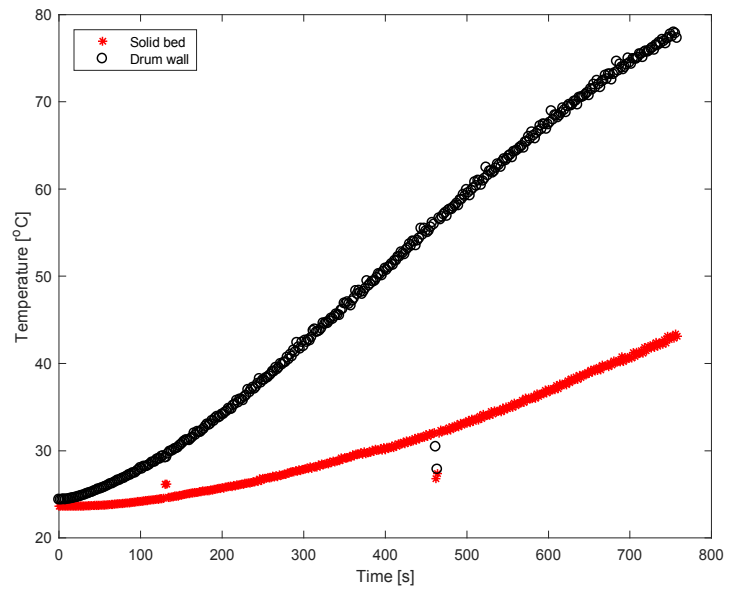
(b)

Figure A 28 (a) Heat transfer coefficient and (b) average temperatures at 25 %

fill level and 10 rpm for trial 3.

APPENDIX E

RAW DATA FOR CONVECTION HEAT TRANSFER EXPERIMENTS
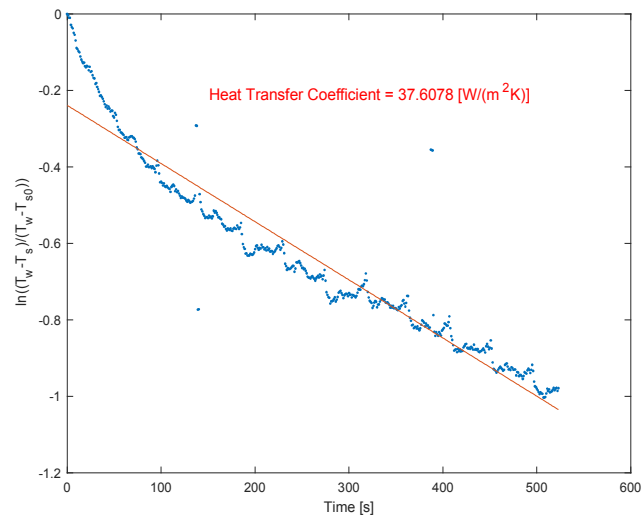
(a)
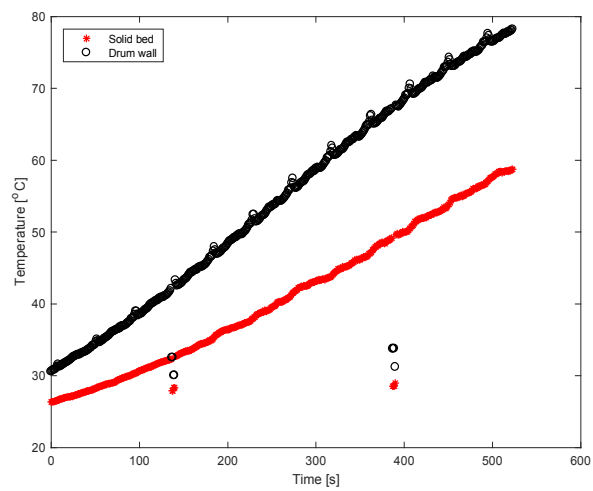
(b)

Figure A 29 (a) Heat transfer coefficient and (b) average temperatures at 10 %

fill level and 2 rpm for trial 1.
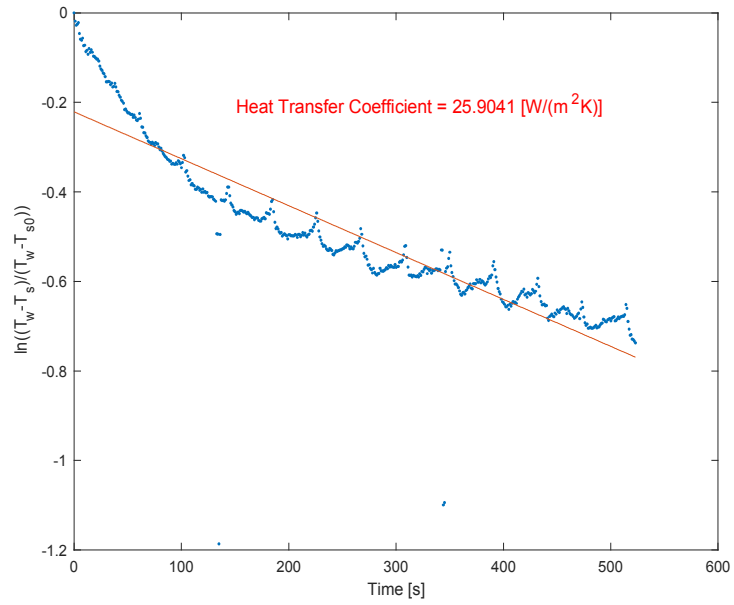
(a)
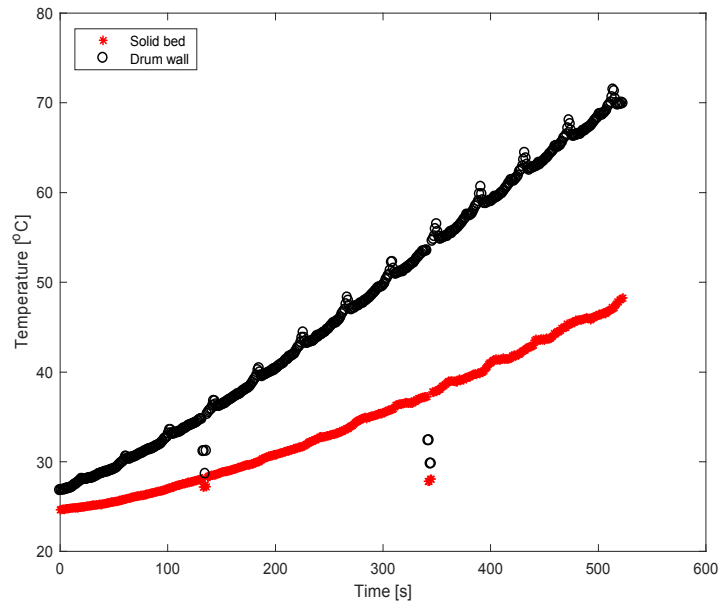
(b)

Figure A 30 (a) Heat transfer coefficient and (b) average temperatures at 10 %

fill level and 2 rpm for trial 2.
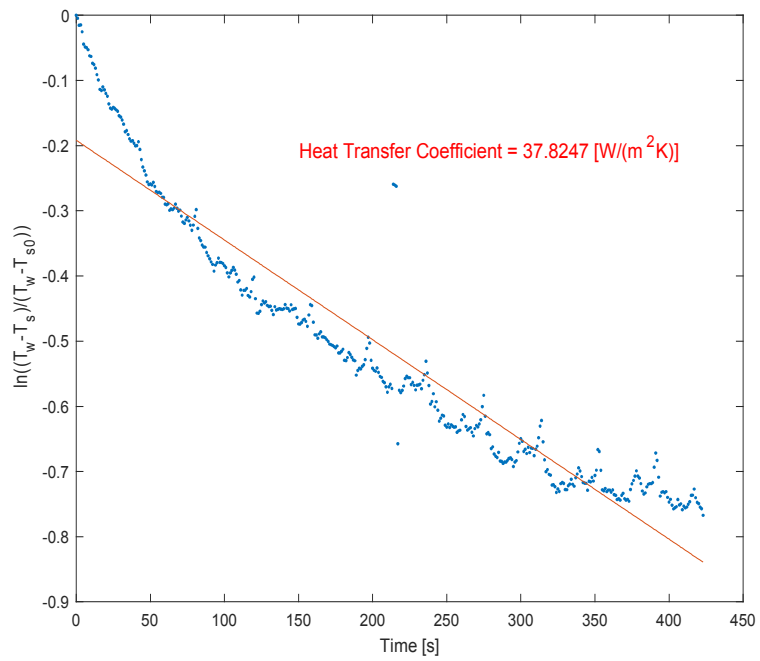
(a)
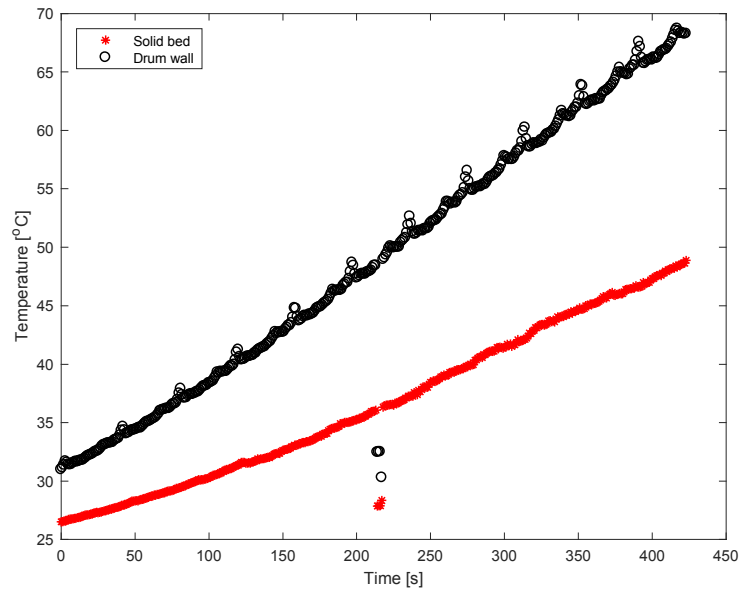
(b)

Figure A 31 (a) Heat transfer coefficient and (b) average temperatures at 10 %

fill level and 2 rpm for trial 3.
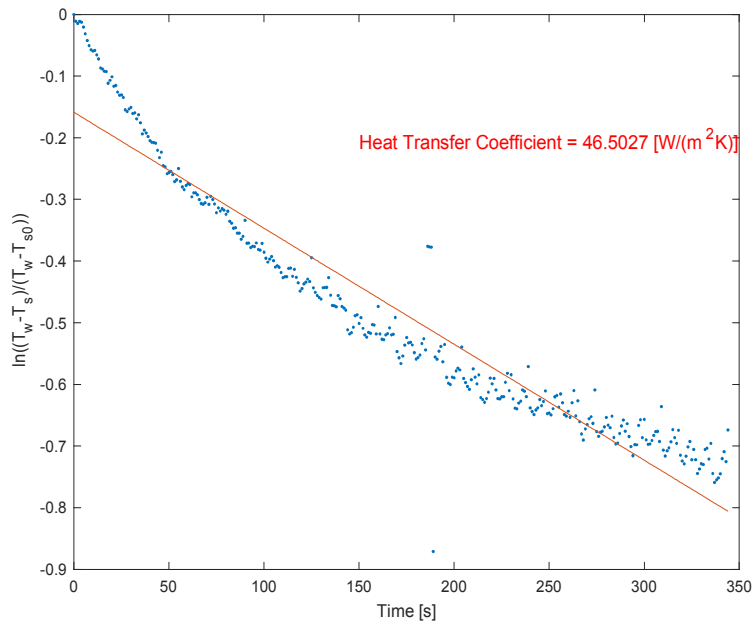
(a)
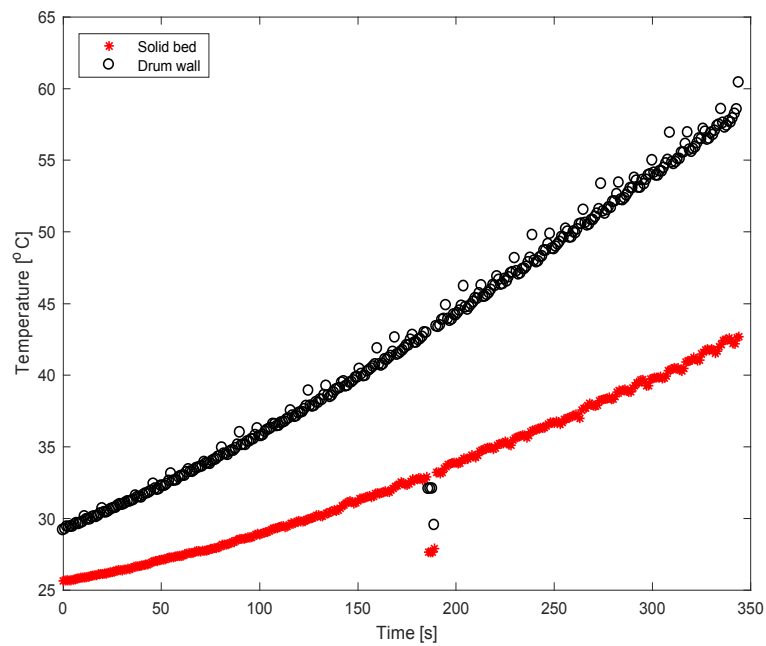
(b)

Figure A 32 (a) Heat transfer coefficient and (b) average temperatures at 10 %

fill level and 6 rpm for trial 1.
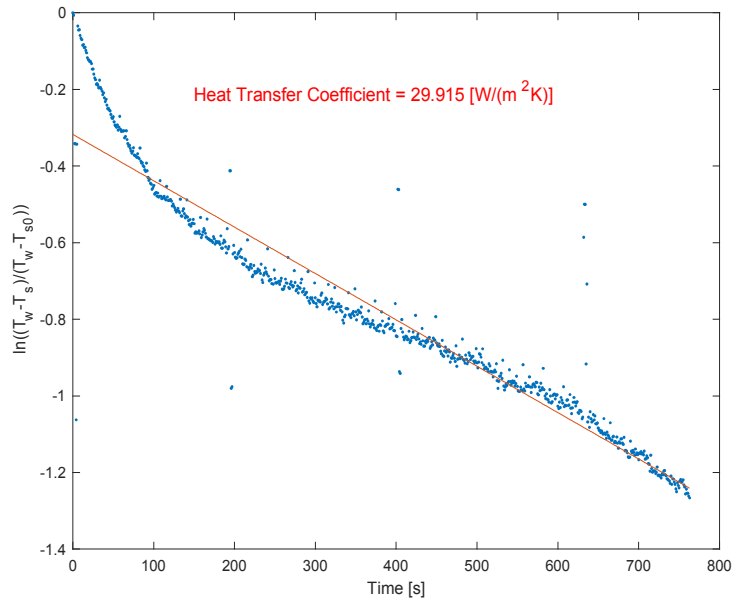
(a)
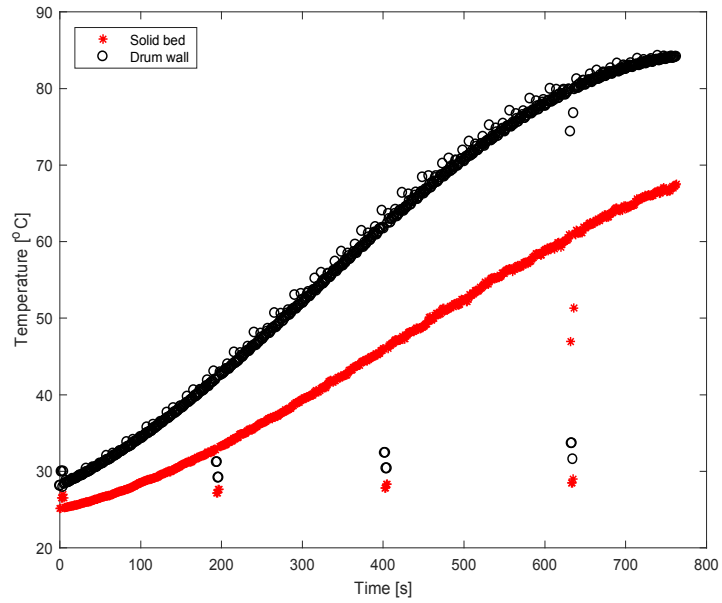
(b)

Figure A 33 (a) Heat transfer coefficient and (b) average temperatures at 10 %

fill level and 6 rpm for trial 2.
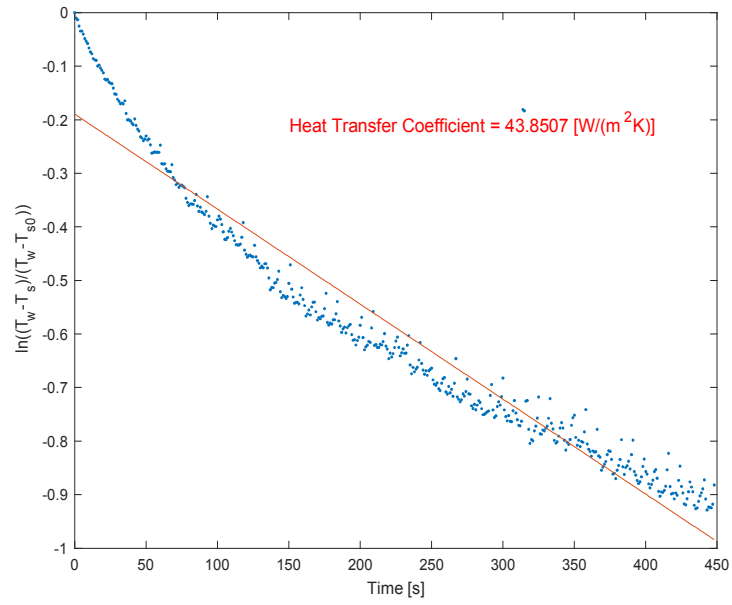
(a)
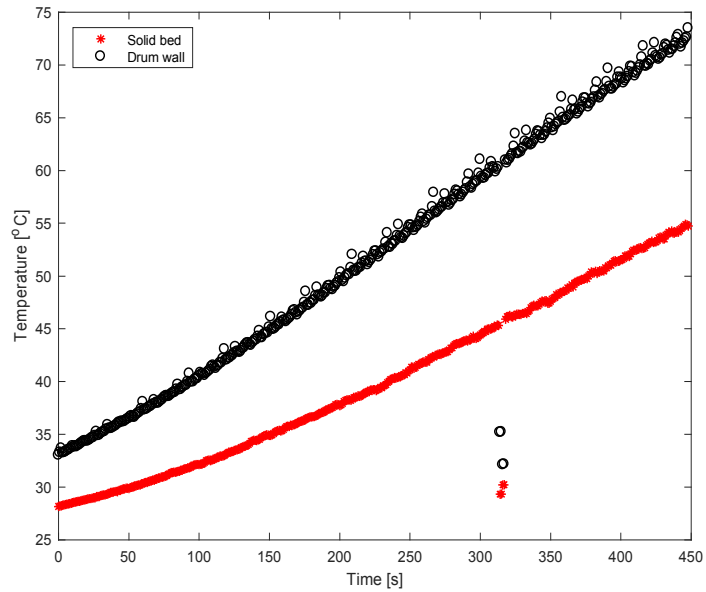
(b)

Figure A 34 (a) Heat transfer coefficient and (b) average temperatures at 10 %

fill level and 6 rpm for trial 3.
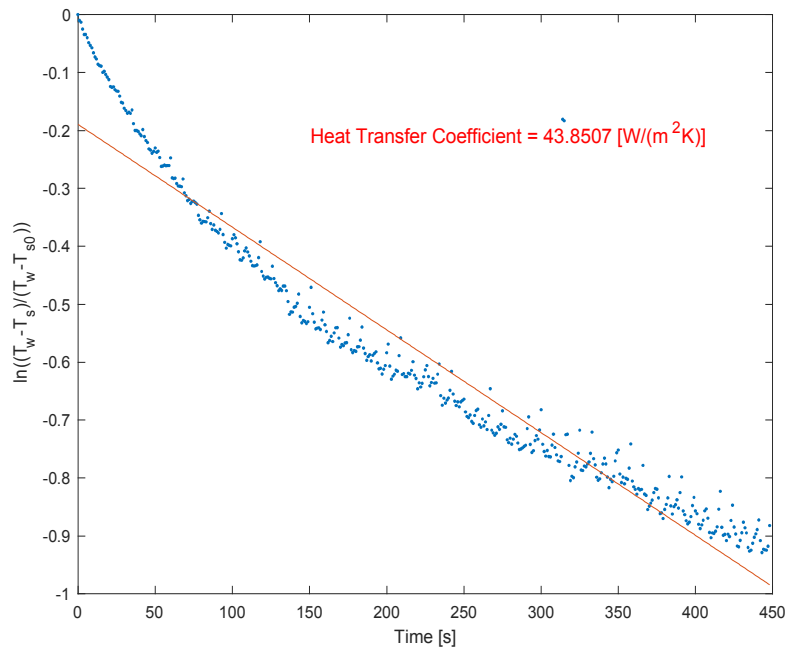
(a)
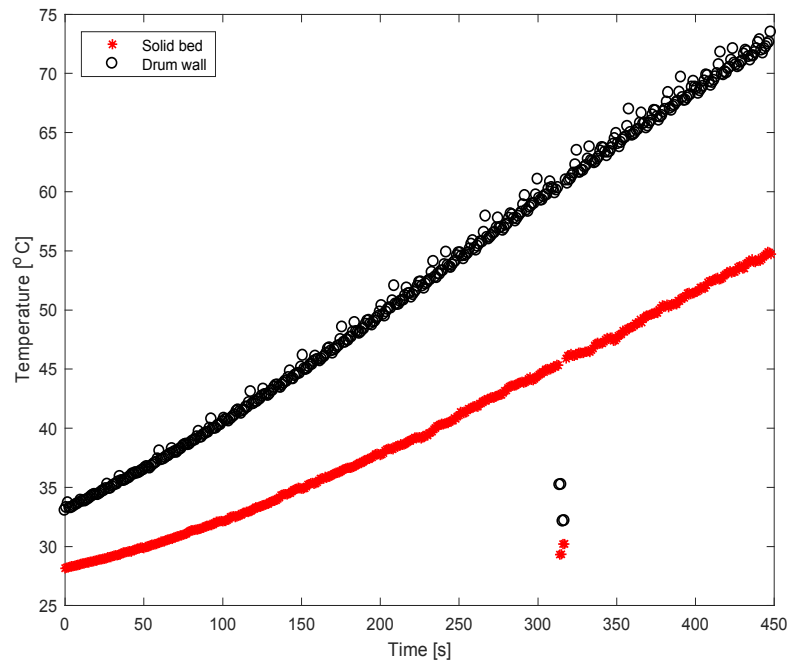
(b)

Figure A 35 (a) Heat transfer coefficient and (b) average temperatures at 10 %

fill level and 10 rpm for trial 1.

184
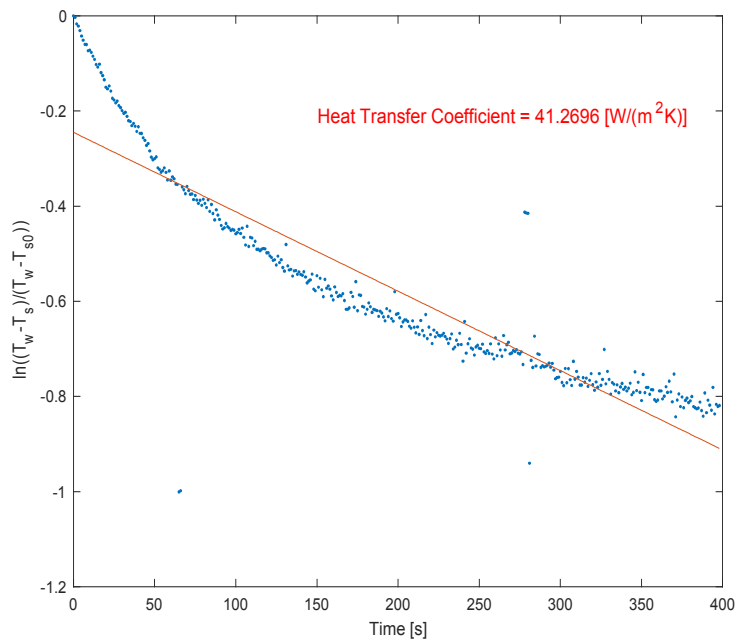
(a)
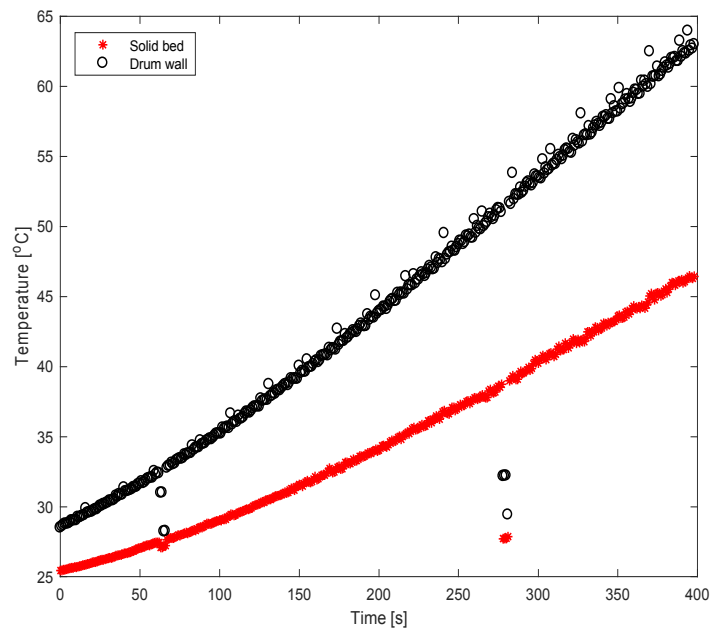
(b)

Figure A 36 (a) Heat transfer coefficient and (b) average temperatures at 10 %

fill level and 10 rpm for trial 2.
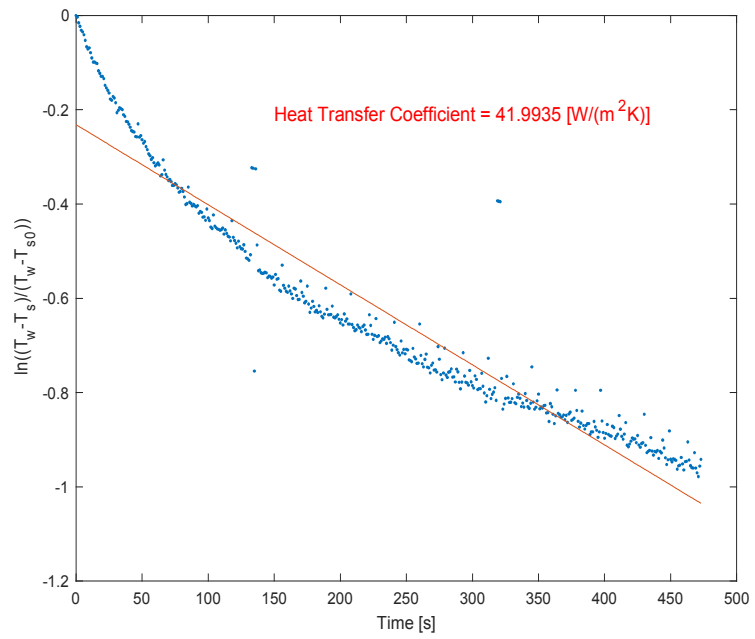
(a)
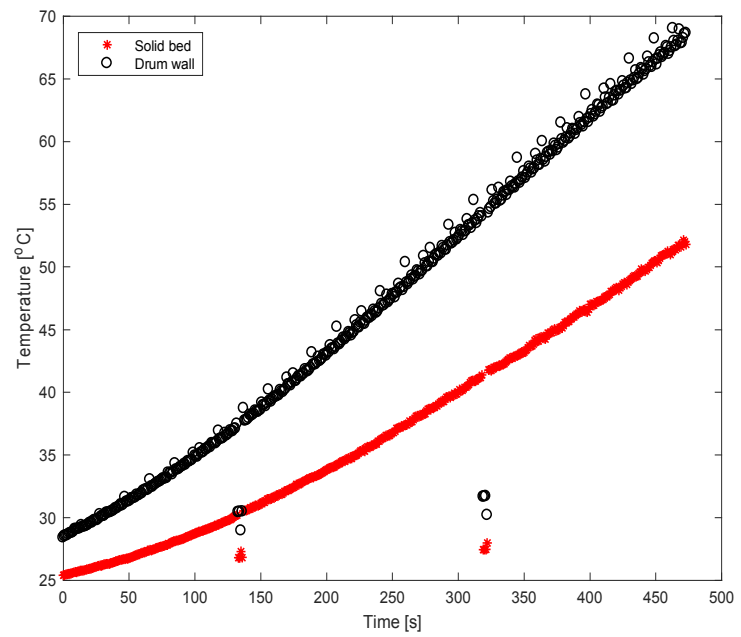
(b)

Figure A 37 (a) Heat transfer coefficient and (b) average temperatures at 10 %

fill level and 10 rpm for trial 3.
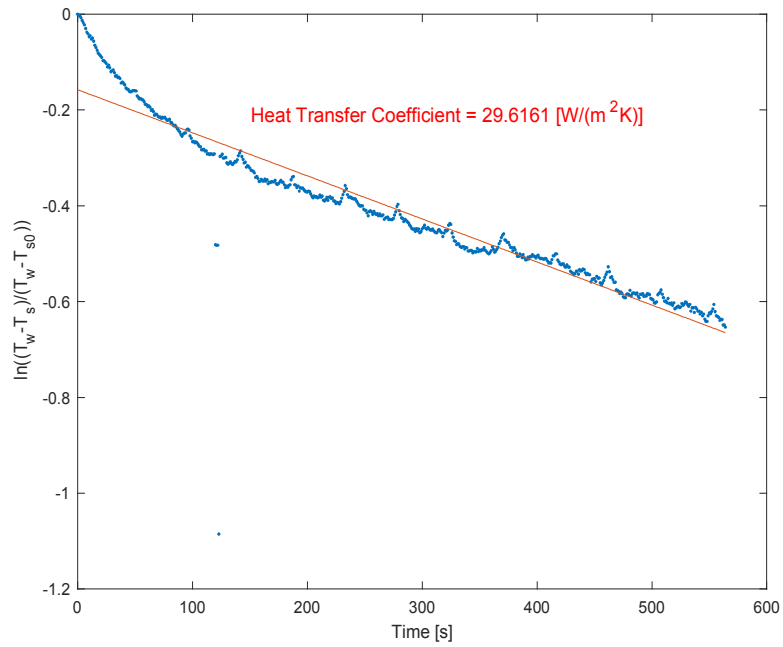
(a)
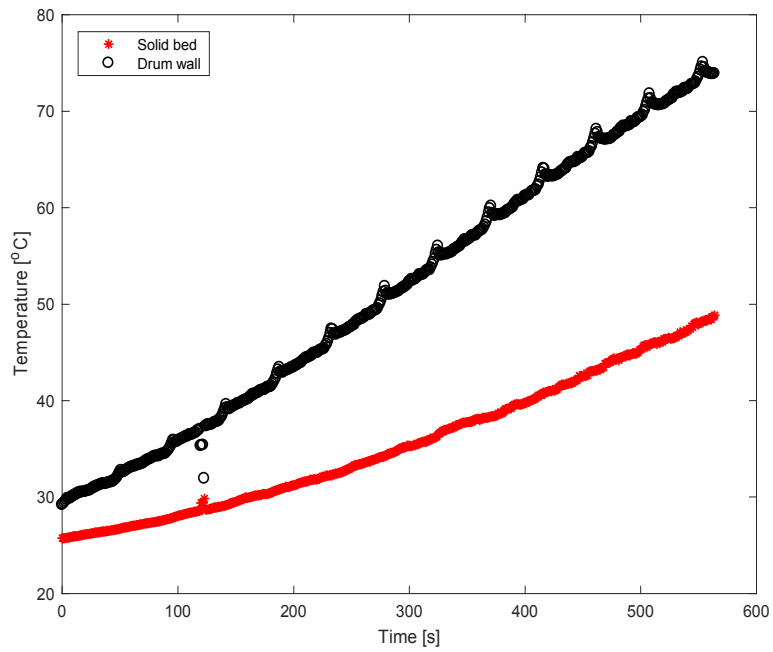
(b)

Figure A 38 (a) Heat transfer coefficient and (b) average temperatures at 17.5 %

fill level and 2 rpm for trial 1.
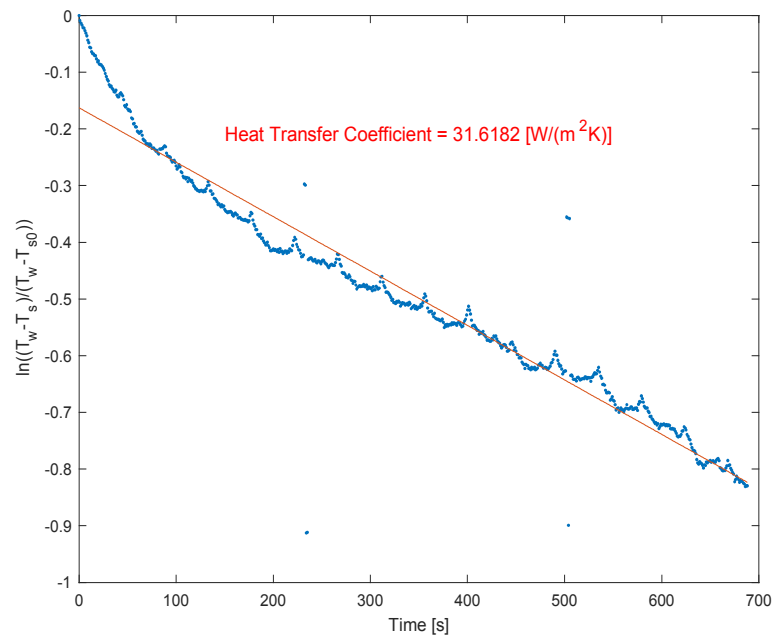
(a)
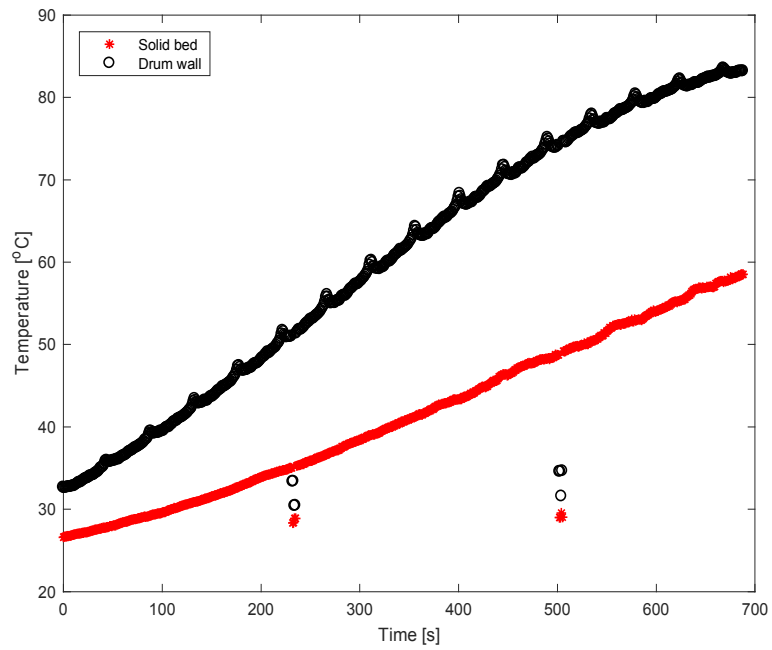
(b)

Figure A 39 ((a) Heat transfer coefficient and (b) average temperatures at 17.5 %

fill level and 2 rpm for trial 2.
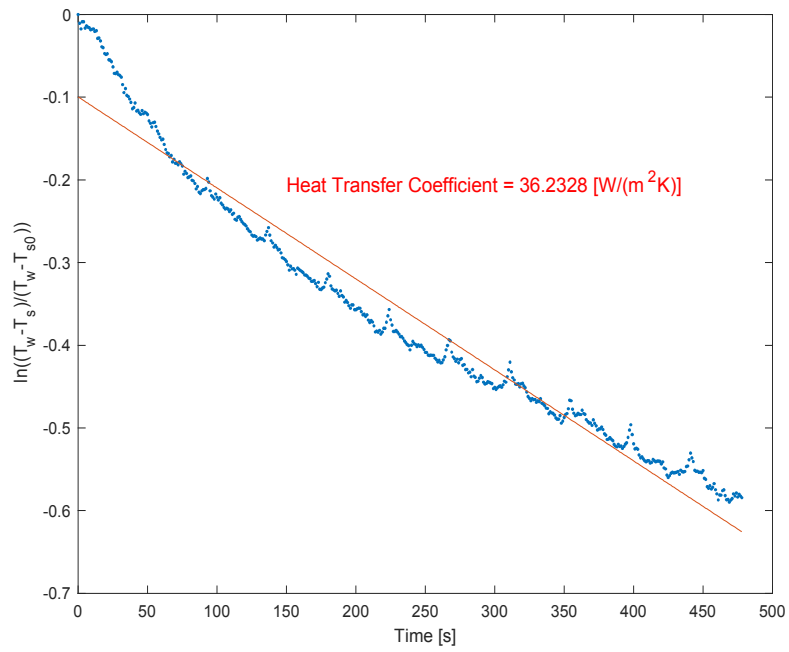
(a)
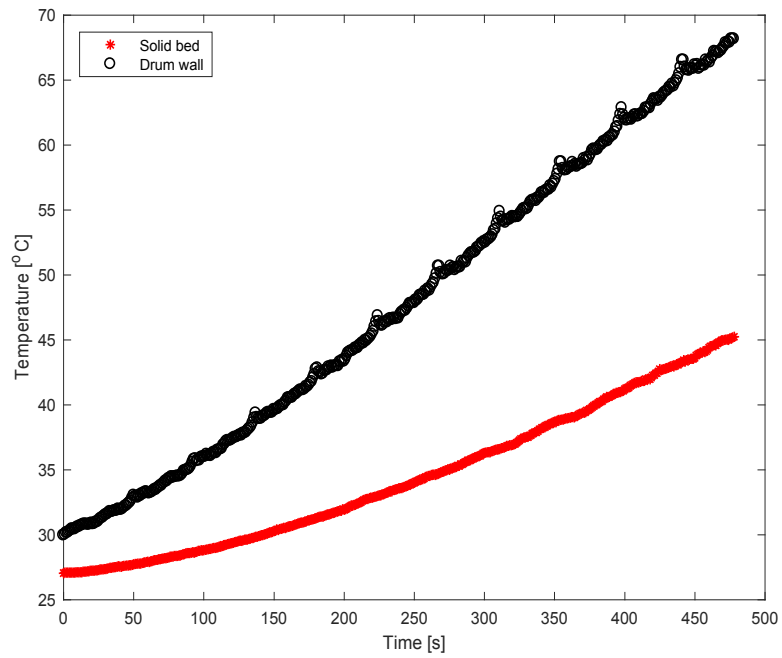
(b)

Figure A 40 (a) Heat transfer coefficient and (b) average temperatures at 17.5 %

fill level and 2 rpm for trial 3.
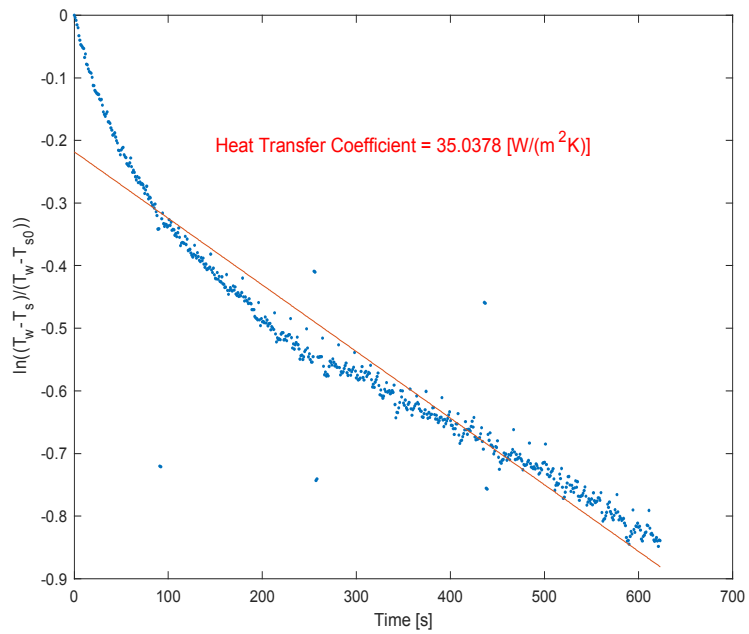
(a)
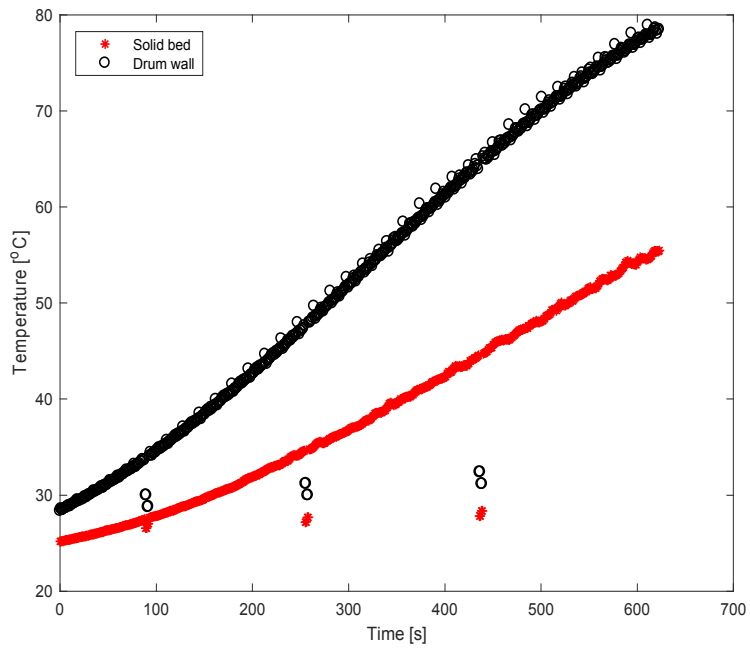
(b)

Figure A 41 (a) Heat transfer coefficient and (b) average temperatures at 17.5 %

fill level and 6 rpm for trial 1.
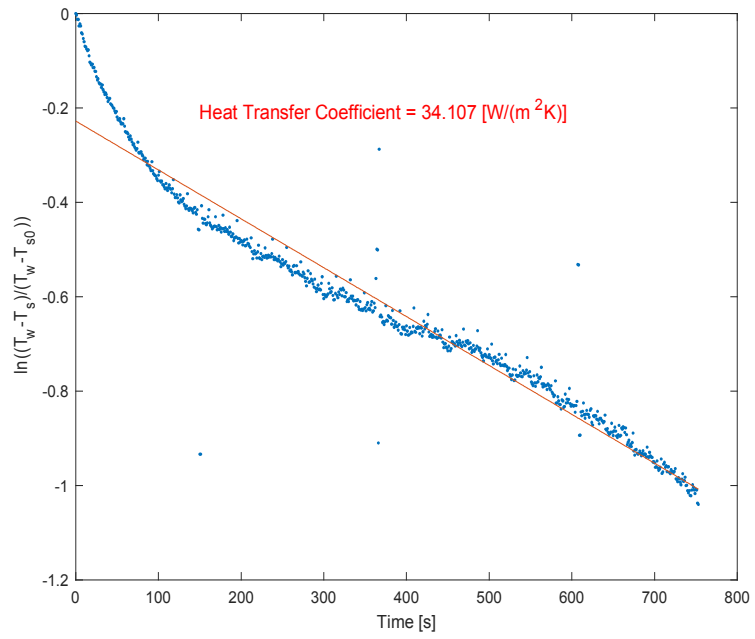
(a)
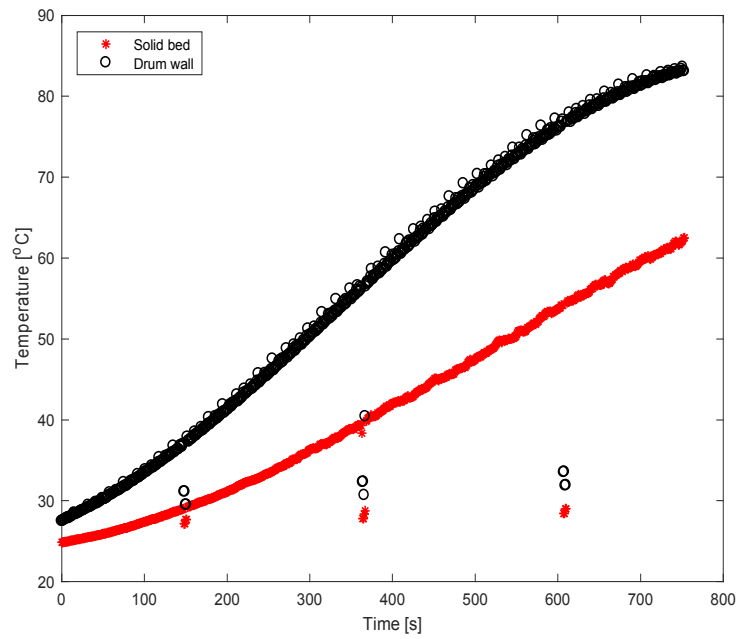
(b)

Figure A 42 (a) Heat transfer coefficient and (b) average temperatures at 17.5 %

fill level and 6 rpm for trial 2.
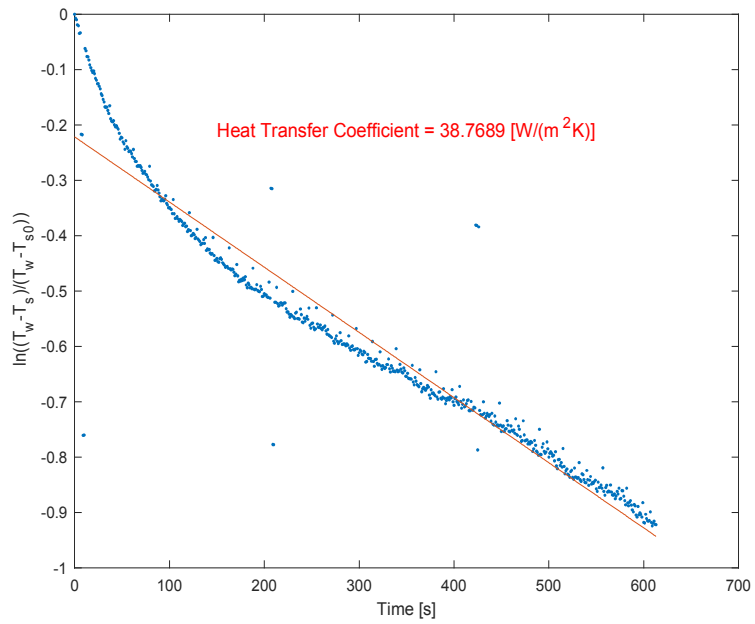
(a)
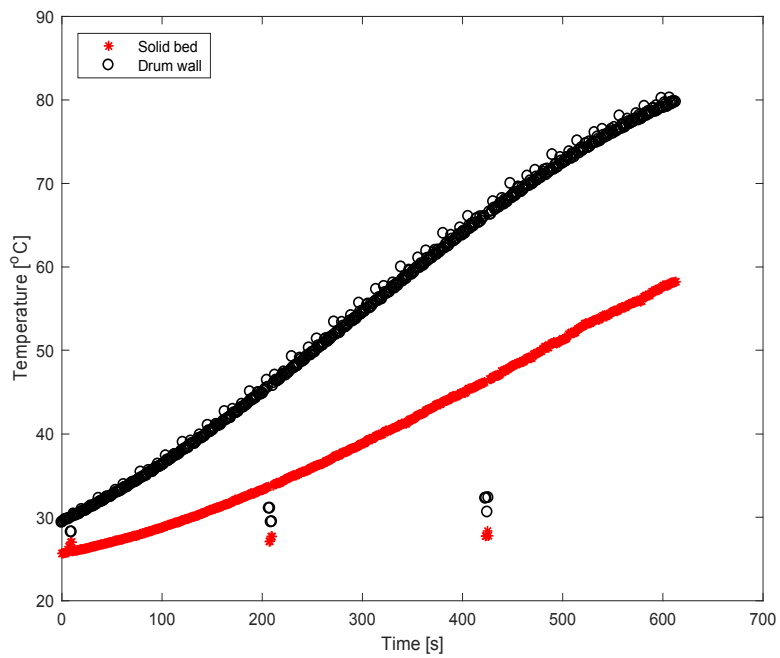
(b)

Figure A 43 (a) Heat transfer coefficient and (b) average temperatures at 17.5 %

fill level and 6 rpm for trial 3.
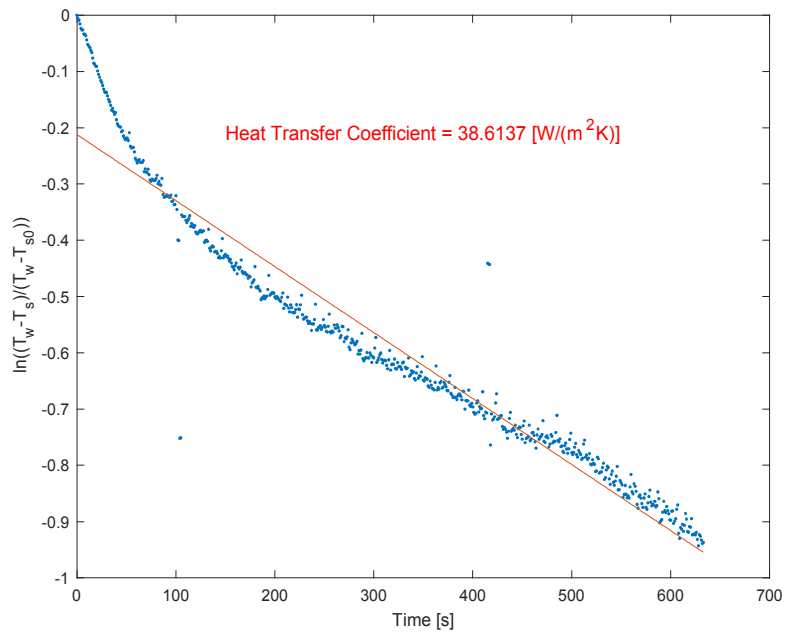
(a)
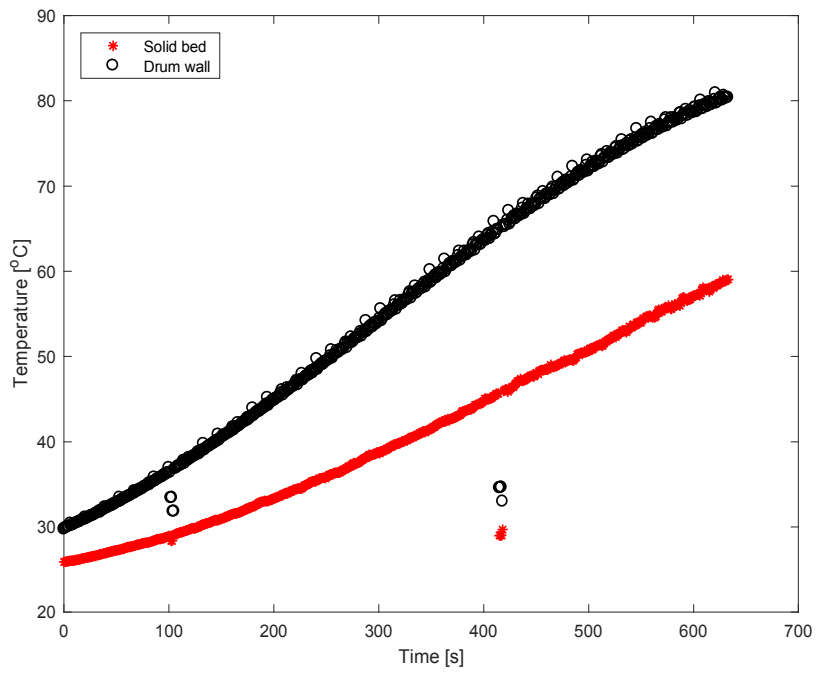
(b)

Figure A 44 (a) Heat transfer coefficient and (b) average temperatures at 17.5 %

fill level and 10 rpm for trial 1.

193
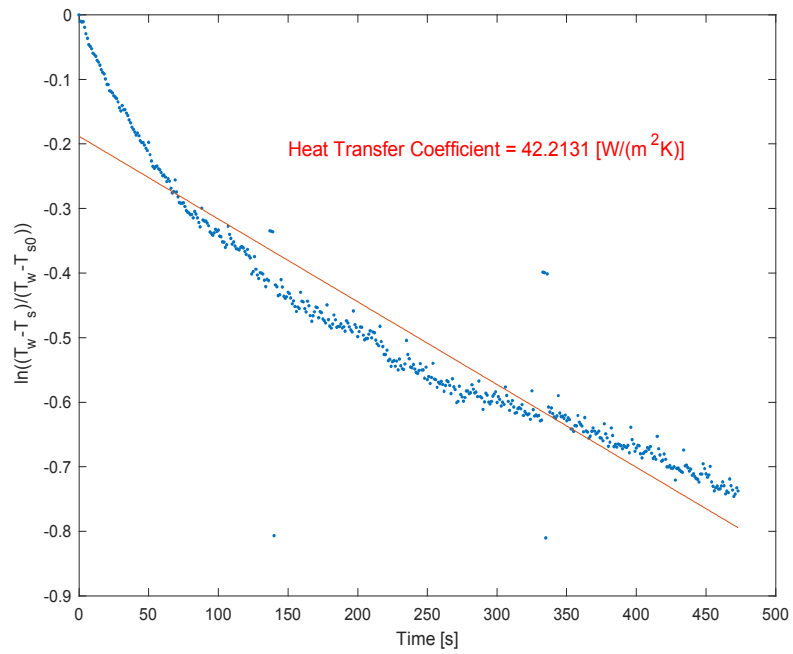
(a)
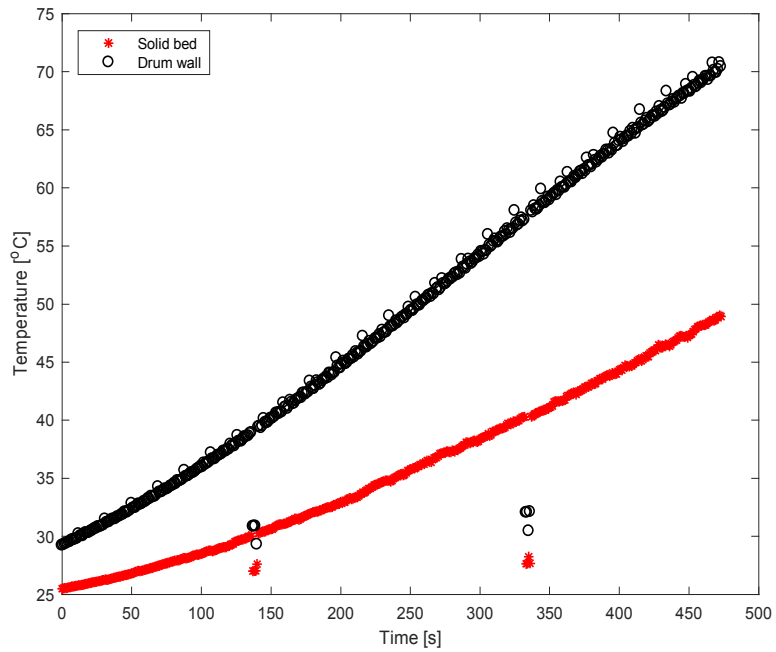
(b)

Figure A 45 (a) Heat transfer coefficient and (b) average temperatures at 17.5 %

fill level and 10 rpm for trial 2.

194
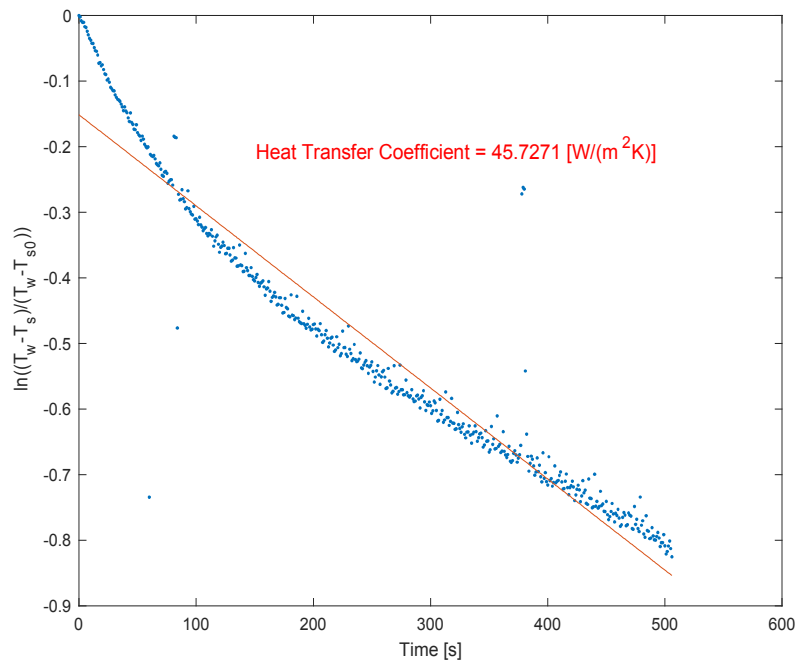
(a)
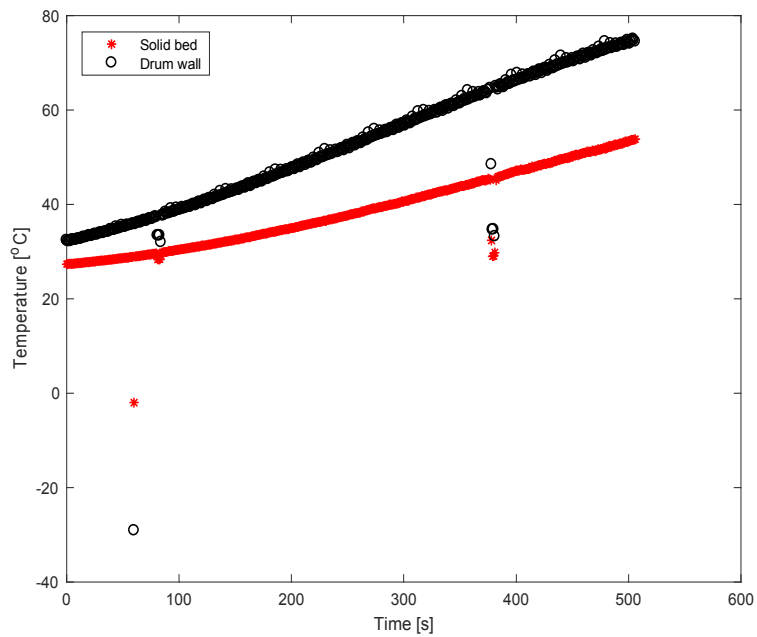
(b)

Figure A 46 (a) Heat transfer coefficient and (b) average temperatures at 17.5 %

fill level and 10 rpm for trial 3.
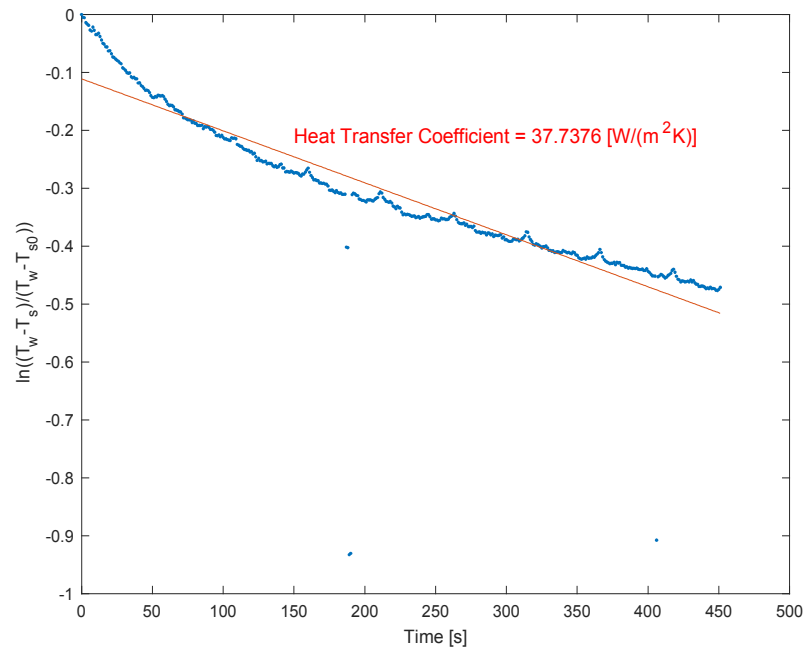
(a)
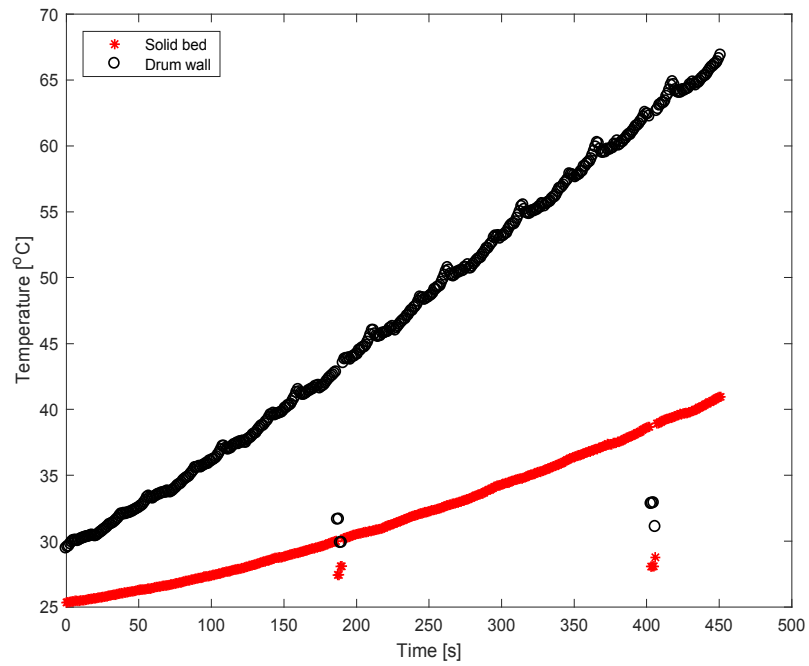
(b)

Figure A 47 (a) Heat transfer coefficient and (b) average temperatures at 25 %

fill level and 2 rpm for trial 1.
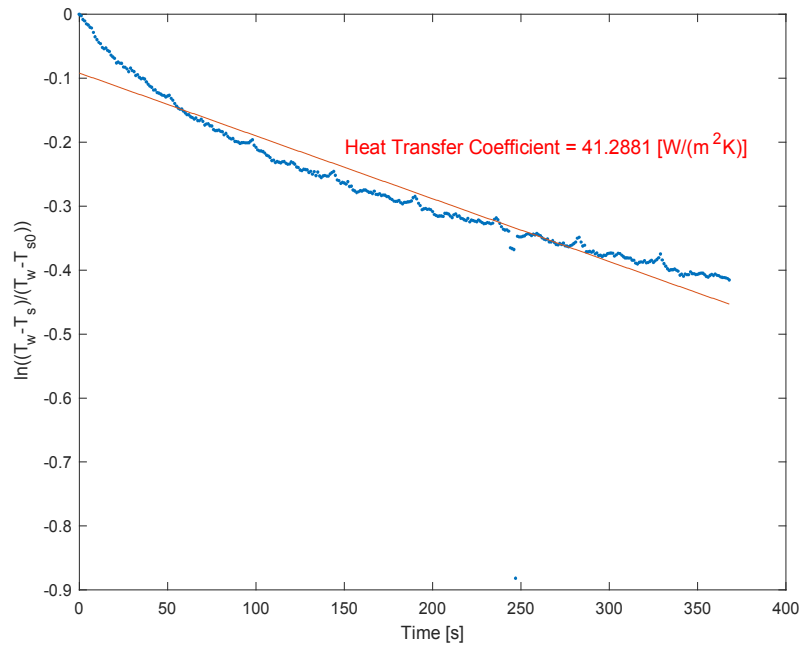
(a)
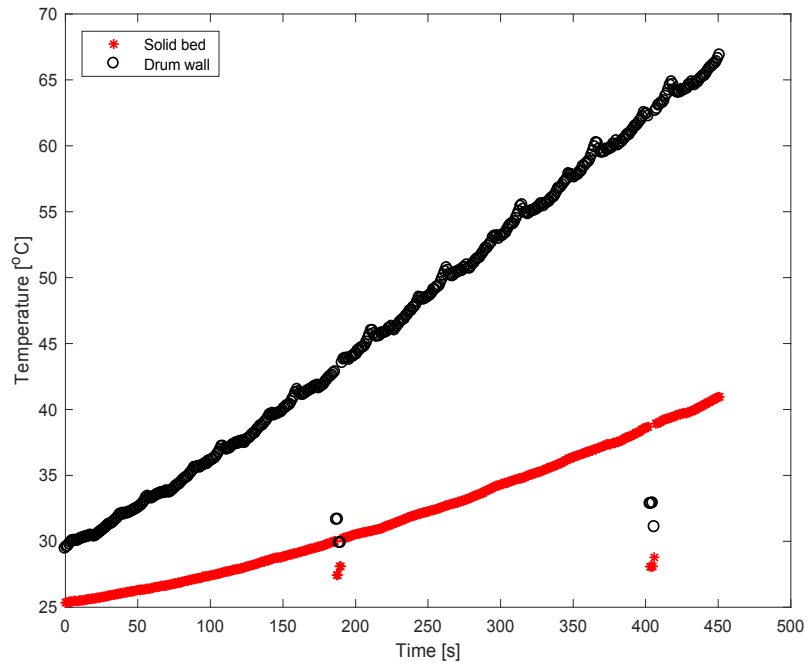
(b)

Figure A 48 (a) Heat transfer coefficient and (b) average temperatures at 25 %

fill level and 2 rpm for trial 2.
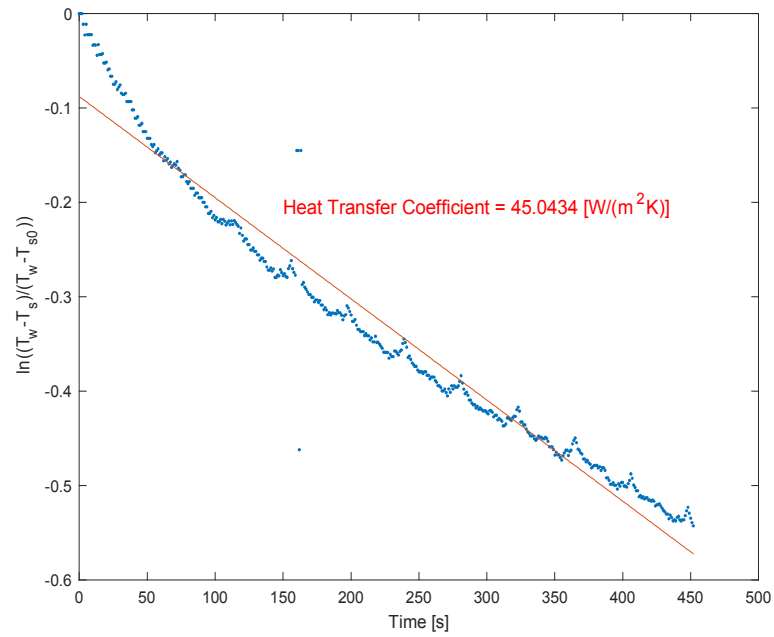
(a)
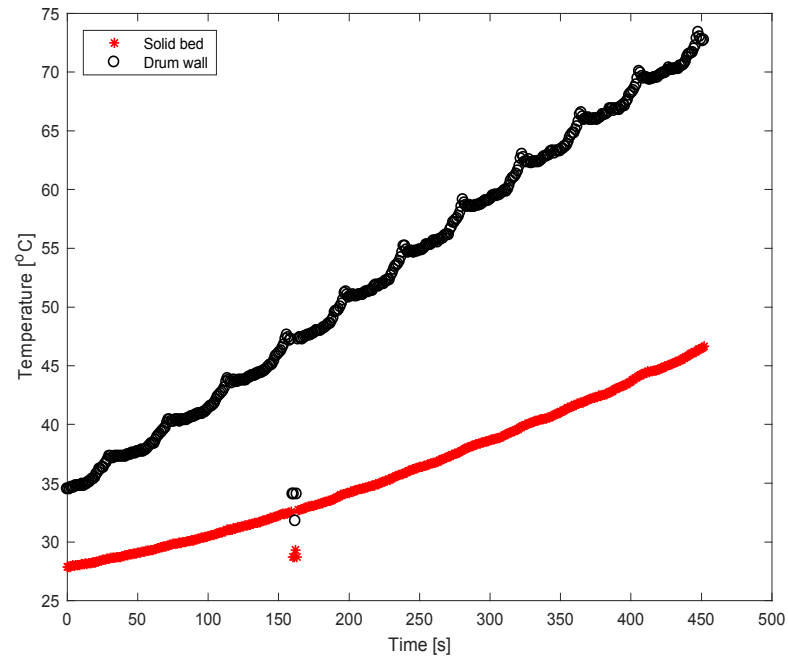
(b)

Figure A 49 (a) Heat transfer coefficient and (b) average temperatures at 25 %

fill level and 2 rpm for trial 3.
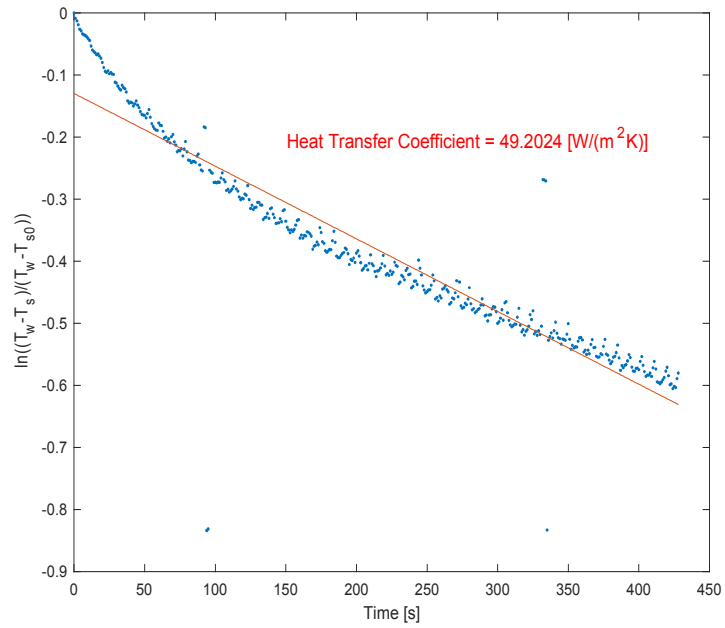
(a)
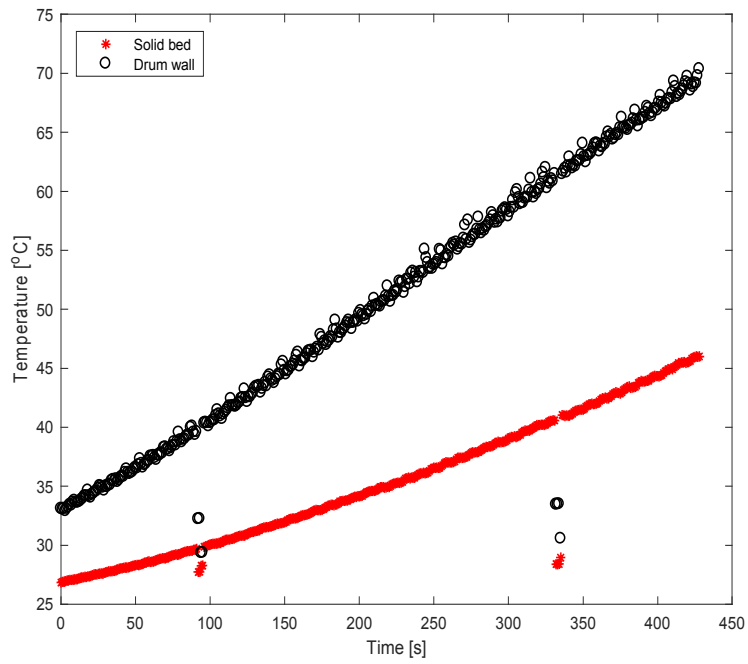
(b)

Figure A 50 (a) Heat transfer coefficient and (b) average temperatures at 25 %

fill level and 6 rpm for trial 1.
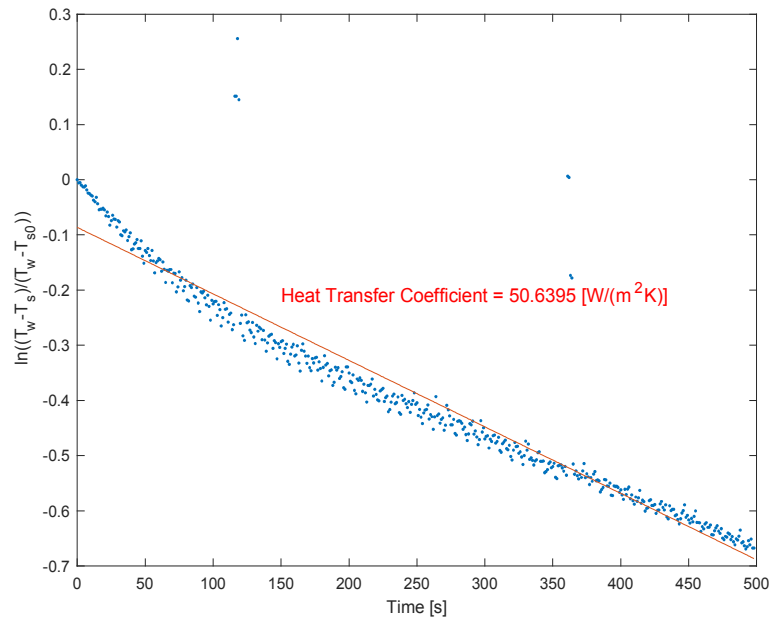
(a)
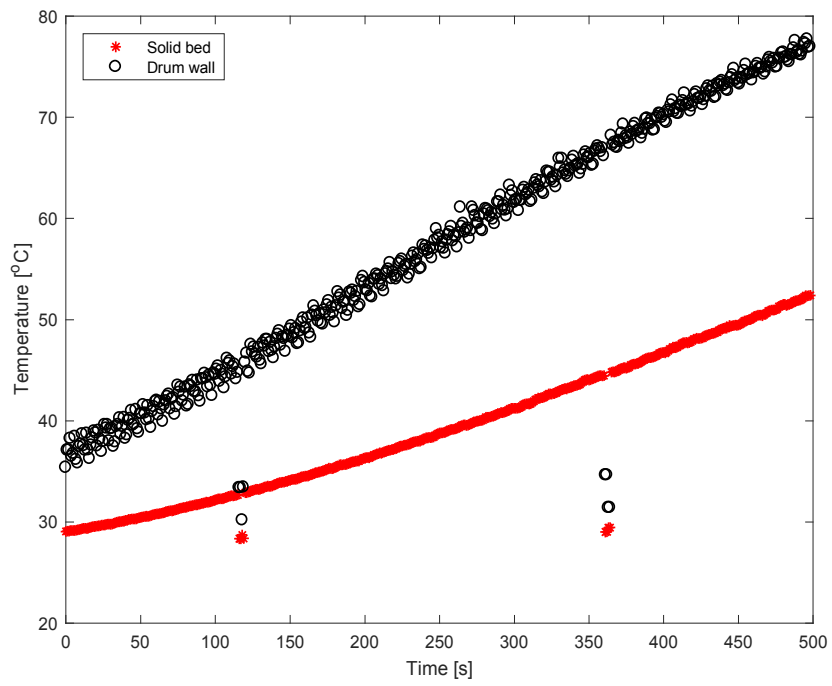
(b)

Figure A 51 (a) Heat transfer coefficient and (b) average temperatures at 25 %

fill level and 6 rpm for trial 2.

200
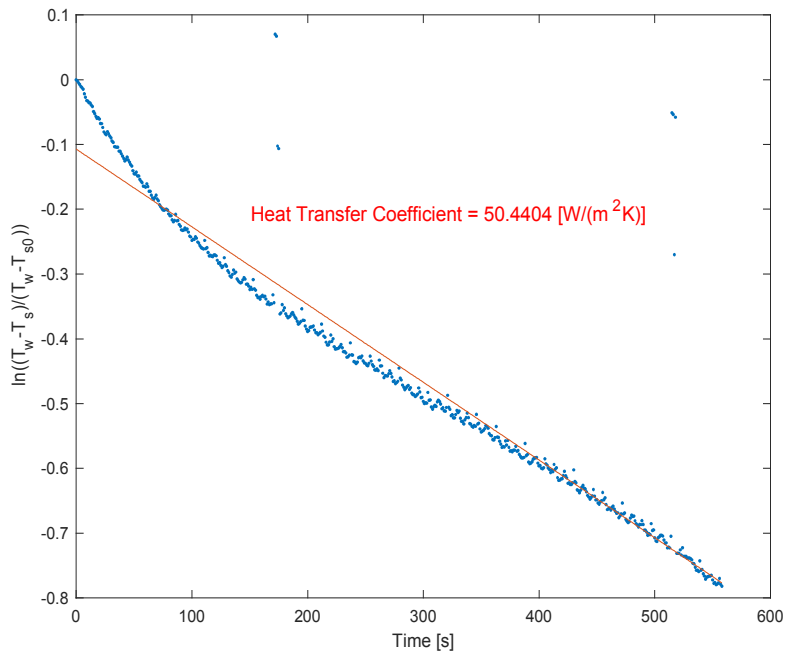
(a)
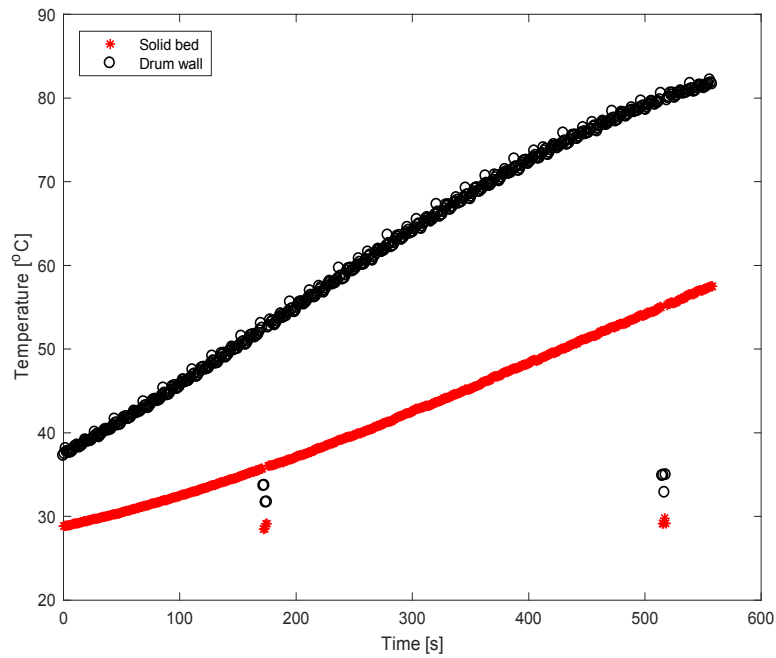
(b)

Figure A 52 (a) Heat transfer coefficient and (b) average temperatures at 25 %

fill level and 6 rpm for trial 3.
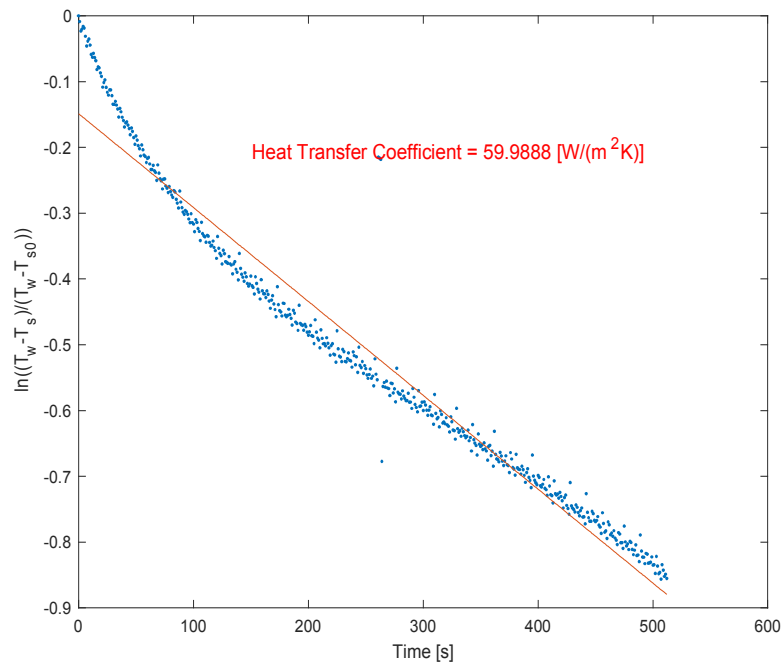
(a)
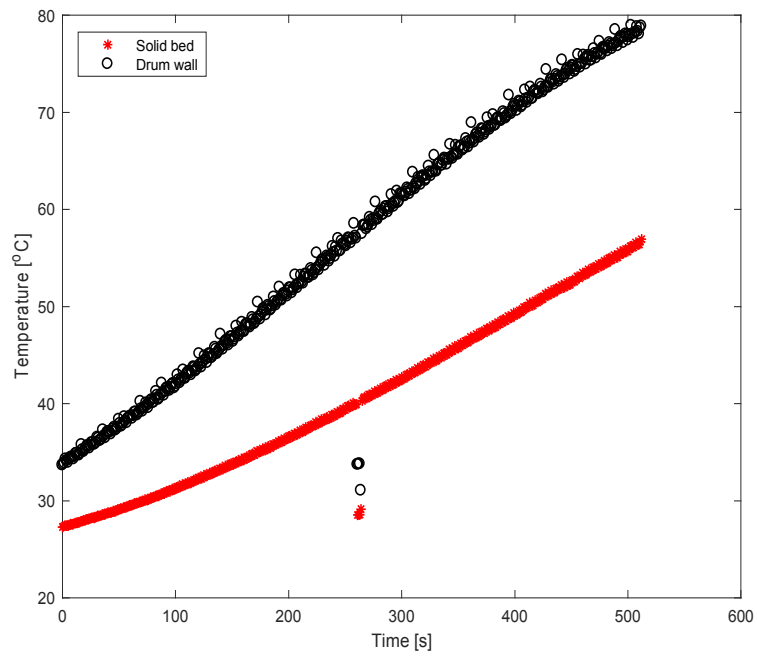
(b)

Figure A 53 (a) Heat transfer coefficient and (b) average temperatures at 25 %

fill level and 10 rpm for trial 1.
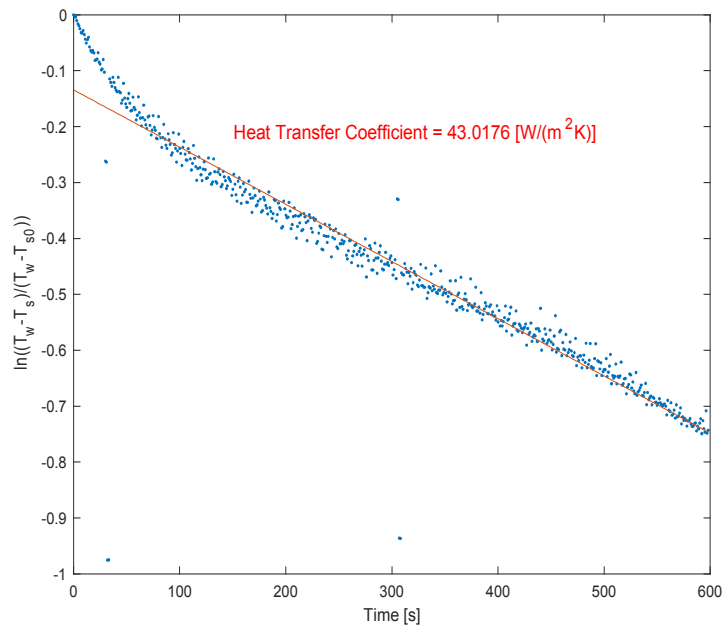
(a)
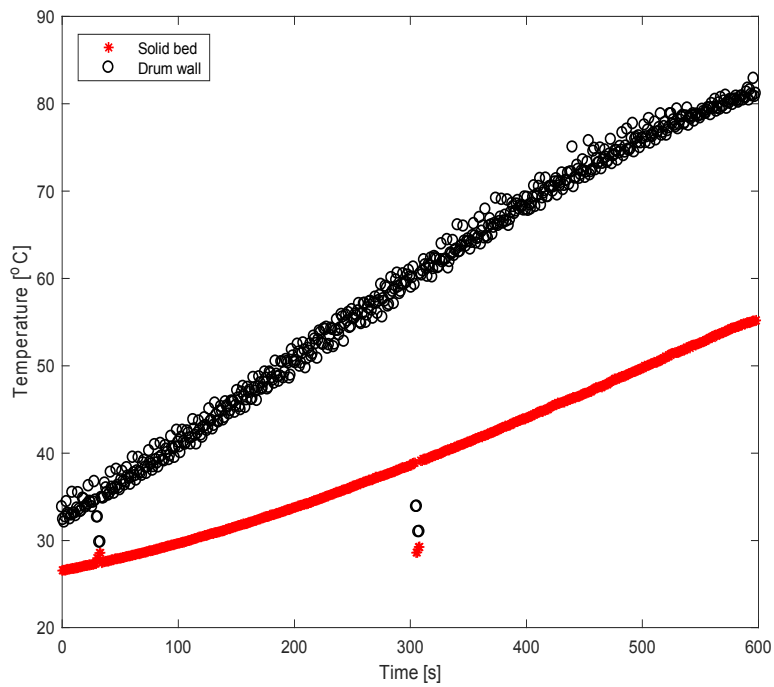
(b)

Figure A 54 ((a) Heat transfer coefficient and (b) average temperatures at 25 %

fill level and 10 rpm for trial 2.
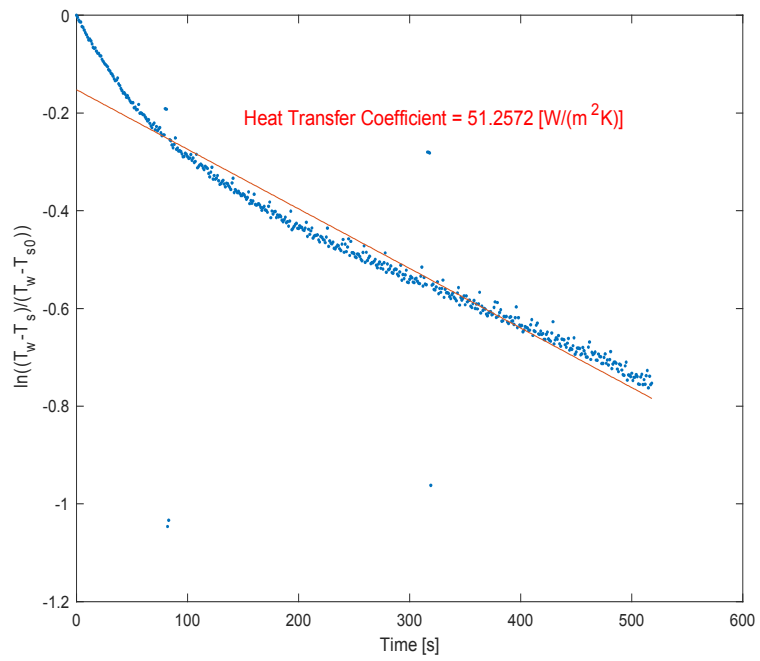
(a)
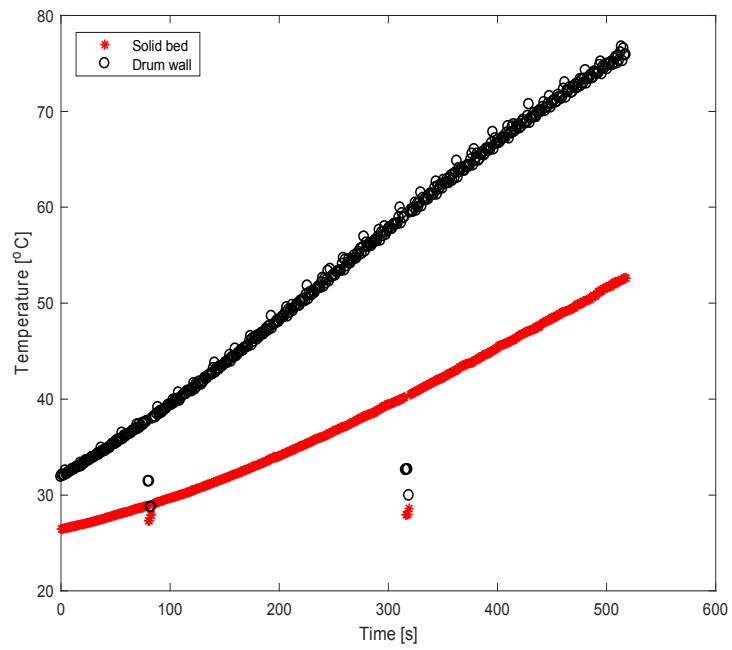
(b)

Figure A 55) Heat transfer coefficient and (b) average temperatures at 25 % fill

level and 10 rpm for trial 3.

APPENDIX F

LIST OF PUBLICATIONS

1. Chen, S., Adepu, M., Emady, H., Jiao, Y., & Gel, A. (2017). Enhancing the Physical Modeling Capability of Open-source Mfix-dem Software for Handling Particle Size Polydispersity: Implementation and Validation. Powder Technology, 317, 117-125.

2. Adepu, M., Emady, H. Wall to Particle Bed Contact Conduction Heat Transfer in a Rotary Drum Using Dem. Submitted for Publication.

3. Adepu, M., Boepple, B., Fox, B., Emady, H. Conduction Heat Transfer in a Rotary Drum Using Infrared Thermography. Submitted for Publication.

4. Adepu, M., Emady, H. Convection Heat Transfer in a Rotary Drum Using Dem Using Infrared Thermography. Under Preparation for Publication.

5. Adepu, M., Emady, H. Effect of Particle and Wall Roughness on Discharge of Silica Beads Through Hoppers. Under Preparation for Publication.

BIOGRAPHICAL SKETCH

Manogna Adepu is a doctoral candidate of chemical engineering at Arizona State University (ASU) in Tempe, working in the Process and Product Design Lab with Dr. Heather Emady. She received a B.Tech in chemical engineering from Jawaharlal Nehru Technological University, India (2013) and an M.S in chemical engineering from Rutgers University, New Brunswick (2015). She has expertise in computational and experimental research mainly focusing on granular heat transfer in rotary drums, segregation of particles through hoppers, hydrodynamics in a fluidized bed, multiphase modeling and simulations (using CFD, DEM, and PBM), spouted Wurster coating, and high-shear wet granulation.